Micro Optics for Micro Hybrid Concentrator Photovoltaics

by

Duanhui Li

B.S. Materials Science and Engineering
Tsinghua University (2012)

Submitted to the Department of Materials Science and Engineering
in partial fulfillment of the requirements for the degree of

Doctor of Philosophy in Materials Science and Engineering

at the

MASSACHUSETTS INSTITUTE OF TECHNOLOGY

September 2019

Author . . . .
Department of Materials Science and Engineering
August 5, 2019

Certified by . . . .
Juejun Hu
Merton C. Flemings Career Development
Associate Professor of Materials Science and Engineering
Thesis Supervisor

Accepted by . . . .
Donald R. Sadoway
John F. Elliott Professor of Materials Chemistry
Chairman, Department Committee on Graduate Studies

Micro Optics for Micro Hybrid Concentrator Photovoltaics

by

Duanhui Li

Submitted to the Department of Materials Science and Engineering
on August 5, 2019, in partial fulfillment of the
requirements for the degree of
Doctor of Philosophy in Materials Science and Engineering

Abstract

Concentrating photovoltaics (CPV) systems use concentrating optical elements to significantly reduce the material and processing costs of multi-junction high efficiency solar cells and improve the conversion efficiency. However, several issues hindered the development of CPV technologies due to the fundamental limit of thermodynamics and practical difficulties of manufacturing and deployment, such as system bulkiness, tight tracking error, thermal management and inability to collect diffuse irradiance. By dramatically scaling down the dimensions of the cells to the level of hundreds of microns and accordingly the concentrating optics, micro hybrid CPV overcomes the listed issues and also delivers a small form factor module profile similar to conventional flat panel PV. In this thesis, we are focusing on the critical optical components in the micro hybrid CPV: the micro optics.

First, we demonstrated a wafel-level micro hybrid CPV module based on Si fabrication. By introducing the micro cavities in Si wafer with wet etching, this novel micro optical element illustrates its potential for cost-effective collection of both direct and diffuse sunlight, thereby extending the geographic and market domains for cost-effective PV system deployment. By improving the CPV figure of merit by 46%, our micro hybrid CPV module demonstrated state-of-the-art small-form-factor CPV module optical performance.

Next, we focused on developing a micro-prism-array based low-profile spectrum splitting optics assembly. By novelly combining conjugate optics design with materials optical properties, the high-efficiency, low-cost, and low-profile optics potentially enables significant improvement on solar module performance and reduction of energy production costs.

Lastly, we developed a simulation frame work to generate annualized diffuse radiance energy distribution map that covers the whole United States region. This simulation approach accounts for different geographic locations and weather conditions and aims to provide high accuracy reference for diffuse concentrator design.

Thesis Supervisor: Juejun Hu
Title: Merton C. Flemings Career Development

Associate Professor of Materials Science and Engineering

Acknowledgments

First I would like to express my sincerest gratitude to my advisor Prof. Juejun Hu. I won't be able to pursue my PhD degree without you giving me this opportunity. You are the most helpful and supportive person I have ever seen. Your passion and comprehensive understanding in optics have inspired me through the whole project and you will always be a role model in my following careers. Next I would like to thank my thesis committee members Dr. Jurgen Michel and Prof. Eugene A. Fitzgerald for your valuable feedbacks and guidance. The discussions with you have greatly motivated me to expand my knowledge and skills.

I also would like to thank all my collaborators for the achievements we made together. I would like to thank Dr. Tian Gu for introducing me into the field of CPV and guiding me when I was a novice. I would like to thank Prof. Lan Li for the close collaboration and support in WPV project. I would like to thank Qianyi Zhang for the contribution in diffuse irradiance simulation. I would like to thank Dr. Ujjwal Das from IEC and the Sandia National Lab team for the WPV module prototyping. I would like to thank all my collaborators in LAMB project for the great teamwork and discussion, especially Dr. Ruitao Wen and Haoquan Zhang for educating and supporting each other.

I would like to thank the whole PMAT and EMAT group. Even though we did not work closely due to the disparity in research topics, but I still benefitted a lot from the smart, passionate and helpful group of people. I especially want to thank Dr. Qingyang Du. I am glad we became close friends by interesting coincidence. Without all the good things you told me about JJ, I won't be brave enough to step into the field of optics and grasp this opportunity.

I would like to thank all the people I worked with in MIT Chinese Students and Scholars Association. CSSA is the organization I felt most belonging to in MIT. All of you are great team workers and friends. I especially would like to thank Zhaohong Han and Binghong Han for introducing me into it, and Tailin Wu for the pleasant collaboration as co-presidents.

I would like to thank all the friends I met in MIT. I am grateful to have you through my journey here.

I would like to thank my best friend Jun Gao. We have supported each other during our darkest times and learned from each other's merits. You are the most diligent and determined person I have met and I wish you achieve your deserved success and inner peace.

I would like to express my gratitude to my dear family. Thank you my parents for supporting us with all you can. I would never imagine me doing a better job if I were in your place. Thank you my older brother Duanjie Li for being a role model and guiding me through my whole student period.

Lastly, I want to express my deepest love to my dear wife Xi. I take my greatest achievement in MIT as having you as my life companion. Thank you for shining into my darkest time with warmth and hope. And thank you for bring in our cute little Adam. I know for better for worse, for richer for poorer, in sickness and in health, we will always hold our firm hands together.

Contents

List of Figures

List of Tables

Chapter 1

Introduction to Micro Hybrid Concentrator Photovoltaics

The world energy consumption has been steadily increasing in the past few decades. The finite and non-renewable fossil fuel resources are limiting its further growth since it occupies 90% of the total world energy consumption. [1] Despite the abundance issue, the utilization of the fossil fuels also generates severe environmental issues like the global warming and pollution. Thus the pursuit of green renewable energy has been one of the most critical topics for human civilization development.

All the energy resources on Earth, despite the nuclear energy, originate from the solar energy. Solar energy is an extremely abundant energy resource. The solar energy flux reaching the earth surface totals as 1.7×10^5 TW, [2] while the world annual energy consumption is predicted to reach 739 quadrillion BTU by 2040, which equals the solar energy illuminated on earth in only 1.27 hours. This is suggesting that an effective method to harvest the solar energy can sustain the human species for centuries. The great economic potential of solar energy has been driving the market escalation. The solar market has already provided 38% world expanded capacity, compared to the 30% from fossil fuels and nuclear energy in 2017. [3] Photovoltaics (PV) is the most promising technology to harvest the solar power. In this chapter, we will go over the fundamentals of the PV technology, especially concentrator photovoltaics (CPV), and discuss the current system development status.

1.1 Concentrator Photovoltaics Fundamentals

1.1.1 Introduction of Solar Irradiance

Solar irradiance originates from the Sun nuclear furnace. The Sun's electromagnetic spectrum spans from a wide range of wavelength, from ultraviolet (UV) to visible, infrared (IR) and radio waves. After travelling a long distance to the surface of the Earth, the average intensity of the solar radiation is 1366 W/m^2. For terrestrial solar energy application, the solar radiation will go through the atmosphere, and get reduced to the level of $1000 W/m^2$ due to the atmosphere reflection, scattering and absorption. [4]

Due to the scattering of the atmosphere, the solar radiation is typically divided into two parts: The direct light and the diffuse light. The direct light is defined as the radiation from a small solid angle of the sky, connecting the observer to the sun position. The World Meteorological Organization recommends 2.5° semi-angle for direct light definition consensus. [5] The diffuse light is defined as the solar radiation scattered out from the direct beam by atmosphere into the hemisphere of the sky dome. The distribution of the diffuse radiation depends on various factors including the sun position, weather conditions and the tracking method.

Solar irradiation is described by the following terms: global horizontal irradiance (GHI), global tilted irradiance (GTI) and direct normal irradiance (DNI), as depicted in Figure 1-1, respectively. [6] DNI is defined as the direct light irradiance measured on a plane that is perpendicular to the line connecting the observer to the sun position, within the 2.5° semi-angle. It can be measured by pyrheliometer, a sun sensor that has 2.5° semi-angle acceptance cone. GHI and GTI are both global solar irradiance, including both the direct light and the diffuse light components. They can be measured by pyranometer, which has a hemisphere acceptance cone. Their difference is in the tracking method: GHI is measured on a horizontal plane while GTI is measured with the sensor plane tracking the sun. They can be expressed as:

$$GHI = DNI \cos\theta + DHI \tag{1.1}$$

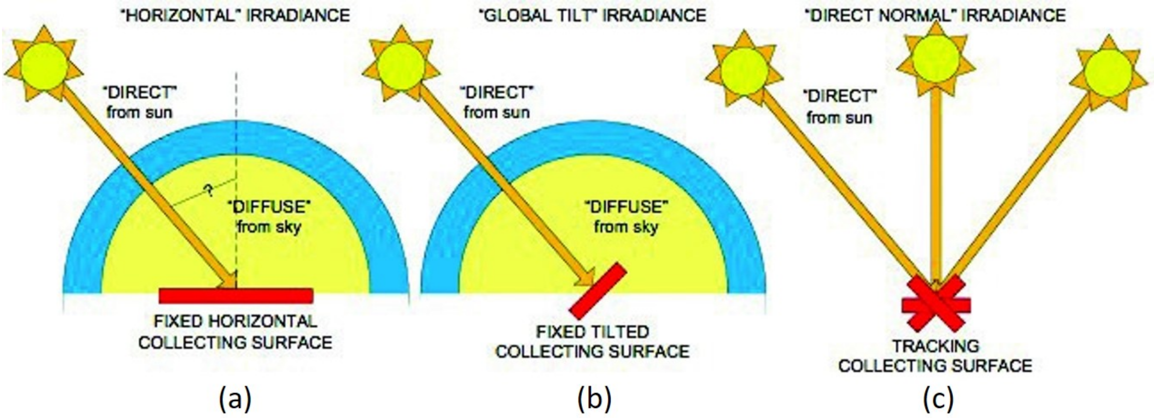

Figure 1-1: Solar irradiance definition Schematics: (a) GHI, (b) GTI and (c) DNI. (The red plane represents the sensor and its facing direction)

$$GTI = DNI + DTI + R_g \tag{1.2}$$

in which θ is the angle between the sun position and the normal of the horizontal plane, DHI is diffuse horizontal irradiance describing the diffuse light irradiance on horizontal plane, DTI is diffuse tilted irradiance describing the diffuse light irradiance on the tilted plane, and R_g is the ground reflected irradiance.

Solar irradiance is directly affected by the sun position and the weather conditions. The sun position is a function of geographic locations and solar time, as depicted in Figure 1-2. [4] The sun position determines the air mass (AM), which is defined as the path length of the solar irradiance that goes through the atmosphere. The lowest AM value is 1, which happens when the solar elevation angle is 90° and the solar irradiance only goes through 1 unit of atmosphere thickness. The larger air mass means longer path to scatter the solar beam, and thus more diffuse light. The weather affects the solar irradiance through the atmosphere particles (aerosol, cloud water molecules, rain droplets and et al.) by reflection and scattering. These complicated factors lead to the extremely variable nature of solar irradiance.

To provide a standard reference for the solar energy community, the standard spectrum ASTM G-173-03 (ISO 9845-1) AM1.5 is proposed for terrestrial solar applications. The spectrum condition is simulated with the sensor facing the sun position,

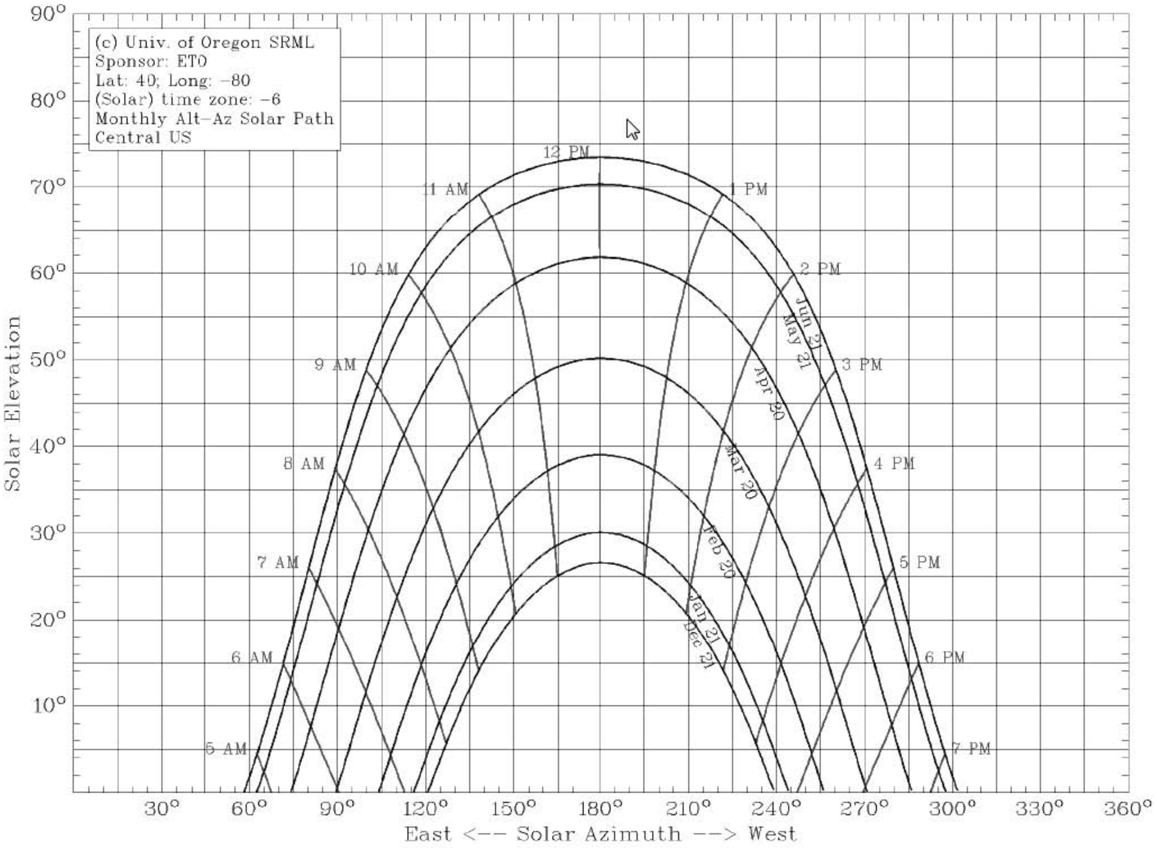

Figure 1-2: Sun path for 40 N 80 W in the central United States in altitude-azimuth format.

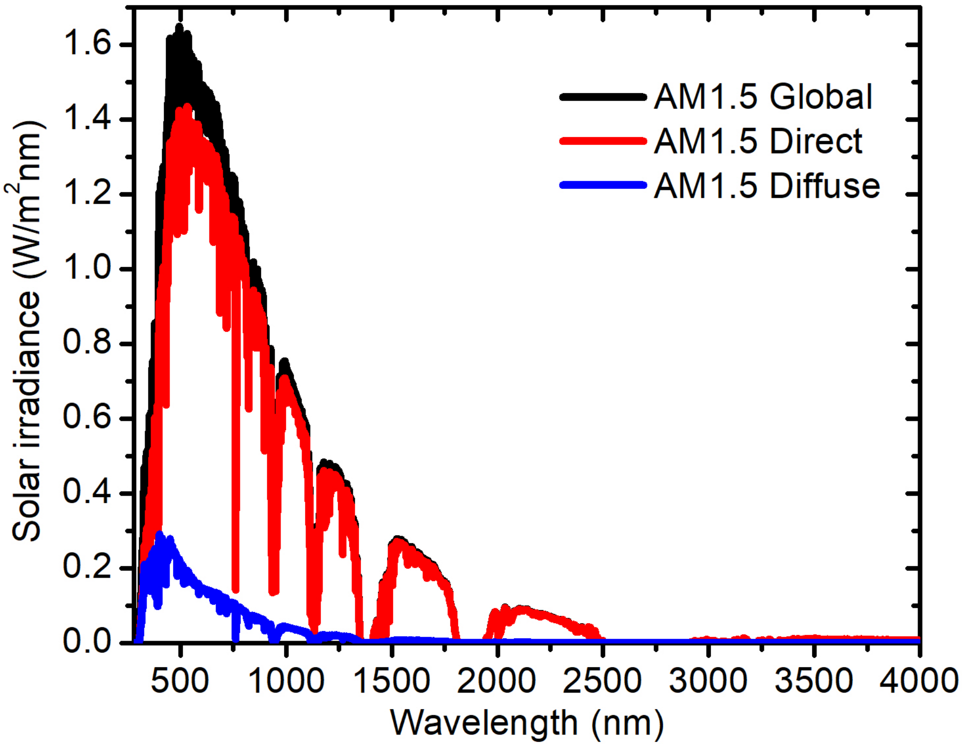

Figure 1-3: Standard AM 1.5 spectrum for terrestrial application.

at an elevation angle as 41.81° (air mass value is 1.5) in an clear weather. [7] The spectrum wavelength range covers from 280 nm to 4000 nm, as plotted in Figure 1-3. GTI, DNI and DTI are 1000 W/m^2, 900 W/m^2 and 100 W/m^2, respectively. Currently, most of the PV device optimizations and the system designs are based on the standard AM1.5 spectrum. It provides a good reference for the fair comparisons between the different PV modules and systems. However, it also leaves room for the discrepancy between research study and field performance.

1.1.2 Photovoltaic Cells

PV cells harvest the solar energy by converting the photons to electron and hole pairs. Photon energy is inversely proportional to its wavelength λ as:

$$E = \frac{hc}{\lambda} \tag{1.3}$$

in which h is the Planck's constant and c is the speed of light. When photon energy is smaller than the bandgap of the cell materials, it will pass without being absorbed. When the photon energy is larger than the bandgap, it will be absorbed. However, the cell can not harvest the full photon energy since the electron and hole pairs will quickly relax to the band-edge due to the thermalization process, and lose energy into heat.

After the electron hole pairs are generated, the electrons and the holes must be separated by electric field to drive the power consumer in the outer circuit. It is accomplished by the p-n junction structure, which is manufactured by doping donors and acceptors into the host material. This p-n junction generates a depletion region where the built-in electric field will sweep the photo-generated electrons and holes in opposite directions, and thus separate them. The single diode model to describe the PV cell performance is shown below:

$$I = I_o(e^{qV/nkT} - 1) - I_{ph} \tag{1.4}$$

in which I is the cell current, I_o is the dark saturation current related to the material quality, q is the unit electron charge, V is the cell voltage, n is ideal factor describing the carrier recombination process, k is the Boltzmann's constant, T is cell temperature and I_{ph} is the photo current.

The most important performance parameter of a PV cell is its energy conversion efficiency η, which is characterized by I-V sweeping measurement with a known input solar irradiance P_i. Then η is calculated using the current I_{max} and voltage V_{max} at the maximum power point from the I-V measurement as:

$$\eta = I_{max}V_{max}/P_i \tag{1.5}$$

1.1.3 Shockley-Quiesser Efficiency Limit

To determine the maximum conversion efficiency of the PV cells, in 1961, Shockley and Queisser proposed the detailed balance model on single junction cell from thermodynamics perspective, which became the most famous PV device design guide called Shockley-Quiesser limit. [8] In the detailed balance model, the assumptions are:

(1) The absorbing materials are perfect. It absorbs all the photons with energy larger than the bandgap and transmits the photons with energy below the bandgap. The material carrier mobility is infinite.

(2) The only loss mechanism of the cell is the radiative recombination. The cell, the sun and the environment are in equilibrium through the radiation transfer.

Later in 1980, Henry introduced graphical quantum-efficiency analysis with detailed balance model to study the multi-junction cells and the concentration effect. [9] This method outlined an intuitional guidance to improve the PV cells efficiency by adopting multi-junction cells structure and concentrating solar irradiance. The multi-junction approach improves the cell module efficiency mainly by expanding the photon absorption wavelength window and reducing the thermalization loss. The solar concentration approach improves the efficiency by reducing the dark saturation current I_o in equation 1.4, since I_o is proportional to the cell area.

1.1.4 Solar Concentration Thermodynamic Limit: Etendue

Since concentration of solar irradiance can increase the cell efficiency, and also reduce the cell materials usage and the related cost, it's beneficial to concentrate the sun light as much as possible. However, there is a thermodynamics limit for the highest achievable concentration level for a given light source, indicated by etendue conservation. [10] Etendue conservation states that in a lossless optical system in which there are no absorption, scatter, gain or Fresnel losses, the etendue shall remain constant. The significance of etendue is that rays can be determined by stating the positions and directions in phase space. [11] Etendue is a space concept defined in the phase space. According to the edge-ray theorem, the rays that are confined in the etendue after the reflection and refraction in the optical system, will still be confined by the same etendue conserved space. Thus the irradiance concentration can be described by the etendue conservation. If etendue ξ is calculated at the entrance pupil or exit pupil, it can be expressed as:

$$\xi = \int\int d\xi = n^2 \int\int \cos\theta dA d\Omega = n^2 \int\int\int \cos\theta dA \sin\theta d\theta d\phi \tag{1.6}$$

in which n is the refractive index at the pupil, A is the area of the puil, and Ω is the solid angle. In polar coordinates, solid angle $d\Omega$ can be expressed as $\sin\theta d\theta d\phi$, in which θ and ϕ are the polar angle and the azimuthal angle, respectively.

If assuming the solid angle is constant within the pupil area, and integrate the solid angle with θ from 0 to θ_a, and ϕ from 0 to 2π, then Equation 1.6 will be converted to:

$$\xi = n^2 \int dA \int_0^{2\pi} d\phi \int_0^{\theta_a} \cos\theta \sin\theta d\theta = \pi n^2 A \sin^2\theta_a \tag{1.7}$$

in which θ_a is called the semi-acceptance angle.

If etendue is inspected at both the entrance pupil (labeled with subscript i) and the exit pupil (labeled with subscript o), due to the etendue conservation, we can have:

$$\xi_i = \xi_o = \pi n_i^2 A_i \sin^2\theta_{ai} = \pi n_o^2 A_o \sin^2\theta_{ao} \Longrightarrow C = A_i/A_o = \frac{n_o^2 \sin^2\theta_{ao}}{n_i^2 \sin^2\theta_{ai}} \tag{1.8}$$

in which C is the concentration ratio. The maximum concentration ratio is given when $\theta_{ao} = \pi/2$, shown as:

$$C_{max} = \frac{n_o^2}{n_i^2 \sin^2\theta_{ai}} \tag{1.9}$$

Equation 1.9 shows that the more divergent the input light is, the more difficult it is to achieve a high concentration ratio. The beam divergence of the direct irradiance is determined by the sun's diameter (1.39×10^6 km) and the earth-sun distance (149.6

$\times 10^6$ km), which is 0.26° in semi-angle, called solar disk. If the circumsolar region is included, the input beam divergence is 2.5°. [5] The refractive index at the input n_i is always the refractive index of air as 1. Thus if assuming n_o=1 as in air, the maximum concentration ratio for direct irradiance concentration is 48563 if only consider the solar disk, or 526 if circumsolar is also included. The concentration of diffuse irradiance is much more complicated since the direct radiance can be approximated as uniformly distributed within the small angle spread, however, diffuse radiance distribution depends on many factors, which will be discussed in more details in Chapter 4.

Since etendue reveals the trade-off between the concentration ratio and the acceptance angle in a given optical structure, to evaluate the performance between different solar radiation concentrator design, the figure of merit is defined as concentration acceptance angle product (CAP), expressed as:

$$CAP = \sqrt{C}\sin\theta_{ai} = \frac{n_o \sin\theta_{ao}}{n_i} \tag{1.10}$$

To achieve high CAP value, there are two approaches, as indicated by Equation 1.10: (1) Immerse the output beam in high refractive index dielectric material; (2) Adopt advance optical design to expand the output beam to make θ_{ao} as close to $\pi/2$ as possible. Some non-imaging optics design methods are proposed for modern solar concentrator design, such as the flow-line method by Winston and Welford, and simultaneous multiple surface method by Minano and Benitez. [12, 13]

1.2 Concentrator Photovoltaics: Status and Challenges

The first PV device dates back to 1883, made by Fritts. Modern PV research started from 1954 in Bell Labs where the researchers fabricated the Si p-n junctions and achieved 6% efficiency. [14] After 30 years of research study, the PV industry began to mature with facilities manufacturing Si-based PV cells. [15] Since then, the PV

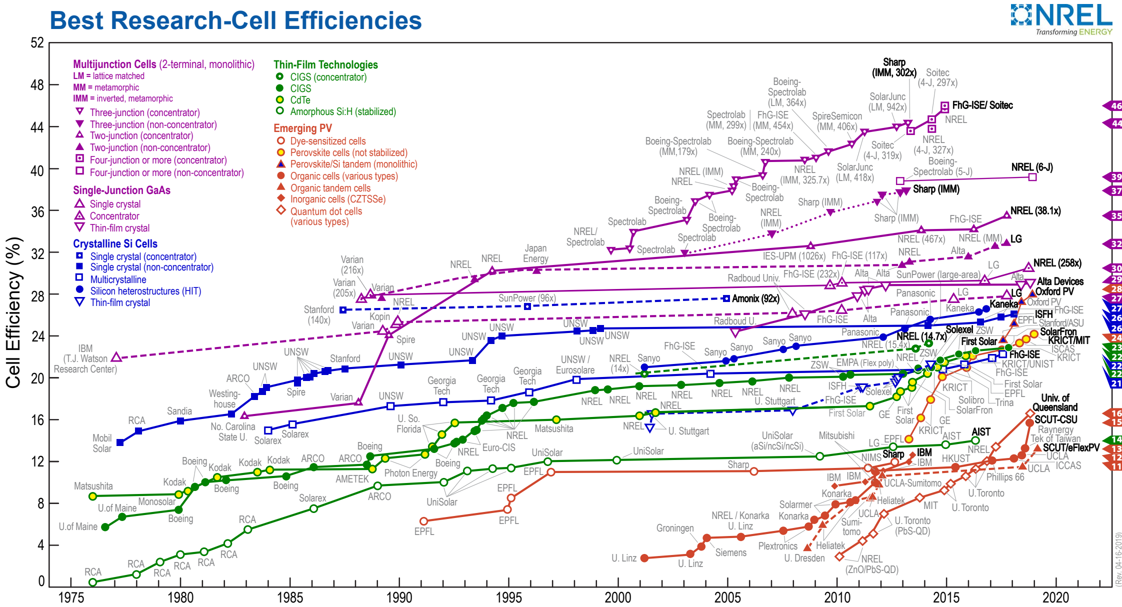

Figure 1-4: NREL cell efficiency records chart.

community have devoted innumerable efforts to develop new PV technologies and push for higher module efficiencies, as shown in Figure 1-4. [16] PV industry also has achieved great success. The world cumulative PV installation has been growing exponentially in the last three decades, and reached 404 GW in 2017, as shown in Figure 1-5. [17] Now the solar power have already accounted for 6.3% and 1.7% of installed capacity and electricity generation, respectively, in global energy market. [18] The dramatic growth mainly takes advantage of the rapid price reduction of Si panel PV, driven by scaling-up of PV deployment volume and technological advancements. Si panel PV has already accounted 95% share of the world production. [19] However, as the efficiency of Si PV reaches its practical limit, balance-of-system (BOS) costs gradually becomes the dominant challenge for continued price reduction which saturates the cost learning curve. [20] High-efficiency, low-cost PV modules beyond Si are therefore critical for further market penetration and can potentially enable a new price learning curve for solar energy technology.

By utilizing high performance multi-junction cells and concentrator optics, concentrating photovoltaics (CPV) systems can in principle reduce energy production costs by considerably reducing the usage of costly multi-junction cells. [21–25] In recent

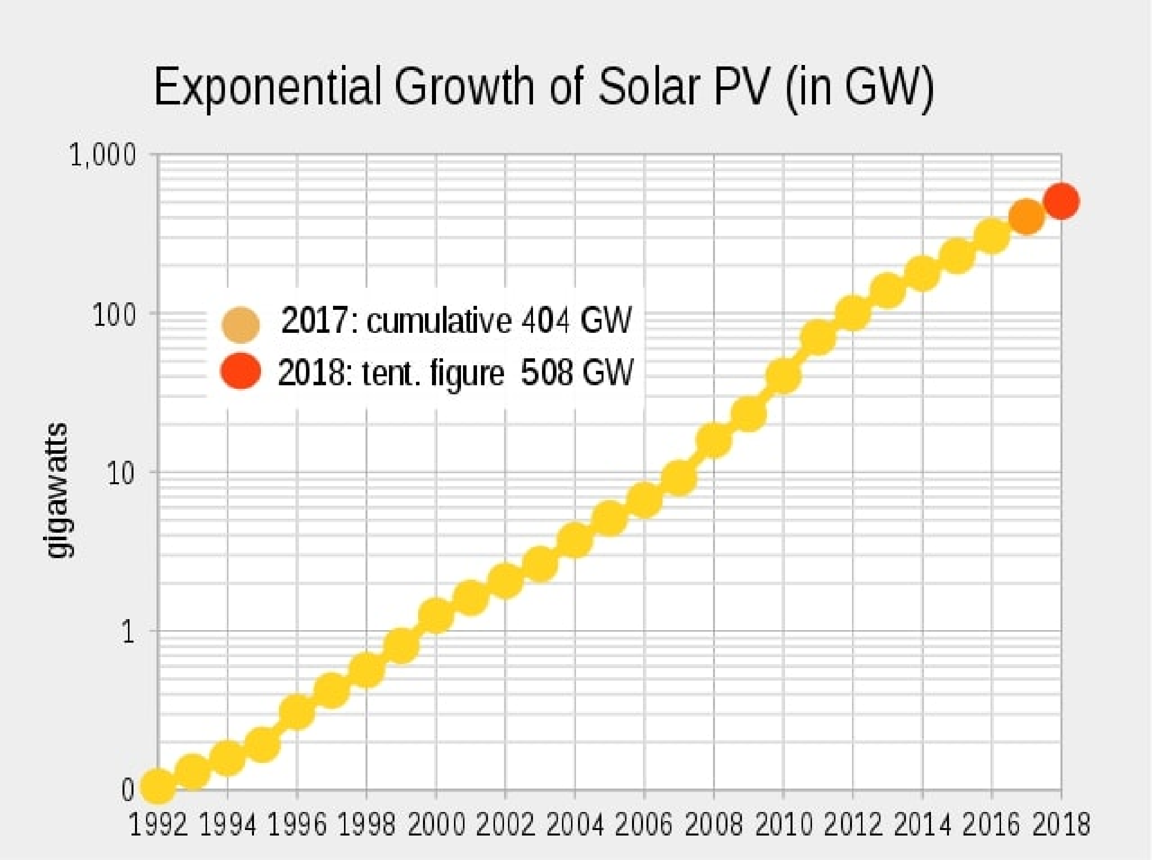

Figure 1-5: World cumulative installation of PV.

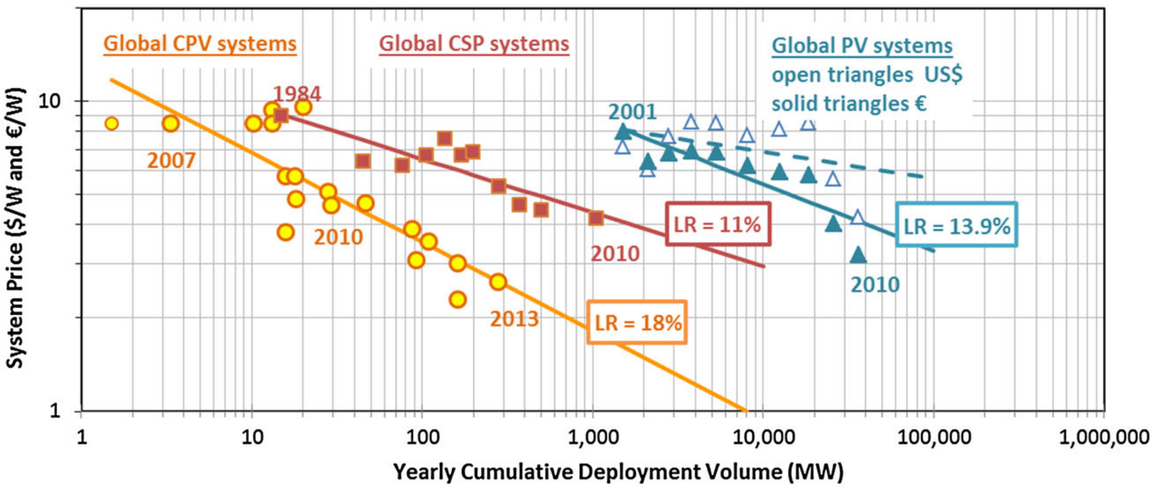

Figure 1-6: Learning curve plot for CPV and Si PV (labeled as Global PV).

years, the performance of CPV technologies has been advancing steadily, with cell and module conversion efficiencies reaching 46% and 43.4%, respectively. [26,27] The installation capacity of CPV has been steadily increasing before 2015. [21] Haysom et al. predicted and compared the learning curves of CPV and panel Si PV in 2015 as depicted in Figure 1-6, showing a bright future for CPV industry. [28]

However, currently CPV only occupies less than 0.1% of the global PV market. [19] It's not only due to the lower levelized cost of electricity (LCOE) of Si PV compared to CPV, [29,30] which mainly originates from the order of magnitude difference of the global deployment and industry scales, but also the intrinsic limits of the traditional CPV systems as listed below:

(1) Tracking requirement: Since CPV is using concentrator lens, a tracking system is required to consistently align to the sun. Traditional CPV systems usually deploy reflective mirrors or refractive Fresnel lens in meter-scale, which mandates high-precision heavy-duty trackers. Due to the high requirements and limited CPV production scale, the high initial investment barrier and prohibitive price has significantly hindered the CPV market growth.

(2) DNI-only harvesting capability: As discussed in Chapter 1.1.1 and 1.1.4, concentrators work most effectively with collimated light. Traditional CPV does not utilize diffuse radiation, which significantly limits the system deployment only

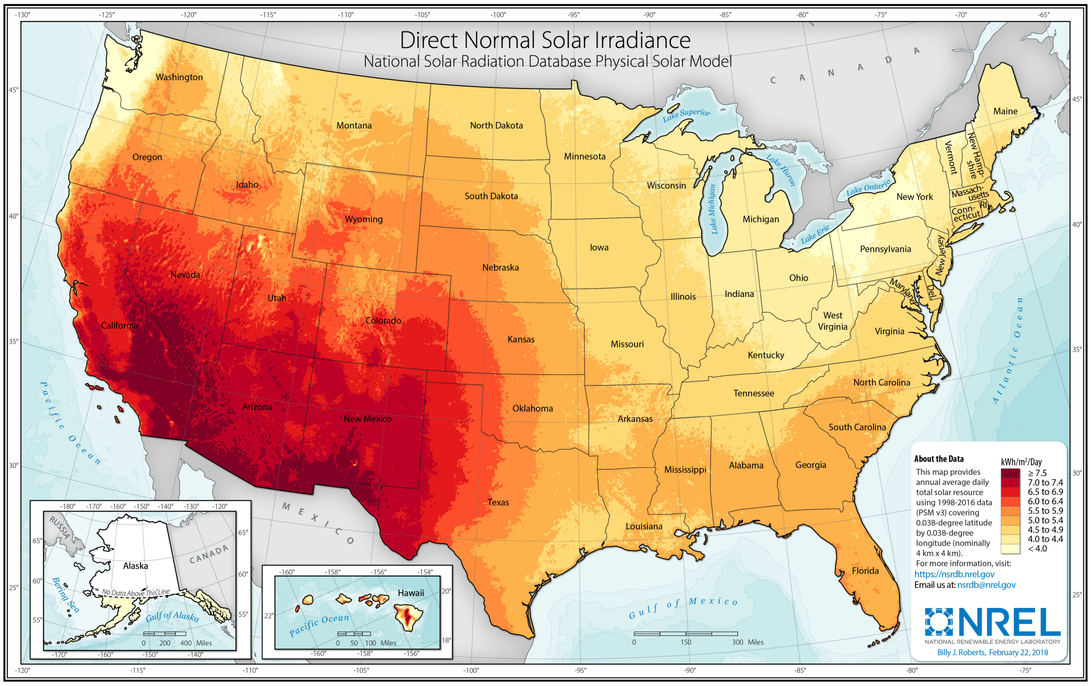

Figure 1-7: DNI abundance distribution map in USA.

within high-DNI regions, i.e. the southwest regions in USA, as depicted in Figure 1-7. [31] Besides, DNI is an extremely variable source of energy, [32] which increases the difficulties in power management and reduces the bankability of traditional CPV systems.

(3) Heat management: The concentration of solar irradiance leads to high density of heat when the concentration ratio is high. However, photovoltaic devices operate at higher efficiency in lower temperature environment. Besides, the cell lifetime can be significantly reduced if the temperature is high enough to melt solders or degrade resins. Traditional CPV requires heat sinks to provide significant cooling ability which adds up the system complexity and related costs.

Currently traditional CPV industry is facing the so called chicken-and-egg situation, [23] as these fundamental performance, reliability and cost issues are slowing down the scaling-up process of the industry, while the limited production volume in turn leads to slow cost reduction, which is essential for advanced CPV system deployment. New approaches are mandated for CPV to break out from this conundrum.

1.3 Promises of Micro Hybrid Concentrator Photovoltaics

The micro hybrid concentrator photovoltaics concept enabled a new breakthrough possibility for CPV system and received various attention in the research communities in the past few year. [33–35]

By drastically micronizing the cell area into the sub-mm region and shrinking the related optics footprint, micro CPV can successfully alleviate, even eliminate most of the fundamental limits of the traditional CPV systems. In the cell level, micro CPV exhibits superior cell performance. To effectively collect the photo-generated carriers, large-area cells need to pattern metal collectors on the top of the cells, which introduces 5% to 10% shading loss. In micro CPV, the metal fingerings are not mandatory when the cell aperture is comparable to the carrier diffusion length, thus eliminates the extra shading loss. In the module level, micro CPV replaces the large scale concentrator to mini lens arrays, and thus achieves more distributed heat. Besides, when the cell size decreases to hundreds of microns level, the surface area to volume ratio will be high enough to enable efficient heat dissipation so that the cell operation temperature is essentially the same to that in one-sun scenario. [34] Typically, micro CPV only requires passive, even no heat dissipation design which reduces the system integration difficulty and cost. Besides, traditional CPV often adopt large Fresnel lens as the primary concentrator to reduce the module weight. However, the Fresnel lens suffer optical losses due to draft angle and corner rounding issues. Micro CPV module adopts mini lens arrays instead, thus can gain extra 10% transmission. [34] In the system level, micro CPV has lighter and more compact system profile by utilizing thin mini lens arrays with small focal length. Thus the tracker does not have to be heavy-duty. Since micro CPV can achieve a panel-like module profile, it can gain leverage from the existing large scale Si PV industry by adopting their racking and trackers. It significantly reduces the initial investment requirement for micro CPV to scale up, providing a feasible route to break out from the chicken-and-egg dilemma.

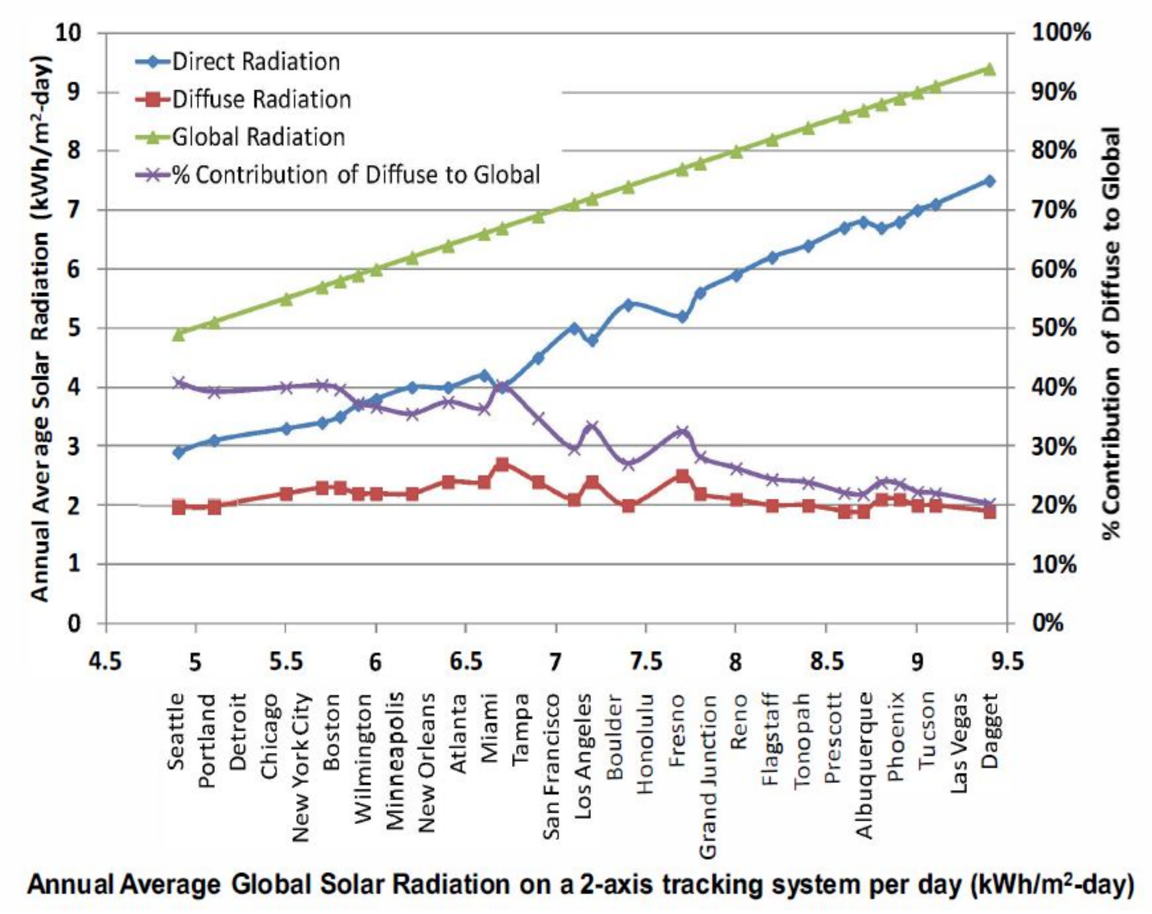

Figure 1-8: Annual average solar radiation in 2-axis tracking mode across the USA.

The hybrid CPV concept aims to expand the energy harvesting capability to include the diffuse solar irradiance. By introducing Si cells as the diffuse irradiance harvesting device, the hybrid CPV can effectively collect both the direct and the diffuse irradiance, expands the CPV system geographic locations from only the high-DNI southwest region to the whole USA, and increases the system adaptability to various weather types like cloudy and overcast. Haney et al. studied the micro hybrid CPV concept in 2014. [36] They showed that in 2-axis tracking mode, the diffuse irradiance ranges from 20% to 40% of the total global irradiance as shown in Figure 1-8, making it an unignorable part for photovoltaic applications. They also conducted the LCOE analysis to compare micro hybrid CPV and micro-only CPV within USA as shown in Figure 1-9, demonstrating maximum of 25% cost reduction by introducing the hybrid concept into micro CPV.

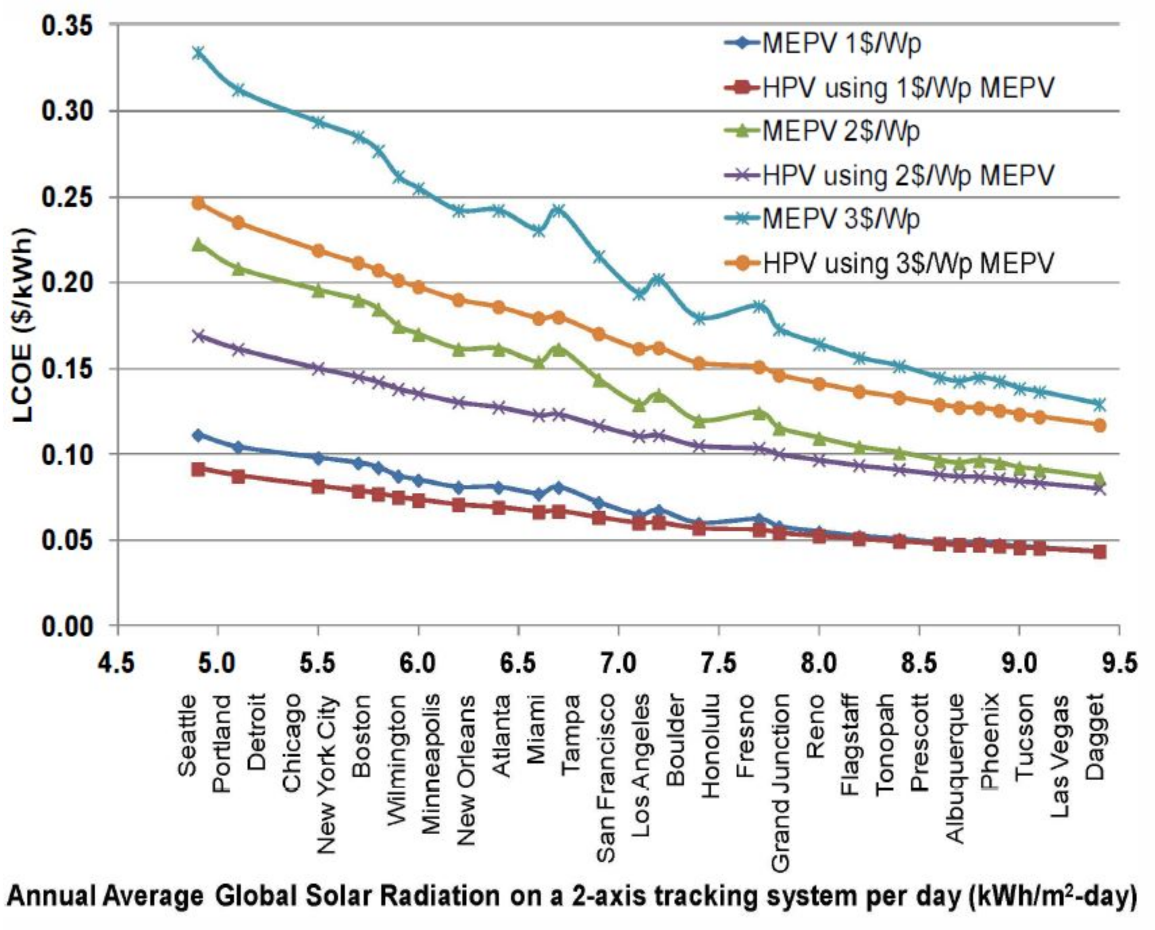

Figure 1-9: LCOE costs within the USA. Micro hybrid CPV and micro-only CPV are labelled as HPV and MEPV, respectively.

There have been some successful demonstrations of micro CPV and hybrid CPV modules, as shown in Figure 1-10. Panasonic demonstrated a monolithic integrated micro CPV module using 3-J cells that achieved 35.9% conversion efficiency. [37] However, their module does not have a secondary optics so the module CAP value is low. Semprius demonstrated a micro CPV module with balls lens as the secondary optics, thus improved the CAP to 0.52. Later they collaborated with UIUC team and added Si cell in the design to enable diffuse light harvesting capability. Besides, they developed the transfer printing technology which is essential to cost-effective large-scale micro CPV module production. [38, 39] The Universidad Politécnica de Madrid research group developed CPV module based on the Fresnel-RXI Köhler integration method and demonstrated measured CAP as 0.56 and design simulated CAP as 0.85. [40, 41] However, the complicated non-imaging optics design may face severe manufacturing difficulties when the cell size goes to sub-mm level. Price et al. developed micro CPV module by imbedding the tracking system into the module and demonstrated system field of view as 140° with over 30% system efficiency. [42] This compact system shows great potential in rooftop PV application. However, the internal tracking approach will inevitably increase the system integration complexity and the system cost. Hybrid CPV designs and modules have been demonstrated by a few research groups. [39,43–45] All of them adopted the same approach as introducing Si cells into the CPV-only module, and demonstrated a boost in efficiency, especially in low-DNI scenarios.

Currently, a cost-effective micro hybrid CPV architecture for large scale production is still under active research, since the system level cost is a complicated topic involving cell optimization, optics design, system integration and cost analysis, where a lot of trade-offs exist. Besides, different application scenarios, like utility-scale solar farm, rooftop PV and solar vehicles, require specific designed modules and systems. In order to reach or even surpass the cost learning curve of Si PV, the following performance attributes are demanded: 1) high performance multi-junction micro-cell arrays, 2) high efficiency, high concentration, and large field-of-view micro-optics that further reduce usage of semiconductor materials, simplify module design, and are tol-

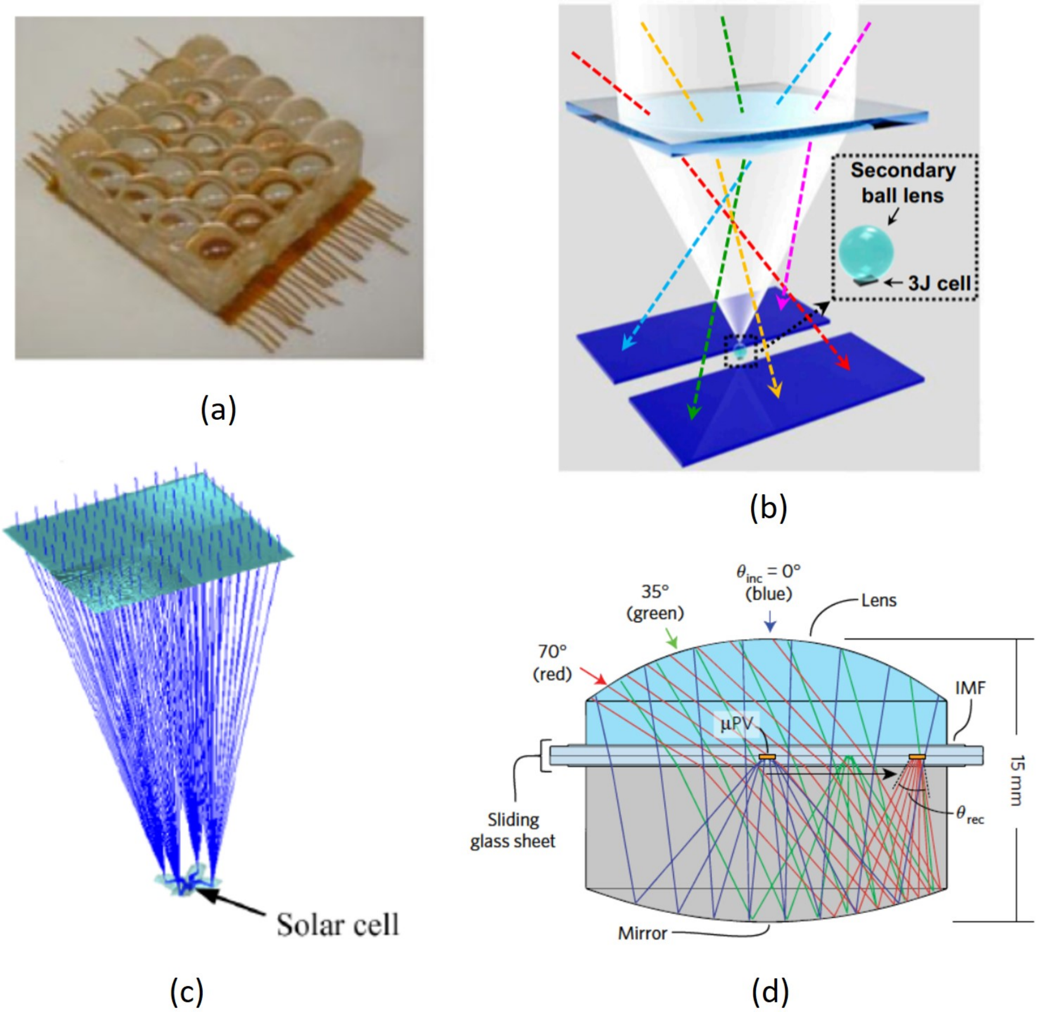

Figure 1-10: Existing micro CPV modules: (a) Panasonic micro CPV module; (b) Semprius and UIUC micro hybrid CPV module; (c) Universidad Politécnica de Madrid micro CPV module; (d) PSU micro CPV module.

erant to pointing accuracies of low-cost trackers (1° to 1.5° tracking accuracy), 3) high level integration of the components within a compact module to minimize assembly and operation costs, 4) the module fabrication and BOS must be compatible with current Si PV manufacturing in order to take advantages of the economy of scale, and 5) diffuse light should be captured in a cost-effective manner.

1.4 Outline of the Thesis

In this thesis, we focus on developing micro optics compatible to large scale production of micro hybrid CPV modules. We will introduce two optical elements: multi-functional Si platform and micro-prism-array spectrum splitting optics. These two optics have thin-profile and can be easily integrated into other existing CPV module designs.

Chapter 1 presents the motivation of developing micro hybrid CPV modules. In Chapter 2, we demonstrate the novel wafer integrated micro concentrator photovoltaics module concept based on the multi-functional Si platform. The fabrication process of the multi-functional Si platform and its outstanding optical and photovoltaic performance are presented. Our results show that it's a viable route to achieve state-of-the-art micro hybrid CPV module, demonstrating 0.68 concentration-acceptance-angle product. In Chapter 3, we design and prototype the novel spectrum splitting optics based on micro prism arrays for lateral-arrayed multi-junction cells. The optics features > 80 percent transmission, $< 8^o$ beam deflection angle and excellent spectrum splitting capabilities. Outstanding module performance is predicted using simulation approaches. In Chapter 4, we focus on construction of annualized diffuse radiance energy distribution model. The 2-axis simulation results indicates an optimistic results for diffuse concentrator design for cost-effective micro hybrid CPV module.

Chapter 2

Wafer Integrated Micro Concentrator Photovoltaics

Simply miniaturizing traditional CPV modules based on fabrication and module assembly techniques optimized for macro CPV is not a viable route to fulfilling the potential benefits of micro CPV. The scaling down of component size further limits the employment of efficient non-imaging or multi-stage optical concentrator systems that could bring performance close to the thermodynamics limit, since the fabrication and assembly of such components in either micro scale or large array is challenging and cost-prohibitive.

In this chapter, a new micro hybrid CPV concept is presented, aiming to radically improve PV system's cost effectiveness by further exploiting cell/optics scaling. The Wafer Integrated Micro Concentrator Photovoltaics (WPV) concept utilizes III-V micro-cells integrated with a novel multi-functional Si platform to fully leverage the high performance of multi-junction cells as well as module- and system-level benefits of Si flat-plate PV. The PV system designs are guided by a detailed cost model based

---

Work presented in this chapter has been published in:

"Wafer integrated micro-scale concentrating photovoltaics" Progress in Photovoltaics: Research and Applications, 26 (8), 651-658 (2018);

"Highly-integrated Hybrid Micro-Concentrating Photovoltaics", 2018 IEEE 7th World Conference on Photovoltaic Energy Conversion, (2018).

on industrial-scale fabrication processes that analyzes and predicts energy production costs. [46]

Here we demonstrate the design, fabrication, integration, and optical performance characterization of the multi-functional Si platform, which shows remarkable versatility for integration with different micro-cell and micro-optic architectures and significant improvement compared to conventional CPV approaches.

2.1 WPV: Module Concept

As schematically illustrated in Figure 2-1, the key notion of the WPV concept is a multi-functional silicon platform integrating high concentration multi-junction micro-cell arrays, cell interconnects and high performance micro-optical elements all embedded at the wafer level. The Si cell contains etched truncated pyramid-shaped reflective cavities that serve as efficient non-imaging micro-optical concentrators and alignment features for other micro-optical/mechanical components as illustrated in Figure 2-1 (b)-(d). The III-V cell is located at the bottom of the cavity, which provides concentration and increases the field of view of the entire optical system. It also improves the tolerance to fabrication errors and refractive index changes resulting from temperature variations. Anisotropic etching of standard 100 oriented silicon substrates exposes the 111 crystal planes to form truncated-pyramid-shaped rectangular cavities with facets of 35.3° slanting angle. The four sidewall facets of the cavity are coated with highly reflective metal films. Optical apertures of the cavities are precisely defined to match the micro-scale cells. The Si cell is also designed to capture and convert the diffuse and off-alignment sunlight which usually contribute to major optical losses in conventional CPV systems. As a result, the WPV approach seamlessly integrates multiple functionalities on an ultra-compact hybrid III-V-on-Si platform, including optical micro-concentration, hybrid PV/CPV photovoltaic, and mechanical micro-assembly.

As depicted in Figure 2-1 (b) and (c), a baseline WPV structure consists of: 1) a Si cell platform encompassing the reflective cavity arrays and cell interconnects, 2)

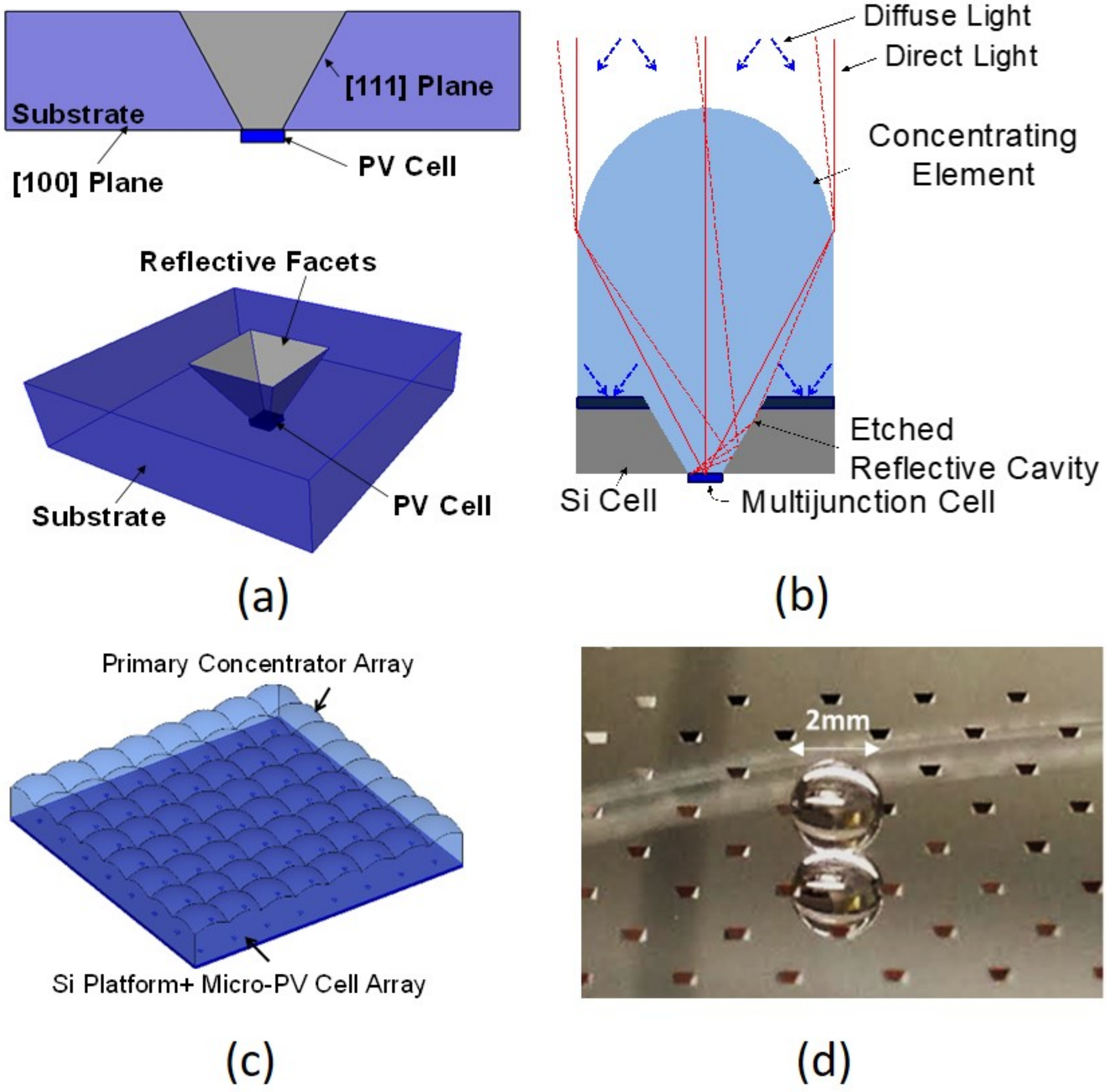

Figure 2-1: (a) A novel multi-functional Si cell platform that integrates an array of concentrated multi-junction micro-cells; (b) and (c) A baseline structure consists of a molded lens array layer, a multi-functional Si cell, and an integrated array of high concentration multi-junction micro-cells; (d) Self-aligned ball lens concentrator on a Si cavity.

a multi-junction micro-scale PV cell array integrated on the Si platform and aligned to the cavities, and 3) a primary concentrating optic array. Enabled by such wafer-level integrated micro-concentrators, the simple baseline WPV architecture yields prototype designs with concentration ratios ranging between 400X and 2400X while maintaining sufficient angular tolerances ($\pm 1°$ to $\pm 2°$) that are fully compatible with commercial low-cost trackers designed for Si PV (typically $1°$ to $1.5°$ tracking accuracy). Compared to high-precision trackers dedicated to CPV modules, Si trackers have less demanding accuracy requirements and their manufacturing can take advantage of the economy of scale to achieve considerably reduced costs($> 50\%$). [47] The Si platform with the cavities as on-wafer alignment features can be further integrated with a variety of single- or multi-stage optical concentrator architectures while maintaining a compact form factor. Analyses and experimental investigations described in later sections suggest the WPV approach can potentially leverage both the high performance of multi-junction cells and the low cost of flat plate Si PV infrastructures at the module- and system-levels.

2.2 Multi-functional Si Platform

2.2.1 Fabrication Process

The fabrication process for the multi-functional Si platform is schematically illustrated in Figure 2-2. The process starts with standard PV-grade double-side polished Si wafers with 280 µm thickness. The truncated-pyramid cavities were defined via anisotropic wet etching in an aqueous solution containing 36% KOH and 10% isopropanol (by weight) at 90 °C. Silicon nitride (400 nm thickness) deposited by plasma enhanced chemical vapor deposition (PECVD) was used as the etch mask. Other etch barrier materials were also tested, such as LPCVD nitride and thermal oxide. However, these high-temperature process will significantly degrade the carrier lifetime of the Si wafer, as indicated in Figure 2-3. The specific etching condition is optimized for generating smooth cavity sidewalls to minimize optical scattering loss.

After the KOH wet etch, standard HNA etch was conducted to remove 1 µm surface material, which was contaminated due to potassium ion diffuse, to recover the wafer carrier lifetime, as shown in Figure 2-3. The nitride mask was stripped in 7:1 buffer oxide etch (BOE) after the etching step and the wafer was subsequently encapsulated in a sputtered silicon nitride layer to prevent electrical shorting. Ti/Au interconnects, Ti/Au/Ni/Au (thicknesses: 25 nm/100 nm/100 nm/200 nm, from bottom to top) underbump metal, sputtered silicon nitride (400 nm thickness) solder dam, and solder metal (5 µm SAC305, a lead-free alloy that contains 96.5% tin, 3% silver, and 0.5% copper) for the multi-junction micro-cells were then sequentially patterned by contact photolithography and lift-off at the backside of the wafer. The interconnect and underbump metal layers were coated using electron beam evaporation whereas jet deposition was utilized to form the solder bumps. All these patterning steps were performed using dry film resist (Dupont MX 5020) to avoid the accumulation of resist in the etched cavities from the conventional spin coating technique. In the last step, the Si cavity sidewalls were coated with a 100-nm reflective silver metal film and a 150-nm silicon nitride protective layer to prevent oxidation of the metal coating. Multi-junction micro-cells can then be solder bonded to the Si piece (not depicted in Figure 2-4). Figure 2-4 (a) and (b) show photos of the front and back sides of the fabricated Si platform.

Resistivity of the interconnect metal wires was measured to be 3.1×10^{-8} ohm·m, consistent with literature values of gold resistivity. [48] Based on the resistivity data, two interconnect designs were modeled to evaluate the ohmic power losses in micro-scale CPV modules. In a test module with 2 cm by 2 cm aperture, there are 11 rows of micro-cells, each containing 9 individual micro-cells arrayed in a honeycomb lattice pattern. In the first interconnect design, the micro-cells in each row are first stringed in series, and then all rows are connected in parallel. In the second layout, all cells are connected in parallel. Figure 2-4 (c) compares the calculated fractional power loss from the test module due to ohmic resistance. While both design can achieve low power loss ($< 2\%$) with a moderate gold film thickness of 300 nm, the series design claims much reduced power loss due to the smaller currents in the interconnect bus

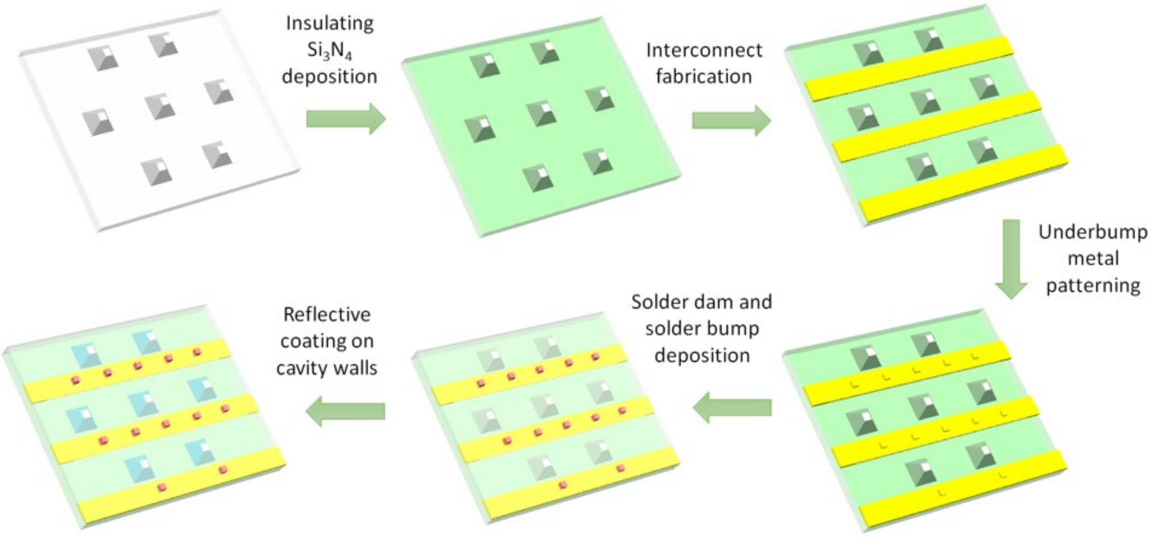

Figure 2-2: Schematic fabrication process flow for the multi-functional Si platform.

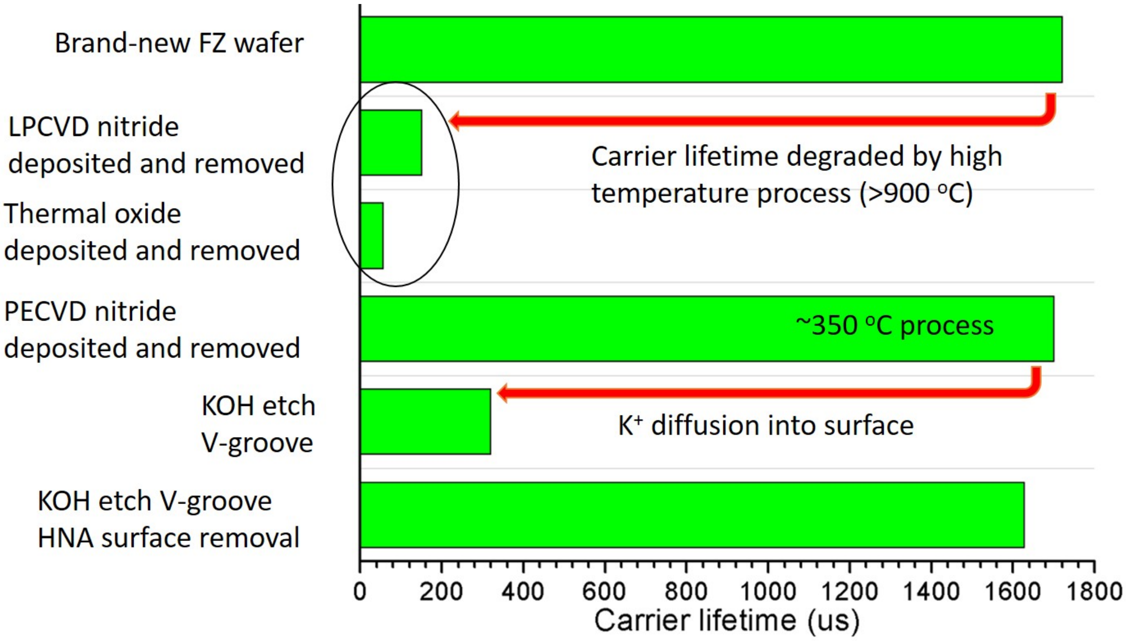

Figure 2-3: Carrier lifetime of the Si wafer after different processes.

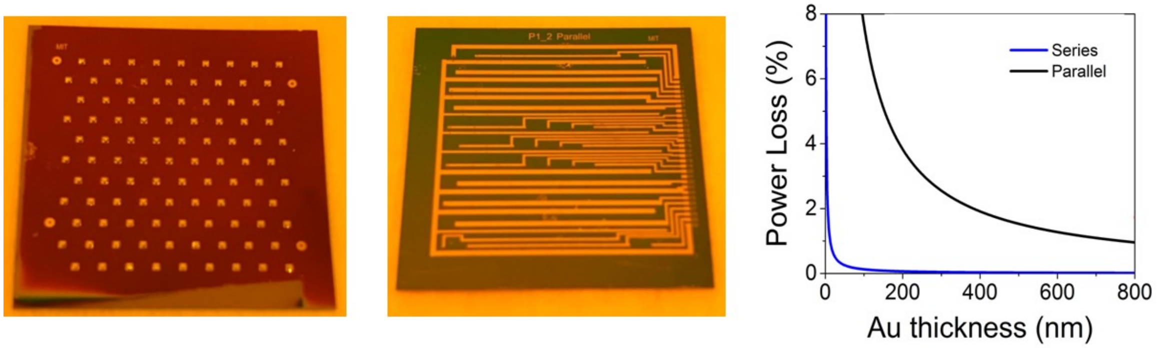

(a) (b) (c)

Figure 2-4: (a) Frontside and (b) backside photos of the Si platform with etched reflective cavities; (c) Simulated power loss due to ohmic resistance of interconnects: the two lines correspond two interconnect designs.

lines.

The etched Si cavity sidewall quality was examined using white light interferometry (WLI). In the experiment, the etched Si wafers were cleaved along the [110] direction passing through the cavities, which divided the cavities in halves, as shown in Figure 2-5 (a). SEM and optical microscopy were used to evaluate the control of etched cavity size, showed well matching to the 100 µm by 100 µm III-V cells, as illustrated in Figure 2-5 (b) and (c). The cleaved sample was then mounted onto a custom-made tilted sample holder such that one of the cavity's four sidewalls lies in the horizontal plane to facilitate the interferometry measurement. Figure 2-5 (c) shows the exemplary surface morphology of the cavity sidewall characterized by WLI. The measurement yields an average RMS roughness value of (10 ± 2) nm, introducing negligible scattering loss and thus minimum impact on the cavity's concentration performance when sunlight is incident on the sidewalls from the filling material (e.g., PDMS).

The results above indicate that the Si etched cavity platform fabricated using standard micro-fabrication protocols projects adequate optical and electrical performance for micro-cell array integration.

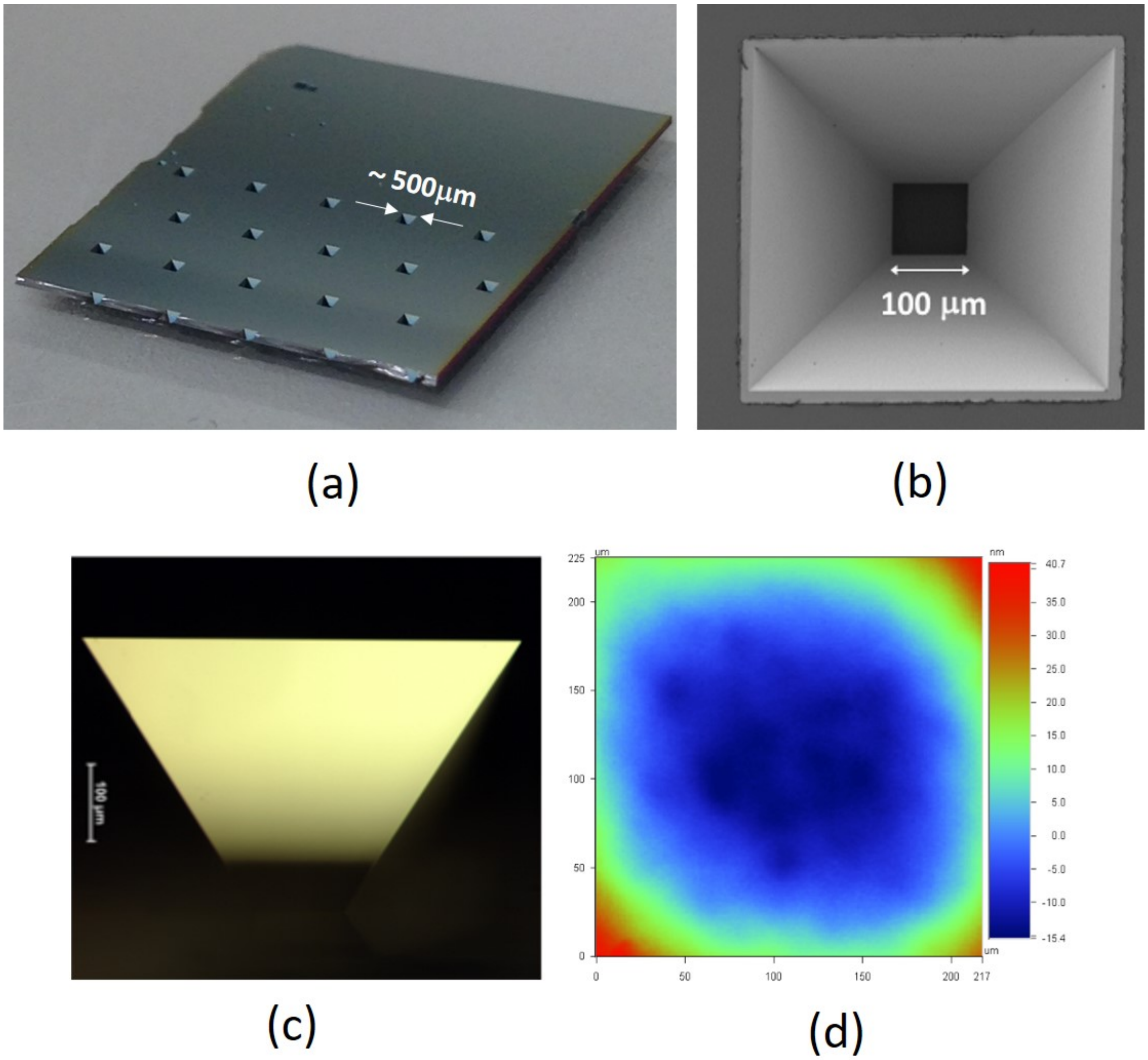

Figure 2-5: (a) Cleaved Si wafer with etched cavity arrays; (b) top view of an etched Si cavity after metallization; (c) side view of an etched Si cavity; (d) surface morphology of the Si cavity sidewall measured using white light interferometry.

2.2.2 Photovoltaic Performance Demonstration

The etched Si wafers were fabricated into interdigitated back contact (IBC) solar cells by Institute of Energy Conversion (IEC). After the wafer cleaning and HF etching, the wafers were passivated by the stack layers of PECVD deposited $a - Si : H$ based thin films. The front passivation layer consists of 8 nm intrinsic $a - Si : H$ followed by 80 nm $a - SiN_x : H$ and 20 nm $a - SiC : H$ layers. This stack structure provides excellent surface passivation with anti-reflection properties. The back surface passivation stack consists of 8 nm thick intrinsic $a - Si : H$ followed by 30 nm n-type $a - Si : H$ and 80 nm $a - SiNx : H$ layers. The IBC cell fabrication was completed with e-beam evaporated interdigitated Al metal contacts, as shown in Figure 2-6 (a). The J-V performances were measured under AM1.5 illumination and at room temperature of 25 °C, and presented in Figure 2-6 (b). The IBC cell open circuit voltage, short circuit current density, fill factor and efficiency are 0.626 V, 35.7 mA/cm^2, 58.4% and 13.0%, respectively. Corrected with the cavity area, the true cell efficiency is 14.3%, which is comparable with the 14.8% efficiency value of IBC cell without through-hole cavities. [49] It suggests that introducing cavity as secondary concentrating optics features in Si wafer will not degrade its photovoltaic performance, and multi-functional Si platform is a viable route to enable hybrid solar energy harvesting function in micro CPV module. By improving the fabrication process and introducing texture features, the IBC cell can potentially achieve 25% efficiency. [50]

2.2.3 Optics Performance Demonstration

The etched Si cavity plays a critical role in simultaneously improving the concentration ratio and acceptance angle of a micro-CPV module with minimally added module complexity and costs. The optical performance of the Si platform is characterized by optically coupling the reflective cavity to an off-the-shelf N-BK7 ball lens concentrator, as shown in Figure 2-7 (a). The optical transmission of the ball lens concentrator under different light incident angles is measured with and without

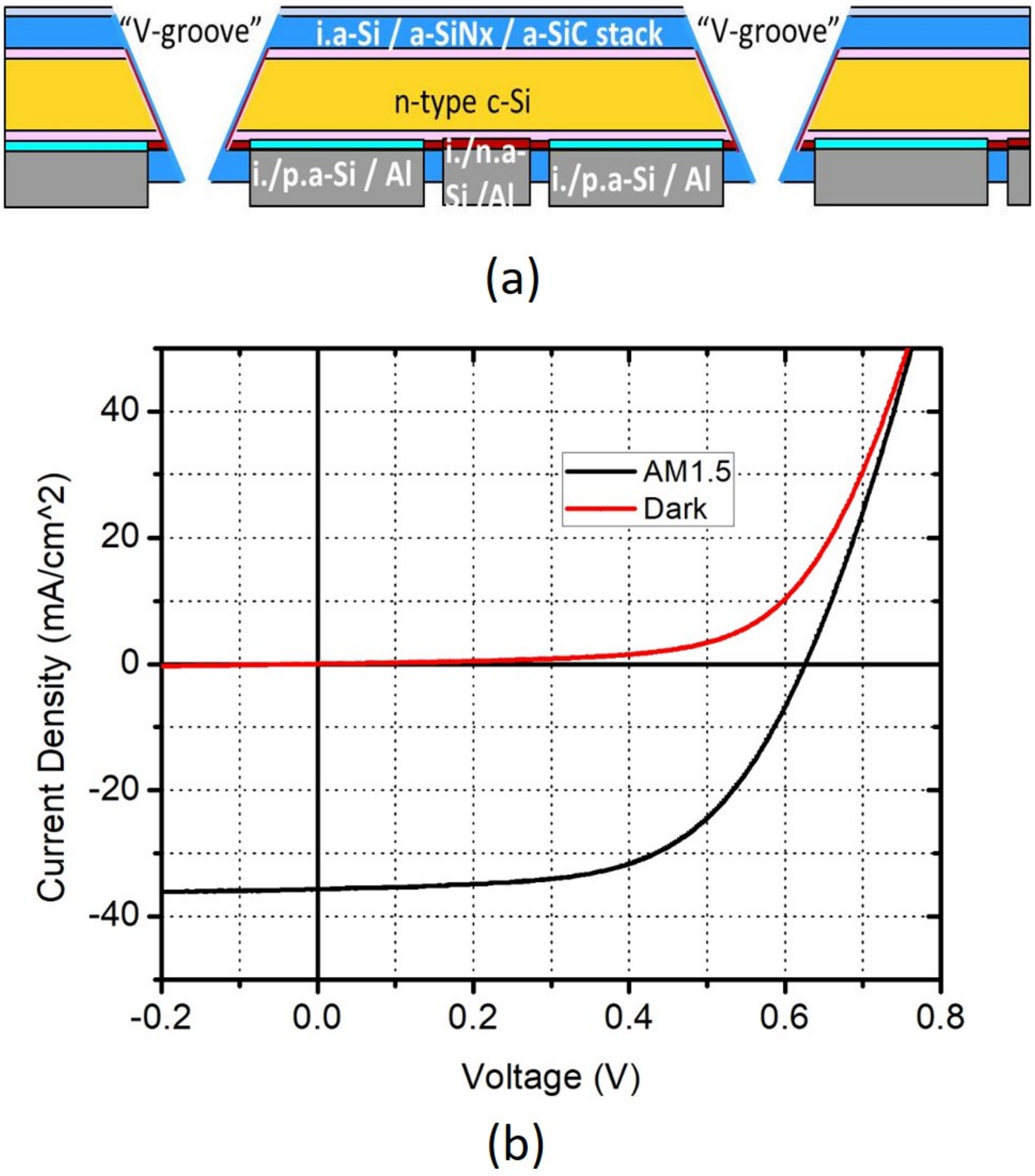

Figure 2-6: (a) Schematics of the IBC cell of the WPV module; (b) J-V measurement results of the IBC cell under AM1.5G and dark environment.

integration with the Si reflective cavity attached to an off-the-shelf photodetector (PD). In order to emulate the micro-cell in the ball lens only measurement, an etched Si wafer is mounted reversely on the PD to act as a shadow mask that defines the 100 µm × 100 µm input optical aperture of the PD. The experimental setup is shown in Figure 2-7 (b). A fiber bundle light source is used to provide simulated direct normal sunlight with a divergence angle of approximately ± 0.25°. The light source assembly are mounted on a custom-designed circular rail stage so that the beam's incident angle on the tested module can be precisely adjusted for angular response measurements. The ball lens and Si platform are mounted on linear-translation and tilt stages for alignment between the components.

The experimental results are shown in Figure 2-7 (c), and compared with simulation results obtained from a ray-trace simulation model. At normal incidence, optical transmittances of 90.9% and 90.1% are measured for optical systems with and without the Si reflective cavity, respectively. The optical losses are primarily attributed to Fresnel losses at the non-AR-coated ball lens surface. Compared to simulation results, the experimental results indicate that the Si cavity enhances light collection by redirecting scattered light from the primary lens surfaces back to the cell region. The measured angular sensitivity further shows that acceptance angles (defined as the angular range with larger than 90% of on-axis power) of ± 2.39° and ± 1.14° are obtained for the optical systems with and without the Si cavity, respectively, indicating that the etched Si cavities significantly increases the angular tolerance of the baseline optical system.

The optical performance characterization results thus suggest that over 100% improvement on the concentration-acceptance-product is achieved by integrating the Si reflective cavity with a conventional optical concentrator. The mechanism for such CAP improvement can be explained by the increased incidence angle (with respect to the micro-cells) of light after reflection at the cavity sidewalls. The increased angular spread of incident light rays allows enhanced spatial confinement of incident light (i.e. higher concentration ratio) according to the étendue conservation principle, leading to an improved CAP metric.

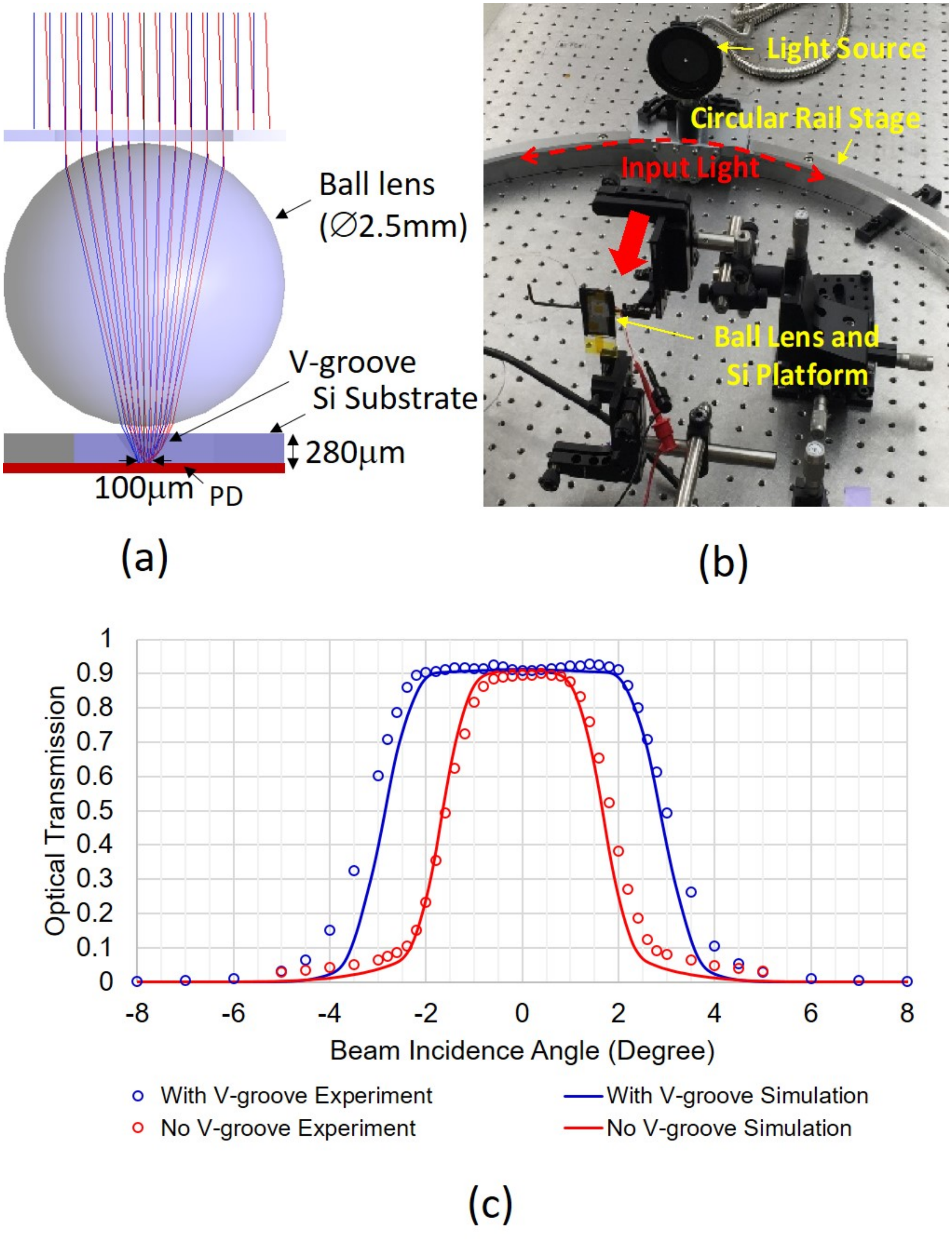

Figure 2-7: Optical performance characterization of etched Si cavity: (a) Optical simulation model; (b) Experiment setup; (c) experimental vs. simulation results indicate over 100% improvement on acceptance angle and CAP by incorporating the low-profile Si cavity into a traditional optical concentrator system.

It should be noted that it is very challenging to accomplish such improvement cost-effectively by conventional optical concentrators due to the limited f number of refractive elements and the significant fabrication challenges of making non-imaging elements at the micro-scale and in a large array format. On the contrary, the proposed WPV approach directly embeds such critical micro-optical elements in the wafer level, an approach suited for large scale manufacturing.

2.3 WPV Module Performance

As schematically depicted in Figure 2-8 (a) and (b), the baseline prototypical module comprises a Si platform, an array of InGaP/GaAs micro-cells with 100 µm square apertures hybrid-integrated on the Si platform, a middle glass plate and an aspheric PDMS primary lens array (2.5 mm sub-lens diameter) directly molded on the glass. The micro-lenses, Si cavities, and micro-cells are arranged in hexagonal arrays to attain a 400X concentration ratio. The baseline structure is designed to have an acceptance angle of ± 2.2° (>90% of on-axis power), corresponding to a CAP of 0.77, while the same optical system without the reflective Si cavities has an acceptance angle of ± 1.33° according to our simulations. Furthermore, with a CAP of 0.77 the baseline WPV design can be adapted to a 2000X concentration at a ± 1° acceptance angle.

For component characterization and optimization purposes, our first prototype consists of two middle glass plates that hold the molded lens array and Si platform on their top and bottom surfaces, respectively. When assembled, they provide the same total effective optical path length as the design with a single middle glass plate. The primary PDMS lens array is molded on the glass and packaged in a Macor frame protected by a front cover glass, as shown in Figure 2-8 (c). The thickness of the optical system is less than 3 mm. The hybrid integration process of cells is demonstrated by flip-chip bonding micro-cell arrays to the interconnects on the Si platform via solder bumps. The resulting III-V-on-Si platform is further bonded to a glass with PDMS as an adhesive layer as well as filler in the Si cavities. A test

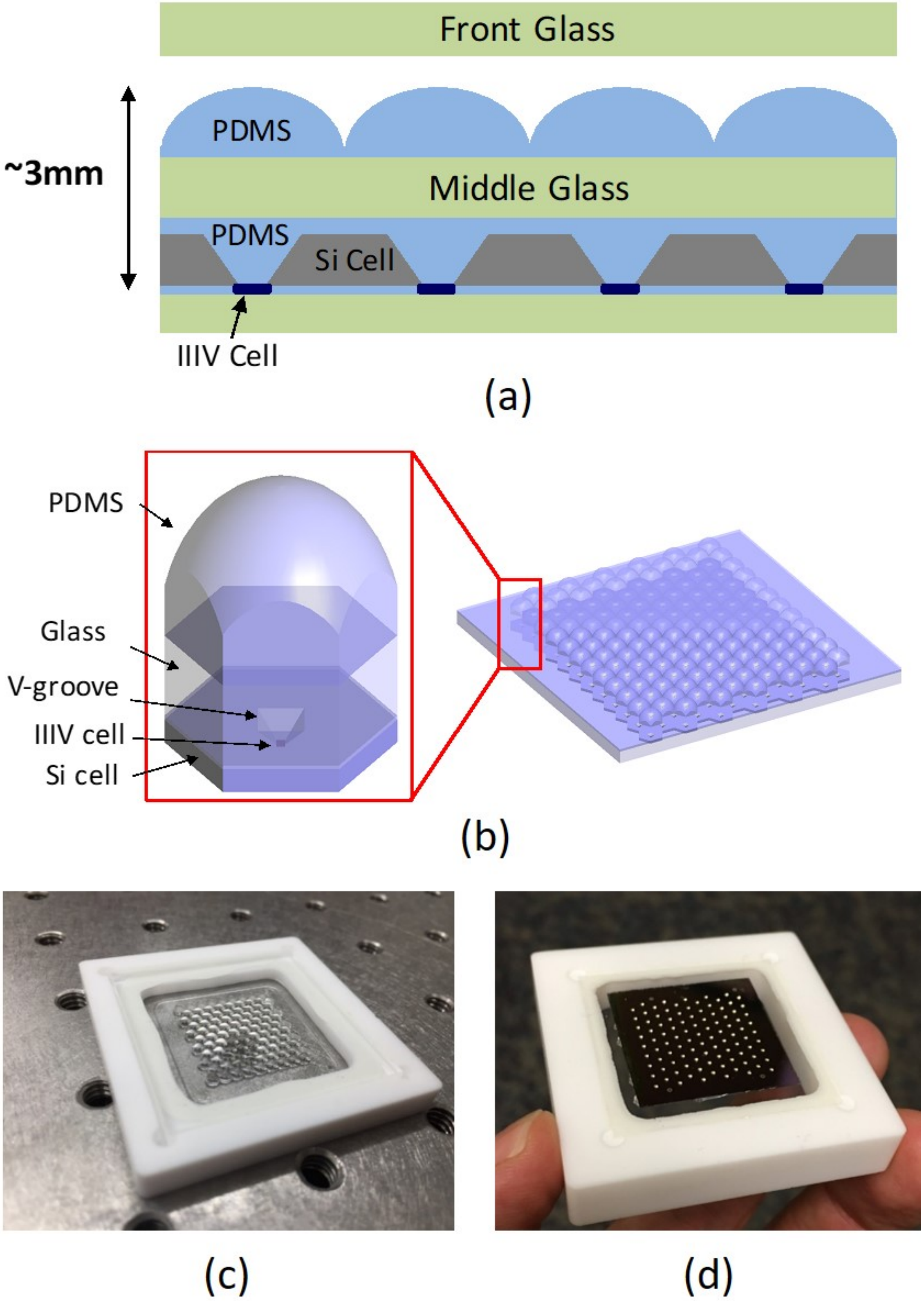

Figure 2-8: (a) Schematics of baseline prototype module; (b) Baseline optical design; (c) Injection molded PDMS lens array packaged in a Macor frame; (d) Hybrid integrated III-V-on-Si platform bonded on glass.

piece after the integration process is shown Figure 2-8 (d). The lens array was then aligned to the III-V-on-Si cell platform.

To ensure the optical coupling between the micro lens array and the cell platform, the molded PDMS lens array is characterized with the setup shown in Figure 2-9. The light source is a collimated expanded laser beam at 635nm. The Si photodiode is assembled with a 5 µm pin-hole aperture to work as a pixel sensor. The pixel sensor is mounted on a 3-way stage, controlled by LabView, so the focal spot profile can be reconstructed by data processing. The measured focal spots profiles are plotted in Figure 2-10 (a)-(c). The focal spots are recorded at positions as focus- 80 µm, focus and focus+ 80 µm, respectively. The encircled energy plots of the focal spots are plotted in Figure 2-10 (d). The FWHM at the focus is only 5.8± 0.9 µm. The measurement results show that the focal spots are well confined in the Si cavity output aperture, which is 100 µm × 100 µm, with a depth of focus > 160 µm. The focal spots of different lenses are measured and compared in encircled energy plot, as shown in Figure 2-10 (e), showing highly repeatable focal spot profiles. The measured back focal length is 689.6± 37.5 µm, in agreement with the ray-tracing simulated value 705 µm. The optical characterization results indicate that the PDMS lens array can be effectively integrated with the cell platform and deliver the design performance.

The first-generation assembled prototype module was mounted on a two-axis tracker (Figure 2-11) and its acceptance angle was measured on-sun under a clear sky. Figure 2-12 (a) shows the dependence of the output optical power on the incident angle of sunlight. Acceptance angles of ± 1.94° are measured for >90% of on-axis power. Compared to the simulation model (i.e., black curve in Figure 2-12 (a)), there is a good agreement to the simulated ± 2.2° acceptance angle, except a gradual roll-off of the transmitted power. The roll-off is due to imperfections of the cavity side-walls such as dirt contamination and bubble traping during the PDMS filling process, which can be eliminated in future improvements. Compared to the simulated ± 1.33° acceptance angle of the without Si platform case, the introduction of the Si reflective cavities demonstrated improvement of the CAP value by 46%, from 0.46 to 0.68, thereby validating the performance improvement conferred by the

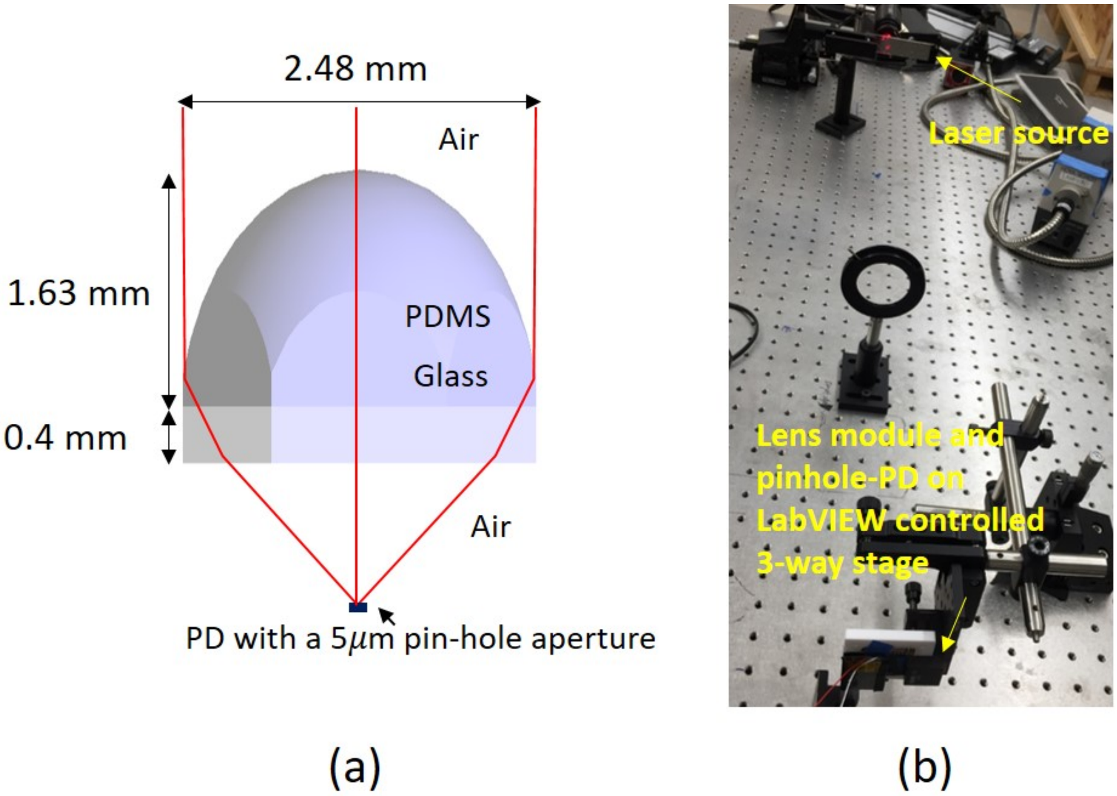

Figure 2-9: (a) Schematics of the micro lens array focal spot characterization setup; (b) Micro lens array focal spot setup. The pixel sensor is mounted on the LabView controlled 3-way stage for scanning measurement.

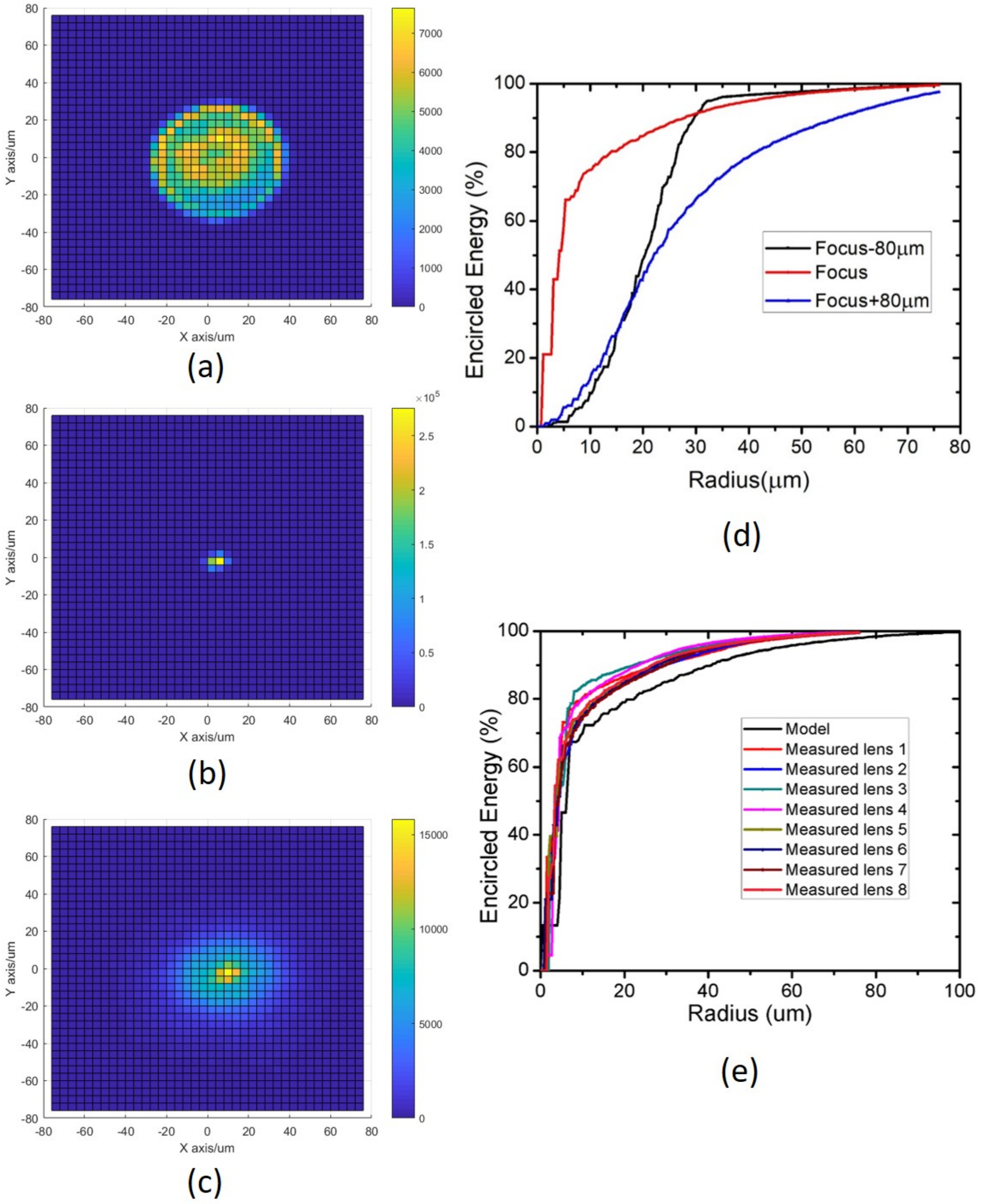

Figure 2-10: (a)-(c) Focal spots of the lens array recorded at focus- 80 µm, focus and focus+ 80 µm, respectively; (d) Encircled energy plots of the focal spots in (a)-(c); Encircled energy plots at focus comparison of measurement and design simulation.

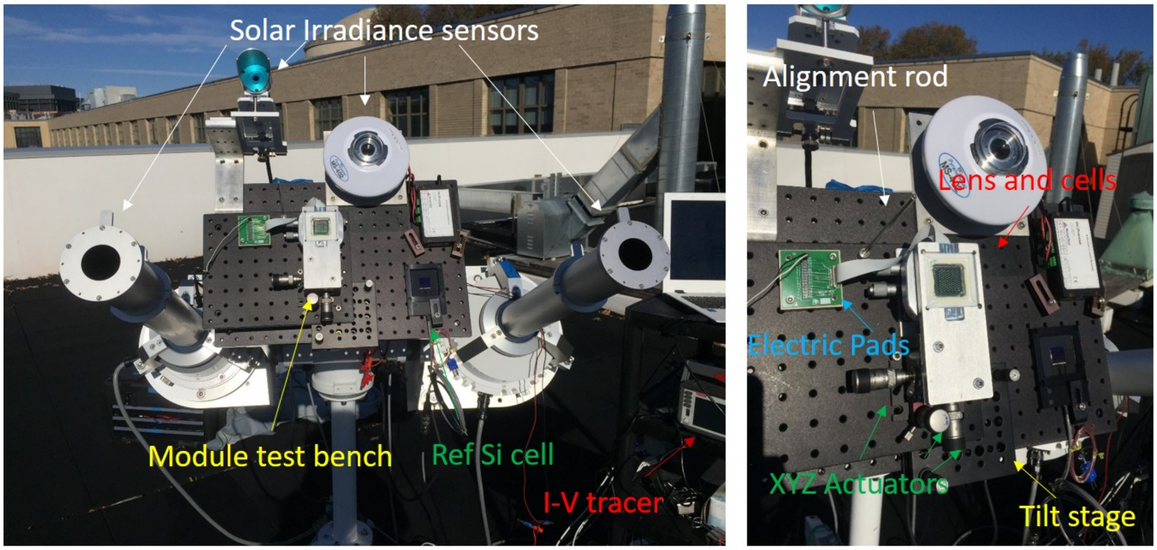

Figure 2-11: On-sun measurement setup: the assembled prototype module was mounted on a two-axis tracker.

Si platform. The WPV prototype module CAP value is compared with other state-of-the-art flat CPV modules in Figure 2-12 (b), showing that our module concept can indeed achieve exceptional solar irradiance concentration performance. [51]

The performance of the micro hybrid CPV baseline design is projected by optical simulations under solar irradiation with a variety of direct/global irradiation ratios, representing different geological and weather scenarios. [52] The optical system is modeled and simulated using 3D non-sequential Monte Carlo ray-tracing under a combination of direct and diffuse light sources. The optical transmissions of the optical system onto the concentrated III-V cell and the non-concentrated Si cell are plotted against the DNI/Global ratio, as shown in Figure 2-13. Assuming state-of-the-art 4-junction cells are used (40% DNI module conversion efficiency), the overall conversion efficiency of the hybrid module is projected based on the optical simulation results and compared to a CPV-only case, also shown in Figure 2-13. It is clearly shown that between Direct/Global irradiation ratio of 0.75 and 0.6, the hybrid module provides a conversion efficiency improvement of 17% to 33% from the CPV-only case. In particular, the hybrid module is projected to achieve an efficiency over 30% for low DNI regions (i.e., regions with 60% DNI) that were typically considered not suitable for conventional CPV deployment.

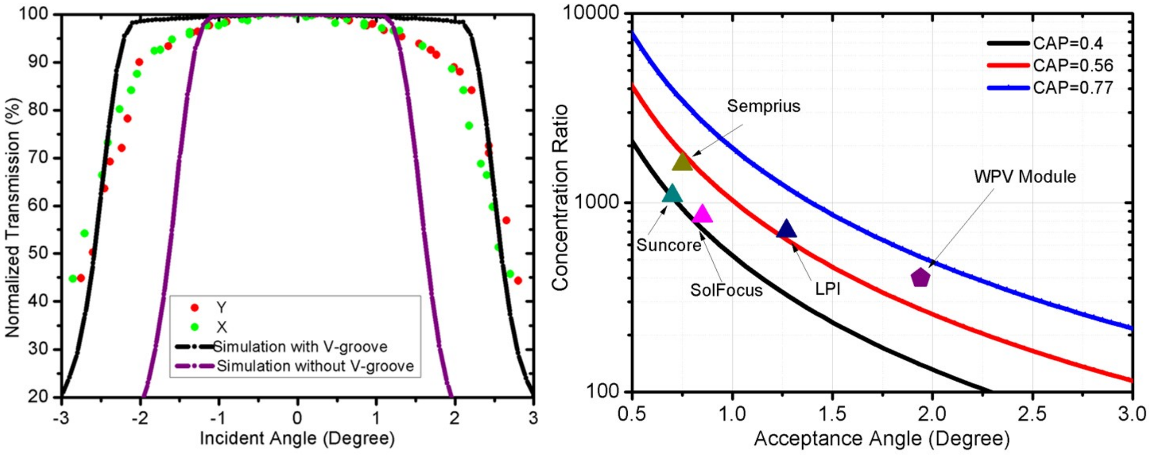

(a) (b)

Figure 2-12: (a) Acceptance angle measurement result vs. simulation model; X and Y represents the measurement results on two perpendicular directions; (b) WPV CAP comparison with other state-of-the-art flat CPV modules.

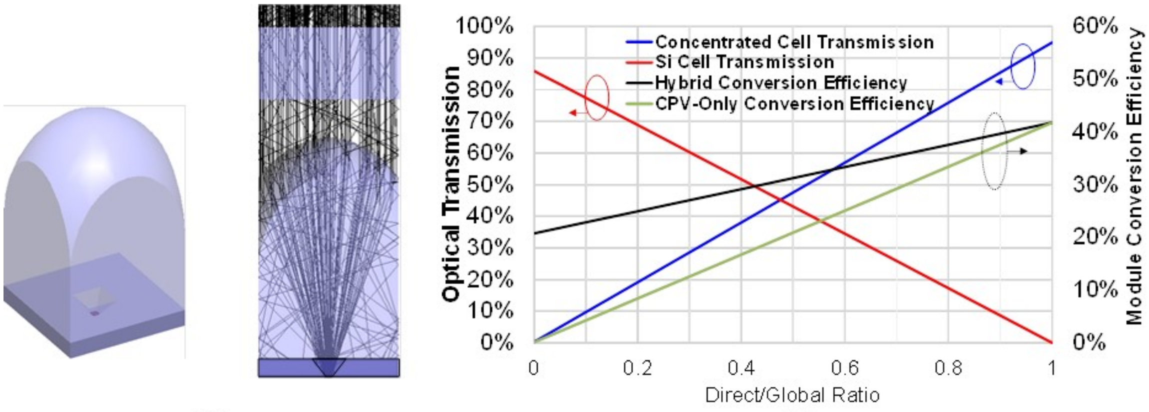

(a) (b)

Figure 2-13: (a) 3D Monte Carlo ray-tracing simulation model of a baseline design under simulated direct and diffuse light; (b) Optical transmissions and conversion efficiency of the hybrid module vs. Direct/Global Ratio. The simulation result of the hybrid module is compared to a CPV-only case of the same concentrator without the Si cell. Blue line: optical transmission on III-V micro-cell; red line: optical transmission on Si cell; black line: calculated overall conversion efficiency combining contributions from both III-V micro-cell and Si cell; green line: calculated conversion efficiency from the III-V micro-cell only.

2.4 Conclusion

In this Chapter, a novel micro-scale integrated hybrid CPV concept is proposed and developed, which tightly integrates multi-junction micro-cell and micro-optical concentrator arrays on a multi-functional Si platform. The Si platform simultaneously provides micro-optical concentration, hybrid photovoltaics, and micro-mechanical assembly functionalities. The wafer-embedded Si cavity concentrator is experimentally shown to provide 46% improvement on the concentration-acceptance-angle product, leading to considerably reduced module costs, sufficient angular tolerance to low-cost trackers, and an ultra-compact flat-plate form factor. The development of a baseline prototype module and its optical performance characterization are described. The performance of the proposed approach under combined direct and diffuse irradiation is modeled and projected, indicating that the hybrid PV/CPV architecture can effectively extend the geographic and market domains for cost-effective PV system deployment. Leveraging low-cost micro-fabrication and high-level integration techniques, the micro hybrid CPV approach is capable of seamlessly combining the high performance of multi-junction cells and the low costs of flat-plate Si PV systems.

Chapter 3

Micro-Prism-Array Spectrum Splitter for Laterally-Arrayed Micro CPV

In this chapter, we are focusing on introducing a spectrum splitting optics based on micro-prism arrays. The conjugate micro-optics design delivers high-transmission, efficient spectrum splitting with minimum aberration, low-profile, and low-cost fabrication, thus allows large scale production of laterally-arrayed multi-junction micro concentrator photovoltaic modules. A dispersive optics prototype based on a 4-prism design is fabricated and characterized showing excellent agreement with our design model.

Work presented in this chapter has been published in:

"Compact spectrum splitter for laterally arrayed multi-junction concentrator photovoltaic modules" Optics Letters, 44 (13), 3274-3277 (2019);

"Micro-Prism Spectrum Splitting Optics for Lateral-Arrayed Multi-Junction Micro CPV", 2019 IEEE 45th Photovoltaic Specialists Conference, (2019);

"Spectrum Splitting Micro-Concentrator Assembly for Laterally-arrayed Multi-Junction Photovoltaic Module", CLEO: Applications and Technology, AW3O.3, (2018).

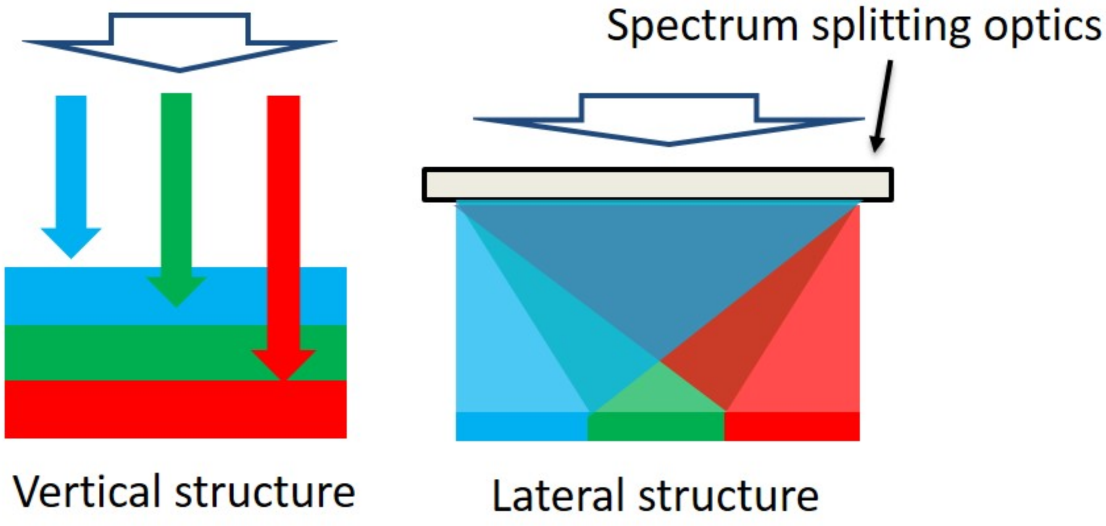

Figure 3-1: Schematics of vertical and lateral multi-junction cells structure.

3.1 Introduction

Under the guide of Shockley-Queisser limit, a multi-junction structure is essential to expand the solar spectrum collection coverage and increase the photon utilization efficiency to achieve highly efficient solar cell modules. The tandem cells with a vertical multi-junction structure has gone through a successful development and already achieved 46% efficiency in a 4J design. [53] However, the traditional vertical multi-junction cells module structure refrains further development of more efficient module.

3.1.1 Lateral Structure Vs Vertical Structure

So far most CPV technologies rely on traditional multi-junction tandem cells. It adopts a vertical structure that use the material absorption selectivity to separate the photons, as shown in Figure 3-1. However, since the vertical structure is based on epitaxial growth, it imposes the following limits:

(a) Lattice matching: Fabrication of tandem cells is typically based on epitaxial growth which mandates lattice matching. To reduce material defects and achieve good current tunneling, the junction materials must be chosen according to the bandgap-

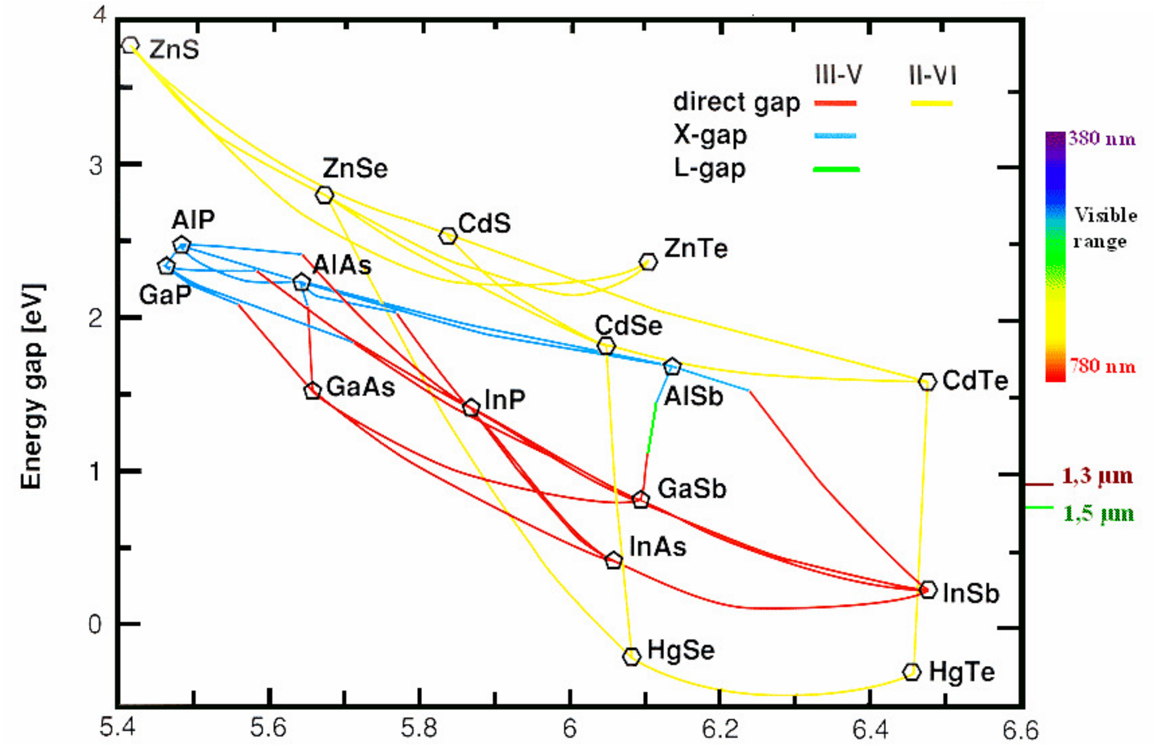

Figure 3-2: Bandgap and lattice constant diagram.

lattice-constant diagram, as shown in Figure 3-2. [54] This significantly limits the choices of the materials, complicates the cell fabrication process and raises costs. The constraint also limits the maximum number of cells that can be embedded in a multi-junction cell module, which bounds the maximum module efficiency.

(b) Current matching: The tandem junctions are connected in series so the module current is limited by the lowest-current junction. It significantly complicates the design procedure since the cell structure, materials property and power electronics are convoluted. Tandem cells are usually optimized according to the Standard AM1.5D spectrum. [7] However, in real outdoor environment, the direct irradiance and spectrum will vary significantly due to the weather and time variation. Broderick and et al. has conducted a simulation study to compare the performance of 3-J cells module in vertical and lateral structure. [55] It shows that the exquisite tandem cell design can slightly outperform the lateral cells during the solar noon time, when the spectrum is close to the standard solar spectrum AM 1.5D. However, lateral module will significantly outperforms the vertical module due the spectrum red shift near the sunrise and sunset. It shall be noted that mechanical stacking multi-junction cells are proposed to surmount the two problems and have shown successful research demonstrations. [56–60] However, this approach still has complicated cell structure and introduces issues like electrical wiring difficulties. [61]

(c) Optical losses through junctions: The multi-layer vertical structure reduces optical transmission of photons reaching lower-bandgap cells due to Fresnel loss and materials absorption, as the number of junctions grows.

Unlike tandem cells, a laterally arrayed cell design uses spectrum splitting optics to allocate photons onto sub-cells with corresponding bandgap energies, as shown in Figure 3-1. Since spectrum splitting is decoupled from the other design considerations, the cell design and materials can be optimized at will to maximize the module efficiency. Advanced interconnect schemes and power electronics can be developed to optimize the maximum power-point tracking on the independently connected cells. [62–67] Thus, the lateral cell architecture can potentially deliver better module performance and enhanced annualized energy output compared to tandem cells. [55]

3.1.2 Existing Spectrum Splitting Optics

The most critical component to realize the lateral multi-junction cells module is the spectrum splitting optics. An effective spectrum splitting optics must have the following features to enable a cost-effective micro CPV module: (a) High optical transmission to achieve high module efficiency; (b) High broadband spectrum splitting efficiency, since the solar irradiance covers a wide wavelength range; (c) Low-cost scalable production for commercialization; (d) Cost-effective module fabrication and assembly processes. The requirements (a)-(c) are self-explanatory. (d) is due to the fact that micro CPV use cells in the size of hundreds of microns. Thus, the module assembly becomes an extremely important issue in micro CPV system. Transfer printing technology developed by the Rogers group uses a elastomer stamp to transfer micro-scale devices from the native substrate to the target substrate. [68] It has already demonstrated over 99% process yield with 1.5 µm placement accuracy on applications like OLED displays, micro LED and micro III-V cells. [69] Semprius has been applying

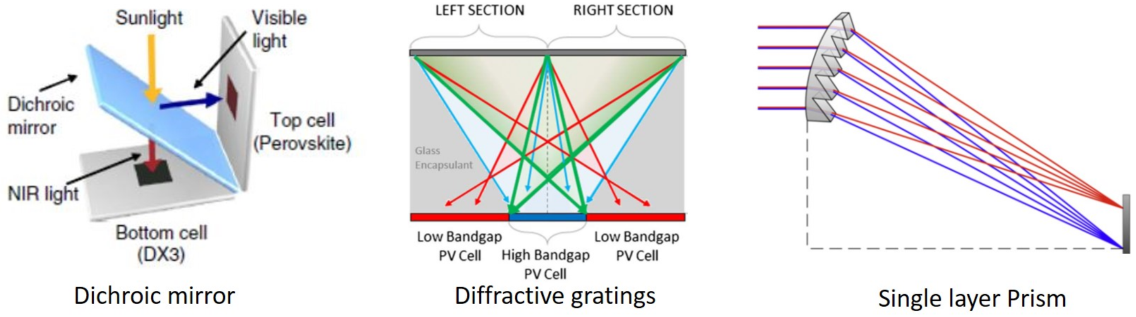

Figure 3-3: Existing spectrum splitting optics techniques: Dichroic mirror, Diffractive gratings and single layer prism array.

it on their HCPV module assembly and showed promising results. [70–72] Thus, it is currently the most promising method for large-scale cost-effective micro CPV module assembly.

Spectrum splitting optics based on dichroic mirrors, [73–75] diffractive gratings, [76–78] and single-layer prisms [79, 80], as shown in Figure 3-3, have already been implemented in CPV applications. Splitting optics based on dichroic mirrors demand complicated module designs with individually assembled sub-cells and optical components, making them incompatible with high-throughput assembly processes like transfer printing. Grating optics allow co-planar positioning of sub-cells but suffer from strong wavelength selectivity and limited spectral splitting efficiency (typically in the range of 40% to 70% when operating with broadband sources [61]). Both dichroic mirrors and gratings also entail high fabrication and assembly costs. The single prism approach, on the other hand, introduces off-axis beam deflection, which leads to severe aberrations and spectral mismatch on lateral sub-cells.

3.2 Micro-Prism-Array Spectrum Splitting optics

3.2.1 Optics Design Concept and Prototype

Here we demonstrate a planar dispersive optics design based on micro-prism arrays that uniquely deliver high transmission and minimal aberration, as schematically depicted in the Figure 3-4 (a) inset. The optics design concept is similar to the

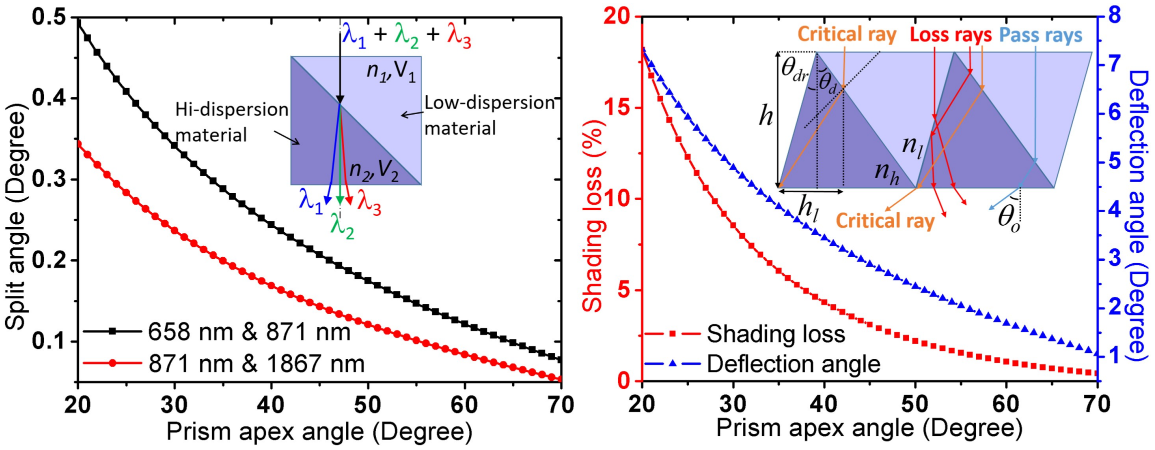

(a)

(b)

Figure 3-4: (a) Split angle between 658 nm & 871 nm and 871 nm & 1867 nm at different prism apex angle; Inset: optics design concept schematics; (b) Shading loss and deflection angle of 550 nm at different prism apex angle of 2-prism spectrum splitting layer; Inset: 2-prism assembly and loss mechanism schematics.

Amici prism. A spectrum splitting layer consists of two conjugate micro-prism arrays made of different materials. The two materials exhibit large Abbe number contrast to enhance spectrum splitting power while having similar refractive indices to minimize overall beam deflection. In the current design, the high- and low- dispersion materials are chosen as polycarbonate (PC) (V-number 30, refractive index 1.584 at 550 nm wavelength) and Zeonex (V-number 51.79, refractive index 1.532 at 550 wavelength), respectively. Its ultra-thin and planar profile facilitates seamless integration of the spectral splitting element with either conventional CPV modules or emerging micro-CPV designs. The dispersive layer can be fabricated in the form of large-area optical sheets via commercial plastic molding with low cost, enabling scalable manufacturing and deployment of the optics.

Here we start with analytically evaluating the optical performance and loss mechanisms in the bi-prism assembly. The prism height, nominal prism apex angle and the draft angle are labelled as h, θ_d and θ_{dr} and are illustrated in Figure 3-4 (b) inset, respectively. The draft angle is a mold feature used to facilitate part release,[81, 82] which is assumed constant at different prism height and prism apex angle. The design goals are high transmission, low beam deflection angle and large split angle.

Assuming the rays first enter the low refractive index (n_l) Zeonex layer then the high refractive index (n_h) PC layer, the beam deflection angle θ_o of the normal incident ray can be calculated by using Snell's law as Equation 3.1:

$$\theta_o = \arcsin(n_h \cos(\theta_d + \arcsin(\frac{n_l}{n_h} \cos\theta_d))) \tag{3.1}$$

The split angle is the deflection angle difference between rays of two different wavelengths.

In our design, we seek to maximize the spectrum splitting angle and meanwhile minimizing the beam deflection angle to suppress aberration for optimal spectral matching to sub-cells.

The main loss mechanism in the 2-prism assembly is the shading loss which encompasses three components: (1) draft angle shading loss which happens when rays are reaching the side surface with a non-zero draft angle and get deflected; (2) corner rounding scatter loss, which occurs at the prism tips rounded due to mold design and fabrication imperfection: the first two loss components can be mitigated effectively by improving molding precision; (3) shading loss due to total internal reflection (TIR), which happens when a portion of the beam refracted from the first prism surface incidents upon the prism side surface. It shall be noted that TIR shading loss can be avoided if the rays first enter the PC layer. However, if stacking structure is deployed for higher split angle, TIR shading loss will still be inevitable. A critical ray is indicated in Figure 3-4 (b) inset, which serves as the boundary between the transmitted and lost portions of the total incident beam. By applying Snell's law to the prism geometry, the shading loss η is expressed as Equation 3.2:

$$\eta = \frac{h_l}{h(\tan\theta_d + \tan\theta_{dr})} = \frac{\tan\theta_{dr} + \frac{\sin\theta_d \cos(\theta_{dr}+\theta_d+\arcsin(\frac{n_l}{n_h}\cos\theta_d))}{\cos\theta_{dr}\cos(\arcsin(\frac{n_l}{n_h}\cos\theta_d))}}{\tan\theta_d + \tan\theta_{dr}} \tag{3.2}$$

If the draft angle is close to zeo, then η is simplified to Equation 3.3:

$$\eta \approx \frac{\cos\theta_d \cos(\theta_d + \arcsin(\frac{n_l}{n_h}\cos\theta_d))}{\cos(\arcsin(\frac{n_l}{n_h}\cos\theta_d))} \tag{3.3}$$

As a design example, the split angles between 658 nm, 871 nm and 1867 nm (The 3 wavelengths correspond to the bandgaps of InGaP, GaAs and Ge cells), [55] the simplified shading loss and the deflection angle at 550 nm are plotted versus the apex prism angle in Figure 3-4 (a) and (b) for the 2-prism assembly. The results show that while larger apex angle gives rise to enhanced spectral splitting, overall beam deflection leading to aberration and shading loss also increase.Besides the prism apex angle, the other important design parameter is the prism height h. Smaller h produces a thinner optics profile conducive to small-form-factor modules and reduced material absorption. However, for a given corner rounding radius, the total scattering loss inversely scales with h. Corner rounding radii of less than 5 µm are commercially attainable with high-quality, large-area compression molding, which corresponds to a negligible scattering loss of <0.7% when the prism height h is 100 µm or above.

The spectrum splitting can be further increased by stacking more 2-prism layers. Since each layer has its own shading region, in-plane alignment of these shading regions is critical to achieving high transmission. The shading loss of a 4-prism assembly at different lateral shift is simulated using non-sequential ray-tracing model with 550 nm source of 0.25° semi-divergence angle, as shown in Figure 3-5. The minimum shading loss occurs when the shading regions of the two layers are aligned. Such alignment becomes increasingly important with larger draft angles.

We fabricated prototypes based on four prism layers following the design insights detailed above. The prism array is designed with h = 0.9 mm and $\theta_d = 50°$. A base layer with thickness of 1mm is added to provide mechanical support, although in an optimized design the base layer thickness can be considerably reduced while maintaining adequate mechanical strength. The micro-prism arrays were fabricated leveraging commercial compression molding (Isuzu Glass Ltd.) Since standard PC exhibits UV-induced coloring, UV-stabilizers were added to improve long-term stability of the optics. Compression molding takes over $10000 for initial molding fee. However, as the production scale increases, the average cost for each optical element will be significantly reduced. [82] Thus, our spectrum splitting optics design is suitable for large scale production.

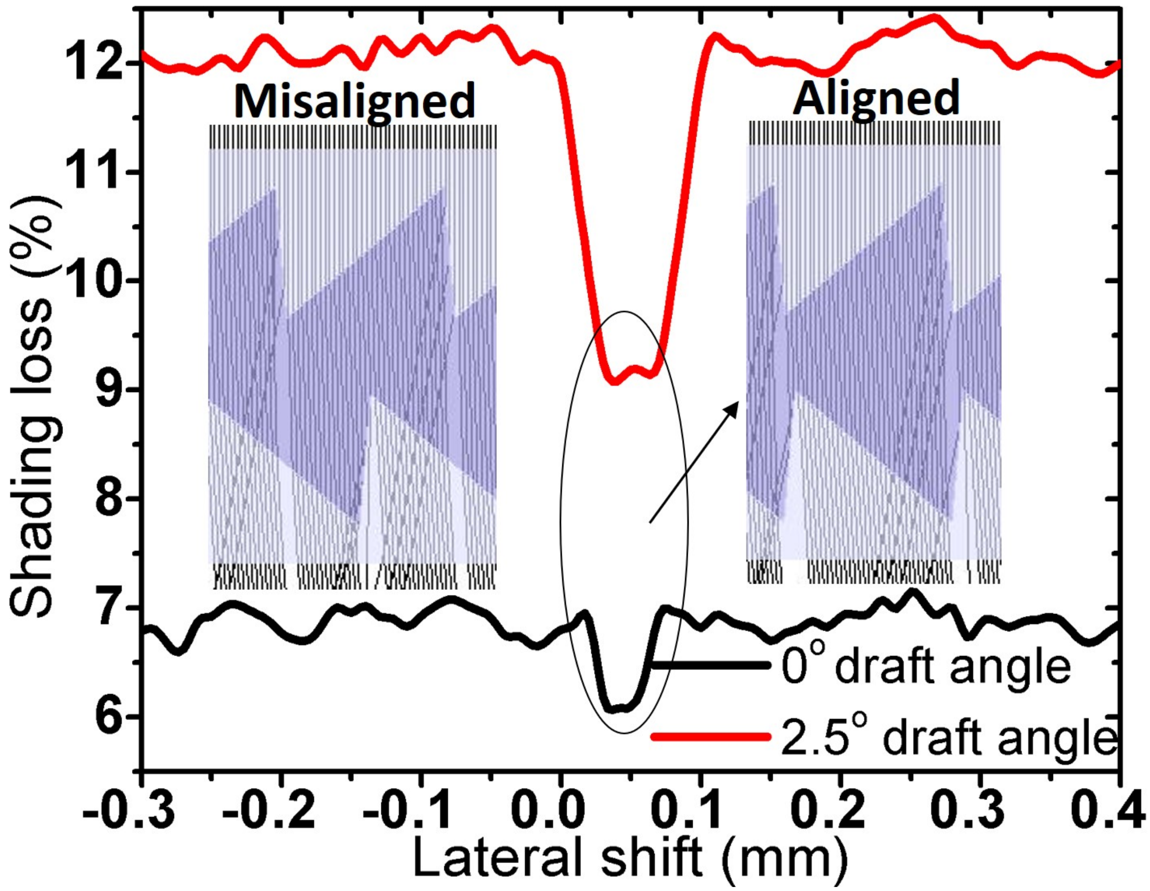

Figure 3-5: Shading loss of 4-prism assembly Vs lateral shift; Inset: ray-trace schematics of aligned and misaligned status.

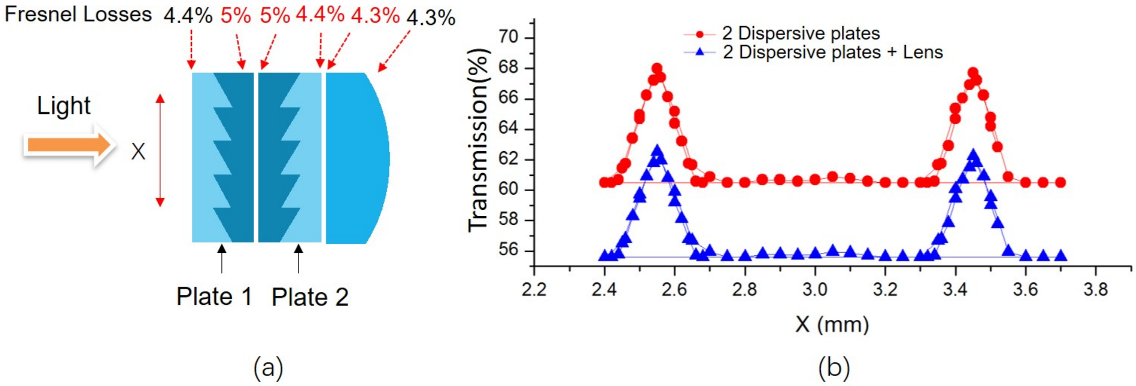

Figure 3-6: (a) Alignment measurement setup schematics; (b) Alignment measurement results; X indicates the lateral shift between the two spectrum splitting layers; 2 Dispersive plates case transmission is corrected from 2 Dispersive plates + Lens case with the transmission of the focus lens.

Experiments were carried out to characterize the alignment effect. The setup schematics is shown in Figure 3-6 (a). Two 2-prism layers were stacked without optical adhesive. The relative lateral shift (X) between the two spectrum splitting layer was controlled using translational stages. A focus lens was used to focus the transmitted light onto a calibrated Si photodiode (Thorlabs, FDS 1010). The transmission is calculated by normalizing the light intensity to the case without dispersive optics and lens, as shown in Figure 3-6 (b). The transmission peak occurs when the alignment of the draft angle shading region is achieved. And the peak has a lateral shift intervals as 0.9 mm, which agrees with the prototype prism pitch 0.9 mm value. To simplify the assembly process, the two middle prism layers are monolithically molded as a single part with a pre-defined lateral shift in the updated prototype. An index-matching optical adhesive (Norland 86, refractive index 1.55 at 550 nm wavelength) was applied to eliminate Fresnel losses in the 4-prism prototype.

3.2.2 Optics Performance Demonstration

To evaluate the performance of the prototype optics, the physical profiles of the prism were examined since they are highly correlated to the transmission performance, as discuss in Chapter 3.2.1. The prism finish surface was measured with AFM and

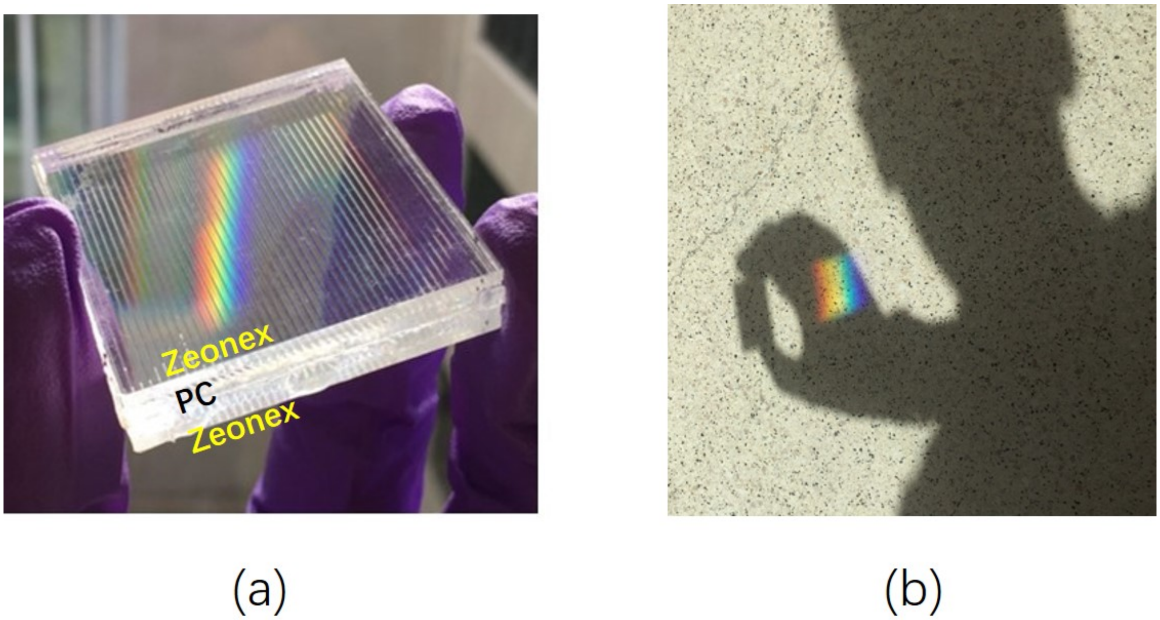

Figure 3-7: (a) The 4-prism spectrum splitting optics prototype; (b) Spectrum splitting effect of the prototype under sunlight.

showed surface roughness as 10 nm. The prism cross-section was exposed by die saw cutting, then examined using SEM and optical microscopy. The cross-sections are shown in Figure 3-8. The draft angle and the corner rounding are measured on the cross-section images using ImageJ. We have been able to achieve <2.5° draft angle and 20 µm corner rounding in the prototype prisms, respectively. The low-level prism imperfections contribute minimal loss in the current prototype spectrum splitting optics.

The bulk transmission of the 4-prism assembly prototype (w/o anti-reflection coating) was measured using UV-VIS with integrating sphere detector. 90% transmission is obtained between 400 nm and 1100 nm due to the thin optics profile, as shown in Figure 3-9.

We modeled optical transmission of the prism-lens assembly using ray-tracing under a light source with 0.25° semi-divergence angle source with AM1.5D spectrum from 280 nm to 1800 nm. In the model, a prism draft angle of 2.5° was used, consistent with our experimental measurement. A total of 3% Fresnel loss was assumed for the two optics-to-air interfaces combined, which can be readily obtained with state-of-the-

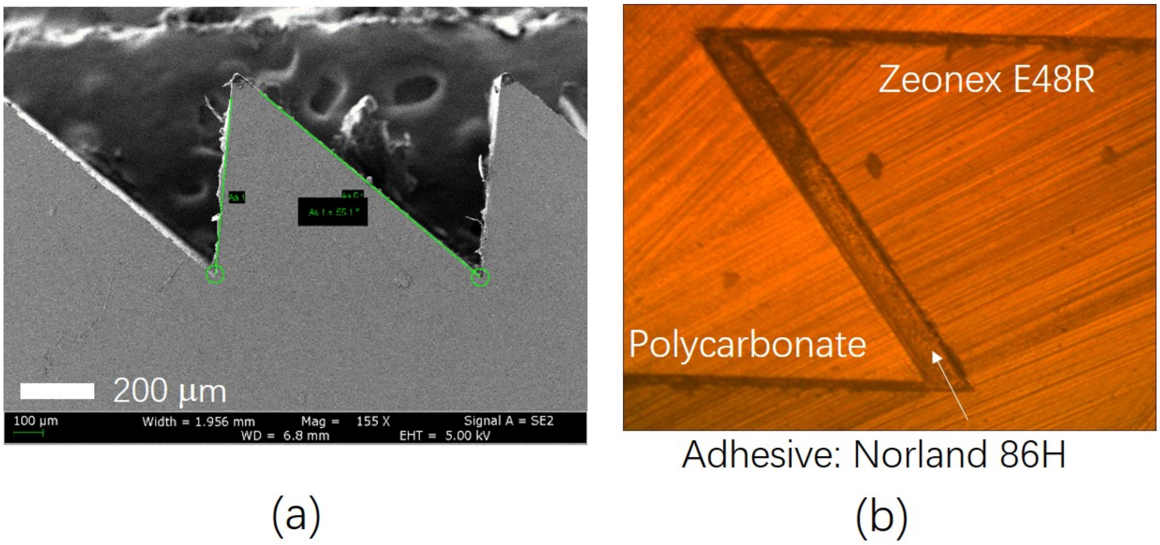

Figure 3-8: (a) SEM image of single prism cross-section; (b) Optical microscopy image of the 2-prism assembly cross-section.

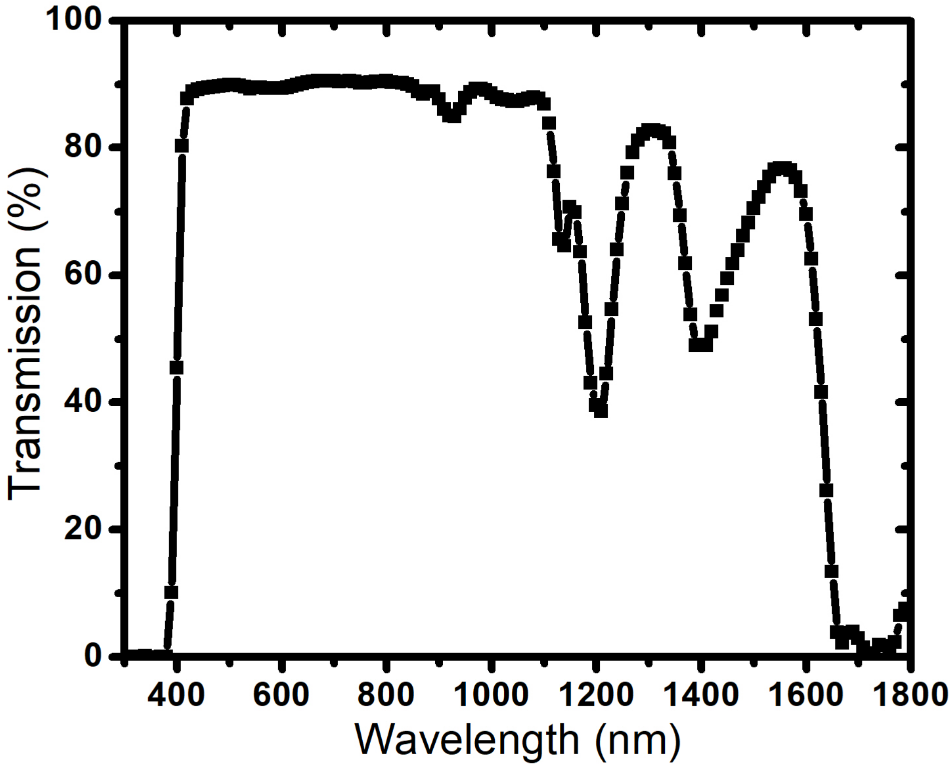

Figure 3-9: Bulk transmission of the 4-prism assembly measured using UV-VIS.

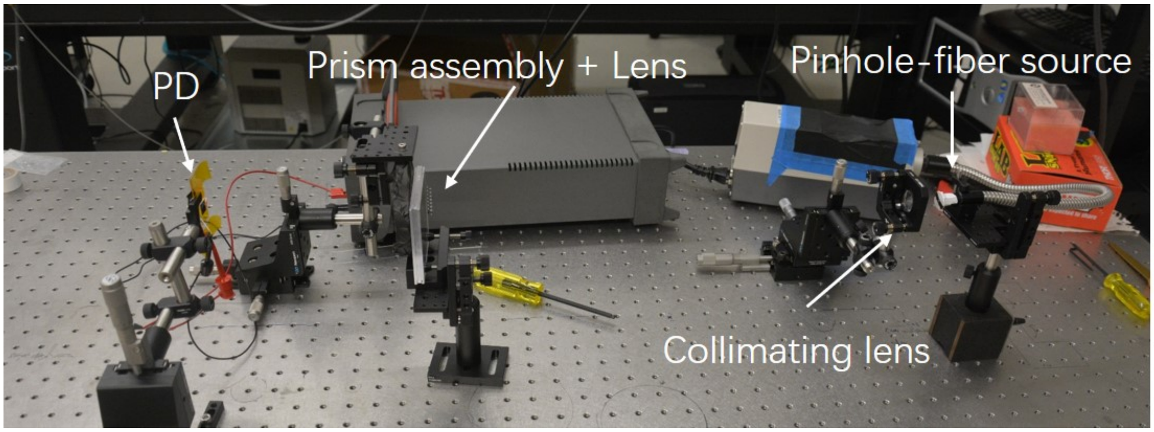

Figure 3-10: Focus transmission setup.

art anti-reflection coating.[83–85] The model indicates focus transmission of 78.7%. 7.8% loss comes from material absorption. In particular, the strong absorption of polycarbonate below 400 nm wavelength constitutes the main loss contributor. The remaining 10.5% loss is attributed to the shading loss.

To draw a direct comparison with the modeling results, focus transmission was measured using a self-constructed lab setup, as shown in Figure 3-10. The halogen lamp broadband fiber source was masked with a 10 µm pin-hole aperture. A collimating lens was used for beam collimation to approximately emulate the solar direct irradiance beam. The optical intensity was measured with a calibrated Si photodiode(Thorlabs, FDS1010). The focus transmission measured over the spectral range of 500 – 900 nm (limited by the light source and the Si photodiode) is 74.9%. In comparison, our model suggests focus transmission of 80.9% over the same wavelength regime. The 6.0% discrepancy is likely due to manufacturing and assembly imperfections. In addition, since the assembly is not anti-reflection coated, 7.6% loss results from Fresnel reflection at the two air-to-plastic surfaces. With state-of-the-art anti-reflection coatings, the prototype focus transmission and the simulated focus transmission will be improved to 80% and 86%, respectively.

To demonstrate the spectrum splitting capabilities and evaluate the discrepancy between the design and the prototype due to the material variation, fabrication control and environment sensitivity, the beam deflection angles were measured using

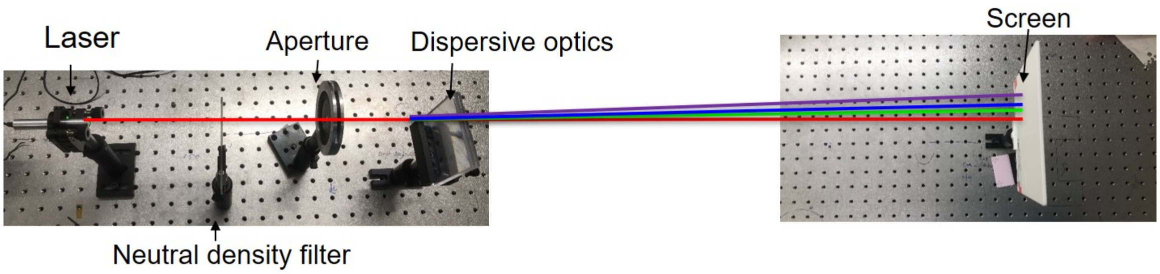

Figure 3-11: Beam deflection angle measurement setup.

Table 3.1: Measured and simulated deflection angles.

Wavelength [nm]	405	532	635	808	980
Experiment [degree]	7.48±0.33	5.71±0.19	5.17±0.19	4.74±0.13	4.36±0.24
Simulation [degree]	7.90	5.74	5.21	4.78	4.50

alignment laser at different wavelength. The setup is shown in Figure 3-11. The beam spot positions were recorded with and without the 4-prism stack and the deflection angles are inferred from the distance between the screen and the prisms. The measured angle values are compared with the simulated values in Table 3.1, showing excellent agreement. This indicates fine control in the optics manufacturing process and proves the robustness to apply it in large scale production. Notably, the bean deflection angle is below 8° at all wavelengths, which introduces minimal coma aberration for the focal spot.

The spectrum splitting performance was further demonstrated outdoor under clear sky conditions with the optical assembly mounted on a high precision 2-axis sun tracker (EKO STR-32G), as shown in Figure 3-12. The 4-prism assembly was mounted on an aspheric lens with a focal length of 150 mm and a 1 cm × 1 cm aperture. Focal plane images were captured using digital camera (Nikon, D7100) when band-pass filters (Thorlabs, FB440-10, FB510-10 and FB650-10) with center wavelengths of 440 nm, 510 nm, and 650 nm were applied in front of the aperture sequentially.

The ray-trace simulated focal spots are compared with the captured spots in Figure 3-13 (a) and (b), showing a good agreement. The focal spot intensity profiles

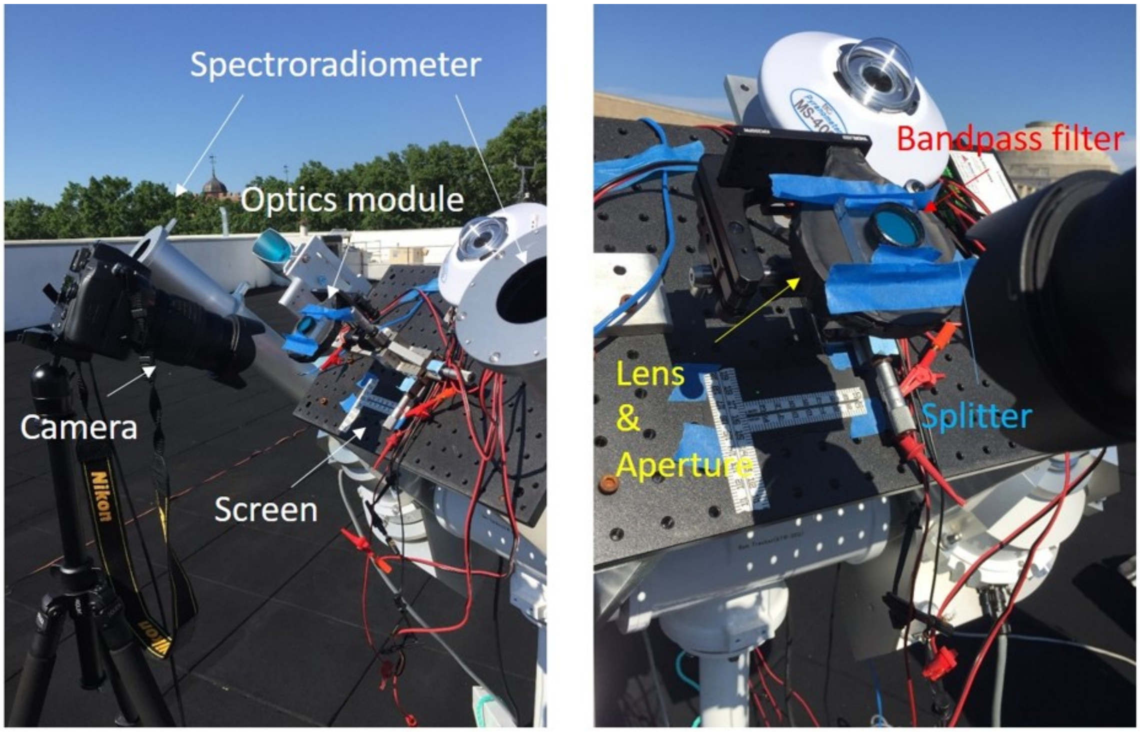

Figure 3-12: Outdoor spectrum splitting demonstration setup.

are analyzed quantitatively in directions along (labeled as X) and perpendicular to (labeled as Y) the spectrum splitting direction, and compared with simulation results, as shown in Figure 3-13 (c) and (d). The focal spots in the X directions show minimal overlaps, indicating excellent spectrum splitting capabilities of the prism assembly. The symmetric focal spot shapes in the X directions indicate that focal spot distortion due to spectrum splitting is minimal, an attractive feature for spectral matching onto lateral sub-cells. It also agrees to the measurement in Table 3.1.

3.3 Module Performance Simulation

The performance of a laterally arrayed module is projected based on the prism-lens array assembly. The module design concept is schematically depicted in Figure 3-14 (a). The 4-prism spectrum splitting stack is coupled with a lens array to allocate the photons on the dedicated lateral-arrayed multi-junction cells. Diffuse collection function can be embedded by laying Si cells on the backplane. As discussed in Chapter

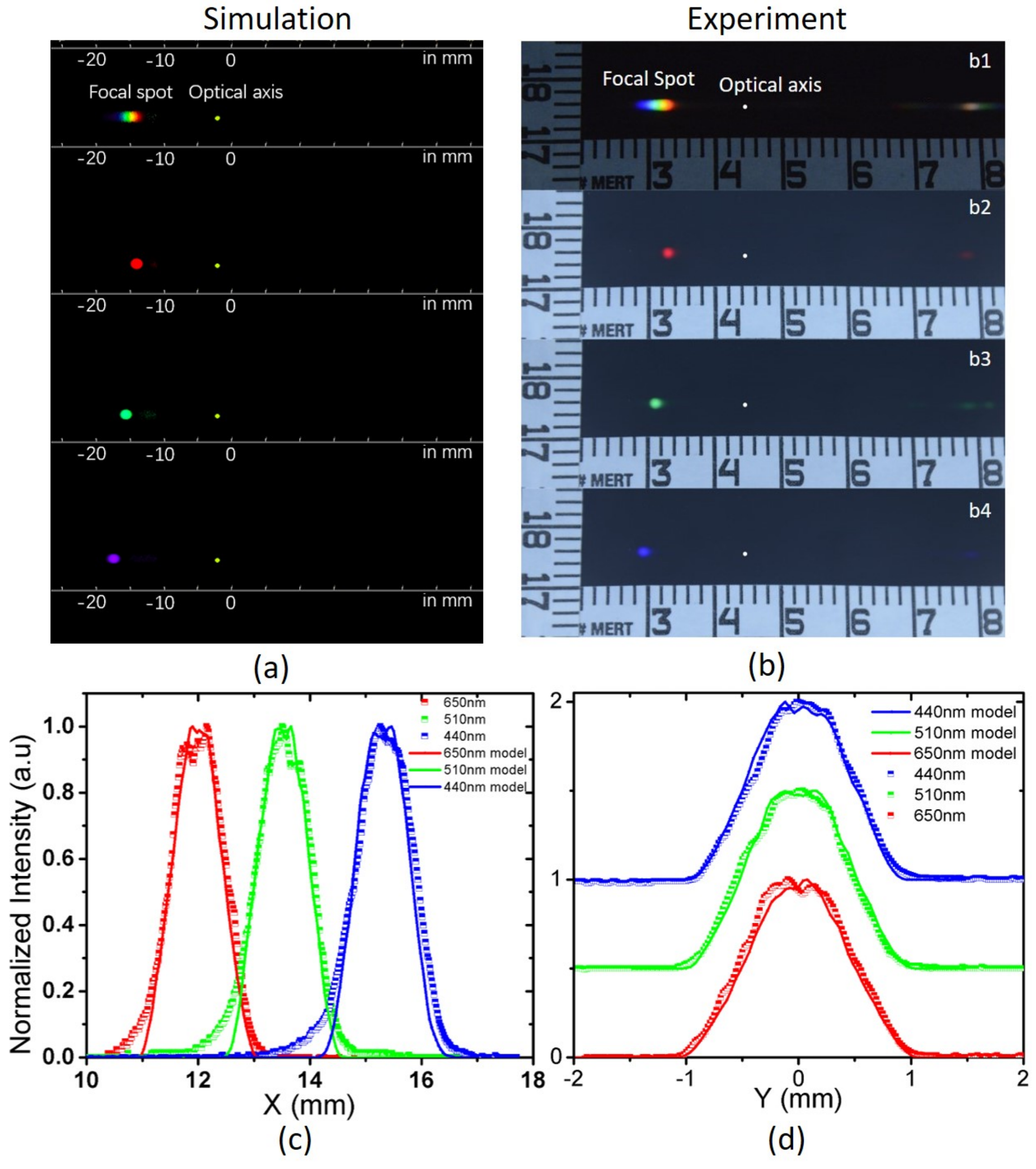

Figure 3-13: (a) and (b) Ray-trace simulated focal spots and captured spots with and without 650 nm, 510 nm and 440 nm bandpass filter; (c) and (d) Intensity profiles along and across spectrum splitting direction.

Table 3.2: Odd polynomial aspheric lens perimeters; Lens units in mm.

Curvature	1.0389
Conic constant	0.048018
2nd order coefficient	$2.3641*10^{-4}$
4th order coefficient	$-1.5018*10^{-5}$
6th order coefficient	$-1.0453*10^{-6}$
8th order coefficient	$8.6697*10^{-9}$
10th order coefficient	$2.5635*10^{-11}$
12th order coefficient	$1.5219*10^{-13}$

3.1.1, the multi-junction cells can operate at their own maximum power point at various conditions by deploying advanced electronic power management scheme.

Concentrating lens array is designed with ray-tracing model in the odd polynomial aspheric form. The lens perimeters are presented in Table 3.2. Lens material is chosen as Shott B270. Lens aperture is designed in a square shape as 1 cm × 1 cm. The focal length is about 4 cm. Figure 3-14 (b) shows the 3D schematics of the prism-lens-array assembly. The prism-lens-array assembly is tested on the 2-axis tracker and demonstrated excellent spectrum splitting in the on-sun test, as shown in Figure 3-14 (c).

The optimistic module performance is simulated with the spectrum splitting optics and the lens array assembly, using 3-J detailed balance model. [86] The optics transmission is 80.11% assuming zero draft angle. The cell positions, cell sizes and bandgaps are optimized using ray-tracing model and Matlab to maximize the overall conversion efficiency under standard AM1.5D spectrum from 280 nm to 1800 nm. The module performance is summarized in Table 3.3 and the incident spectral intensities of the three cells are plotted in Figure 3-15. The efficiencies to the AM1.5D irradiance (Eta) of the 3 cells are 14.85%, 17.92% and 11.67%, respectively. Thus, a module efficiency 44.43% is expected. To evaluate the spectrum splitting effect, an ideal spectrum splitting scenario is assumed and compared to the simulation model. In the ideal spectrum splitting case, the optics has the same transmission but the spectrum is splitted perfectly to the cell bandgaps. The cell bandgaps and sizes are

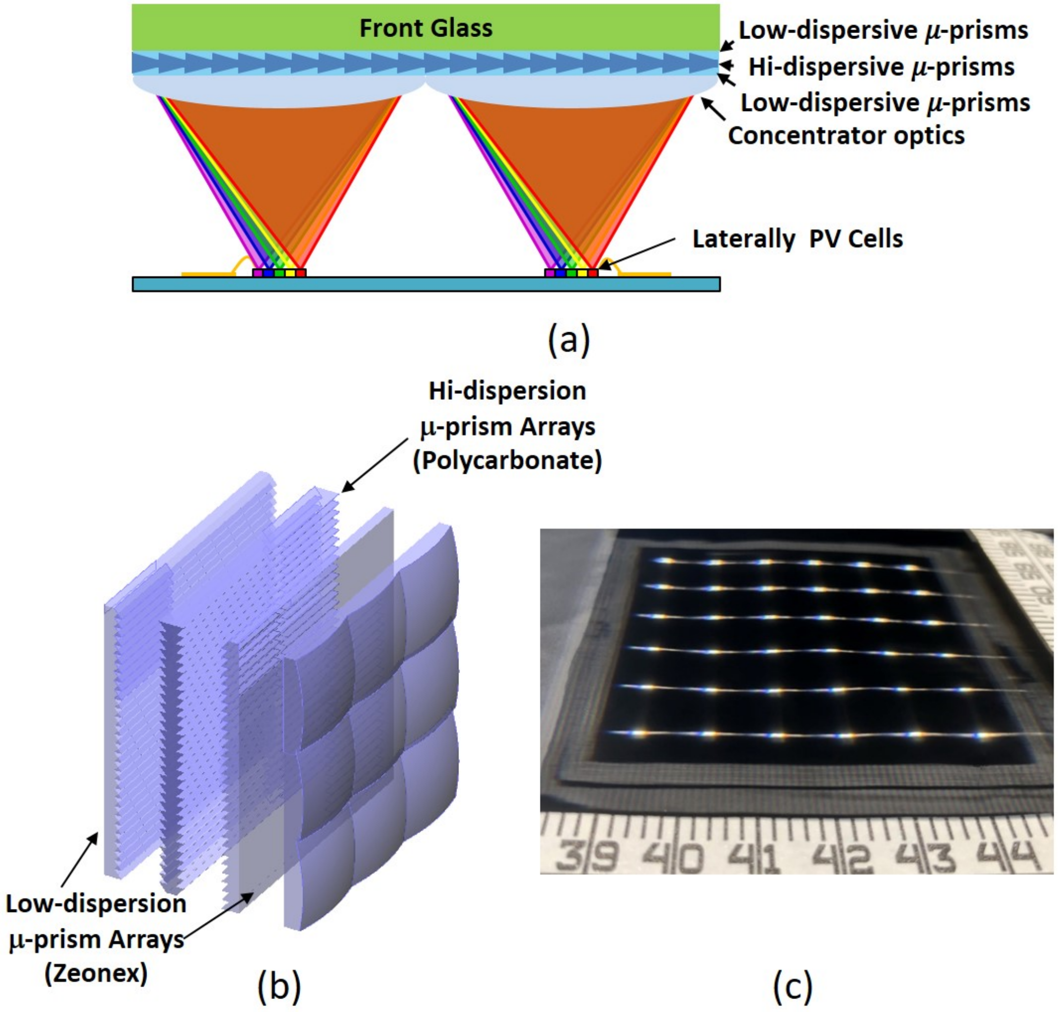

Figure 3-14: (a) Design concept schematics of lateral-arrayed multi-junction cell module; (b) 3D 4-prism stack and aspheric lens array assembly schematics; (c) On-sun spectrum splitting effects of the prism-lens-array assembly.(Units on ruler are in cm.)

Table 3.3: Detailed balance model module performance summary.

Bandgap [eV]	Possible cell material	Cell length [mm]	Geometric concentration ratio	Voc [V]	Isc [mA]	FF [%]	Eta [%]
2.033	InGaP	1.97	50.8X	1.816	7.59	92.65	14.85
1.390	InGaAs	0.43	232.6X	1.247	13.72	90.11	17.92
0.766	InGaAs	0.39	256.4X	0.663	18.03	84.02	11.67

kept the same. By normalizing the module efficiency to perfect splitting case, only the spectrum spitting capability is evaluated without interference from other factors. It shall be noted that such ideality is unachievable in reality due to the solar beam divergence and optics aberration, which leads to spots overlapping. The perfect module efficiency is 50.66% and the spectrum intensities in the perfect splitting case are also plotted as shaded areas in Figure 3-15. By normalizing the module efficiency, this spectrum splitting optics can achieve 87.7% performance compared to the perfect spectrum splitting case.

A realistic module performance is also simulated by using the model perimeters in reference [55]. This model assumes: (a) Using cell materials as InGaP, GaAs and Ge. These materials can grow on Ge substrate to reduce the module assembly cost; (b) The model's photon absorption is based on material absorption coefficient and optimized anti-reflection coatings instead of blackbody perfect absorption; (c) The cells model is using two-diode model based on measured cell material properties instead of thermodynamic limit assumptions in detailed balance model; (d) The cells have shading loss as 6% due to the metallization on the cell surface. The original model assumed perfect spectrum splitting and 100% optical transmission. We updated with our realistic optics performance via ray-tracing model and optimized the cell sizes and positions to maximize the overall module efficiency. The simulation results and the related incident spectral intensities are shown in Table 3.4 and Figure 3-16, respectively. The realistic module can achieve 29.00% module efficiency. Compared to the perfect spectrum splitting module efficiency as 32.88%, the spectrum splitting optics can achieve 88.2% of the ideal performance.

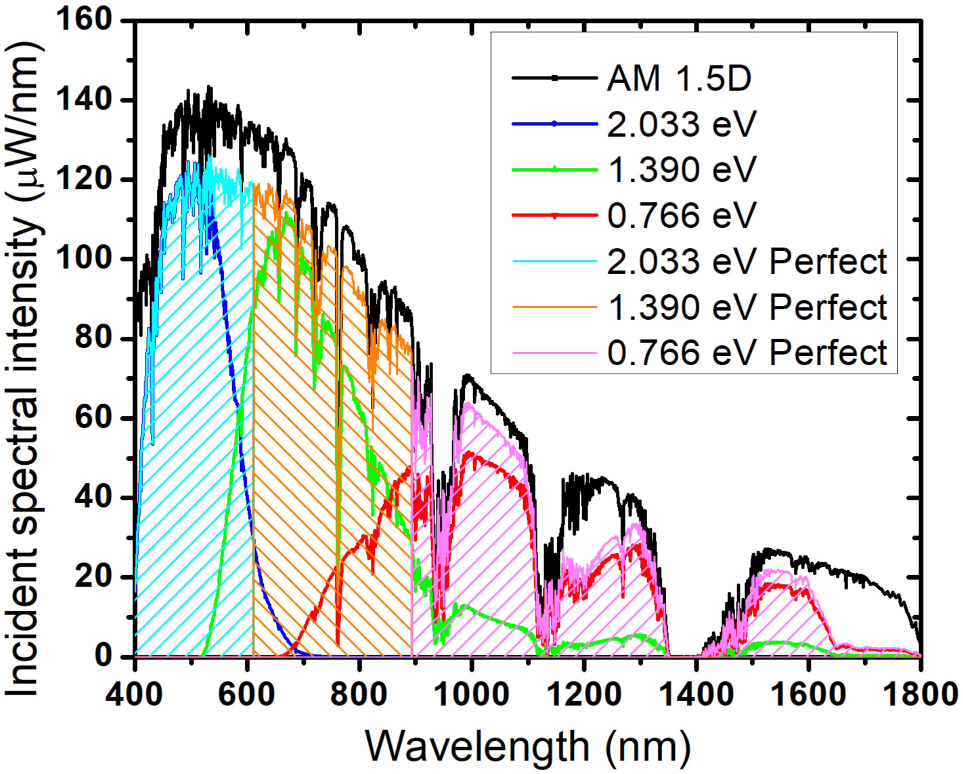

Figure 3-15: The incident spectral intensities of the 3-J cells in detailed balance model.

Table 3.4: Realistic model module performance summary.

Bandgap [eV]	Cell material	Cell length [mm]	Geometric concentration ratio	Voc [V]	Isc [mA]	FF [%]	Eta [%]
1.8849	InGaP	1.98	50.5X	1.508	9.01	90.72	14.32
1.4234	GaAs	0.42	238.1X	1.047	12.04	85.51	12.53
0.6642	Ge	0.34	294.1X	0.324	8.65	66.11	2.15

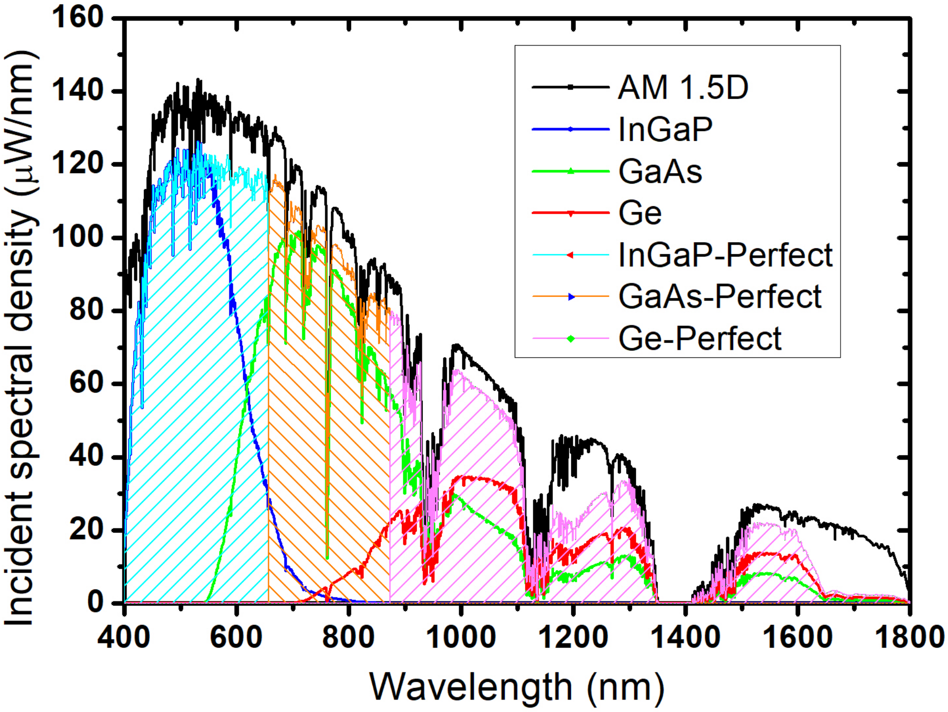

Figure 3-16: The incident spectral intensities of the 3-J cells in realistic model.

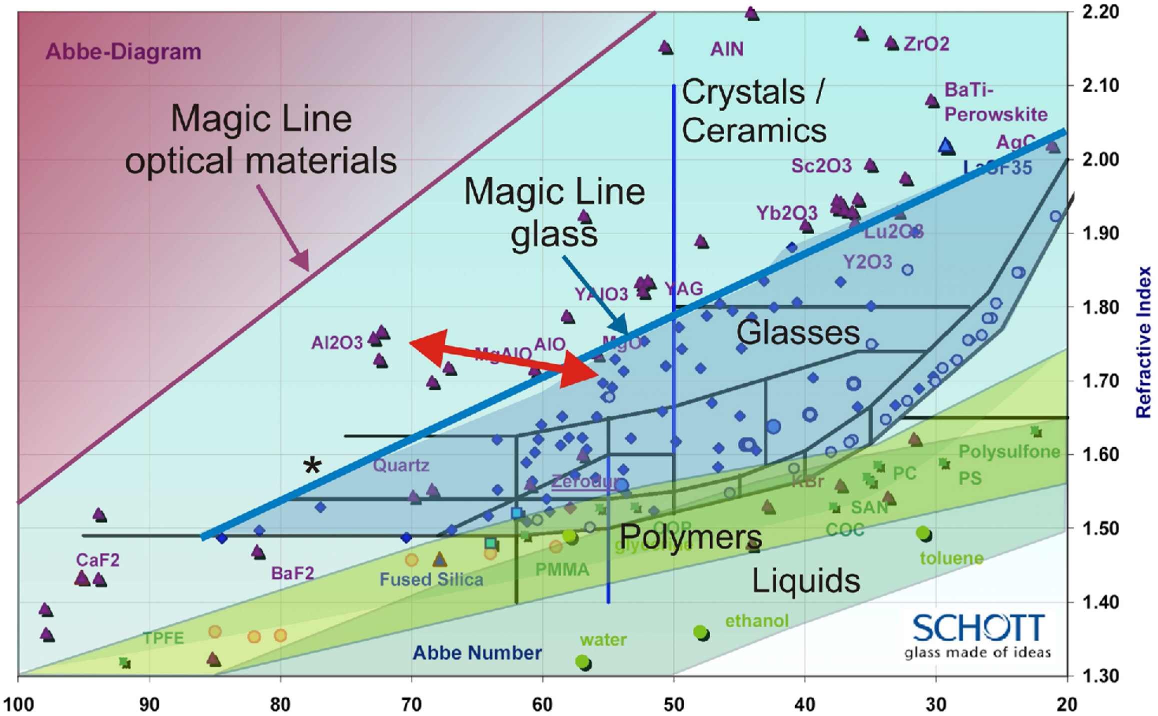

Figure 3-17: Abbe number vs refractive index diagram.

There are a few considerations to improve the multi-junction cells module efficiency: (a) Reducing material absorption. According to the ray-tracing model, the 4-prism spectrum splitting optics transmission can be improved from 80.11% to 87.63% if the material absorption is zero. There are two methods to reduce the material absorption. One is to replace the plastic material, especially polycarbonate, to optical glass. Optical glass usually has lower extinction coefficient, especially in the near UV region. However, according to the Abbe number refractive index diagram in Figure 3-17, [87] to achieve the same Abbe number contrast, unusual glass must be deployed which will significantly increase module cost. Besides, glass prism optics will face more severe corner rounding issues. [82] Another approach is to reduce the prism height h. This approach requires finer control in the molding process. Currently, commercially available compression molding prism arrays can deliver 100 µm high prism arrays. Ray-trace simulation indicates reducing h from 0.9 mm to 100 µm can increase the 4-prism stack focus transmission from 80.11% to 82.92%. Further improvement requires development of advanced molding process.

(b) Reducing spots overlap. The current optics assembly can achieve 88% performance to the perfect spectrum splitting case. The left 12% percent is due to the mis-allocated photons, especially at the cell bandgaps, as shown in Figure 3-15 and 3-16. The spectrum splitting optics can be further improved by optimizing the prism perimeters, choosing novel materials and stacking more prism layers, as discussed in Chapter 3.2.1. The concentrating optics abberation is another source of spots overlap, which can be improved by refining the lens profile. It shall be noted that increasing focal length is beneficial to reduce spherical abberation. However, in diffraction limited scenario, it's not effective. This is because the spots overlap fundamentally originates from the solar beam divergence. If define the focal length, solar beam divergence angle and split angle as f, θ_b and θ_s, respectively. The spot size and the spot center distance can be approximated as $f\theta_b$ and $f\theta_s$. [88] Thus, the spot overlap is approximately θ_b/θ_s, which is an invariant of f. Besides, increasing focal length will reduce the concentration ratio, as a trade-off.

3.4 Conclusion

In this chapter, we discussed the potential of lateral structure in multi-junction cells efficiency improvement and the previous spectrum splitting optics designs. We analyze and demonstrate micro-prism-array based spectrum splitting optics, tailored for high-efficiency, ultra-compact micro-CPV modules integrated with laterally-positioned multi-junction cells. The planar dispersive optics can deliver 80% optical transmission under standard AM1.5D spectrum. The conjugate design introduces minimal beam deflection, thus minimal off-axis aberrations desirable for precise spectral matching. Such an approach further ensures cost-effective, large-area fabrication of optical components as well as compatibility with scalable micro-CPV module assembly such as high throughput transfer-printing.

Chapter 4

Annualized Diffuse Radiance Energy Distribution Simulation

4.1 Introduction

As discussed in Chapter 1.3, hybrid CPV concept can significantly increase the module energy yield and expand its geographic applications. To further reduce the module cost, concentrating the diffuse solar irradiance is a viable route to minimize the Si material usage. It's especially attractive for micro hybrid CPV module since the diffuse concentrator can be monolithically molded with the DNI concentrator, thus introduces minimal extra cost. According to the Equation 1.10, an accurate description of the radiance angular distribution is the key start point for diffuse concentration design.

Several attempts have been demonstrated to simulate the diffuse irradiance for energy harvesting purpose. NREL PVWatts is widely used for panel PV module performance estimation based on a modified constant approach and it takes account the effect of panel tilt, orientation and urban temperature. [89] Reinhart's group novelly

---

Work presented in this chapter has been published in:
"Annualized Solar Diffuse Radiance Energy Distribution Simulation for Concentrator Design", 2019 IEEE 45th Photovoltaic Specialists Conference, (2019).

combined large GIS datasets and LiDAR elevation measurement to generate an annual solar radiation calculation engine called DAYSIM which demonstrated improved geometric accuracy and irradiation predictions for panel PV installation. [90] Lubitz generated a simulation approach based on meteorological year data to optimize the tilt angle and maintenance process for panel PV. [91] However, these approaches cannot be direct applied for diffuse concentrator design since they only provide irradiance values while concentrator design required radiance distribution information. The previous diffuse concentrator studies are commonly using the simplest isotropic sky model, which assumes the diffuse radiation is uniformly distributed over the sky dome. [92–94] However, it significantly underestimates the forward scattering nature of diffuse irradiance and thus underestimates the collectible diffuse energy of CPC. [95] An improved approach is developed by the International Commission on Illumination (CIE). [96] It adopted an classification method to simplify the problem and generated 15 standard sky types to describe the weathers that include cloudless, partly cloudy and overcast. Each sky type has its own specific luminance pattern to calculate the radiance distribution. It provides a useful reference for concentrator design in standard conditions. [97–99] However, these standard skies are not suitable to predict the solar irradiance in the outfield since the PV performance can deviate >30% monthly from the standard conditions due to the variation in real conditions. [100]

In this work, we claim that a solid approach shall exhibit the following features: (a) The simulation approach shall use a radiance distribution model: Illuminance model places little weight on photons with wavelength <450 nm or >650 nm, thus introducing unnecessary system errors. (b) The model shall provide angular distribution description for optics engineers to maximize the geometric concentration while collect most of the diffuse energy. (c) The modelling approach shall present a statistical average of yearly diffuse radiance energy distribution: solar farm will serve over 15-years lifetime. The data is only meaningful if it accounts representative meteorological factors like geographic locations and weather conditions. [101]

Thus, we propose to implement the Igawa all-weather anisotropic diffuse radiance model with National Solar Radiation Data Base (NSRDB) third-generation Typical

Meteorological Year (TMY3) Datasets to generate the annualized diffuse radiance energy distribution map for diffuse concentration design and evaluation.

Igawa model is based on 1-year measurement taken in two cities in Japan, Tokyo and Fukuoka. [102] It adopts the main form from the CIE model, using graduation function and scattering indicatrix function to describe the diffuse radiance distribution. The irradiance data used were measured with a sky scanner of full-acceptance angle as 11°. The lowest altitude of the sky elements for sky radiance is 6° to account the surrounding building shading effect. And the sky elements of which angular distance to the sun are smaller than 15° are excluded in the regression analysis due to the strong circumsolar effect. There are also other anisotropic diffuse models like Perez 1993, Brunger 1993, Harrison 1991 and Kittler 1985. [103–106] We found that Igawa model demonstrated better performance in a few model comparison studies, making it the preferred choice for our study. [102, 107, 108]

TMY3 datasets contain representative hourly data of solar radiation and meteorological information for one-year period. It contains 1020 weather stations that covers the whole United States area, thus providing a nation-wide comprehensive description as shown in Figure 4-1. [109] It shall be noted that TMY3 datasets are based on dated measured data and simulations which may failed to account the changes of solar radiation resources due to causes like pollution. Consistently updated data from NSRDB can be used if model timeliness is a concern.

By combining the two tools, we are able to generate representative annualized diffuse radiance energy distribution maps that account geographic locations and weather conditions and provide high accuracy reference for efficient energy-production-oriented concentrator designs.

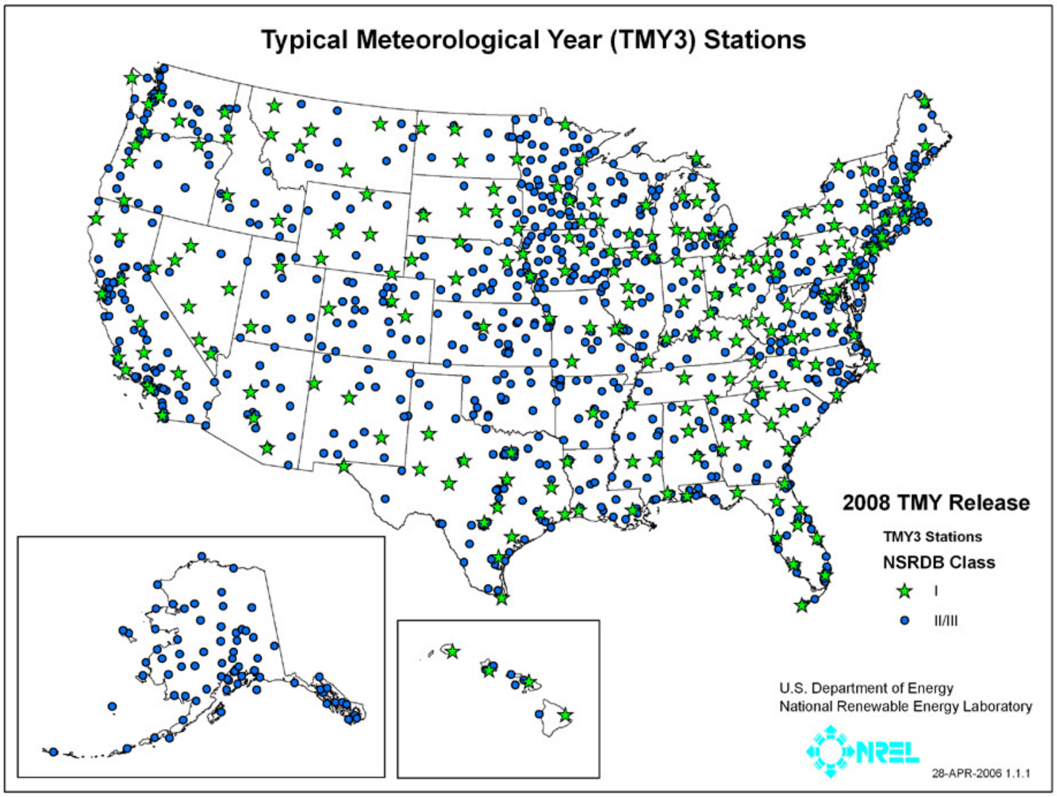

Figure 4-1: TMY3 stations distribution in USA.

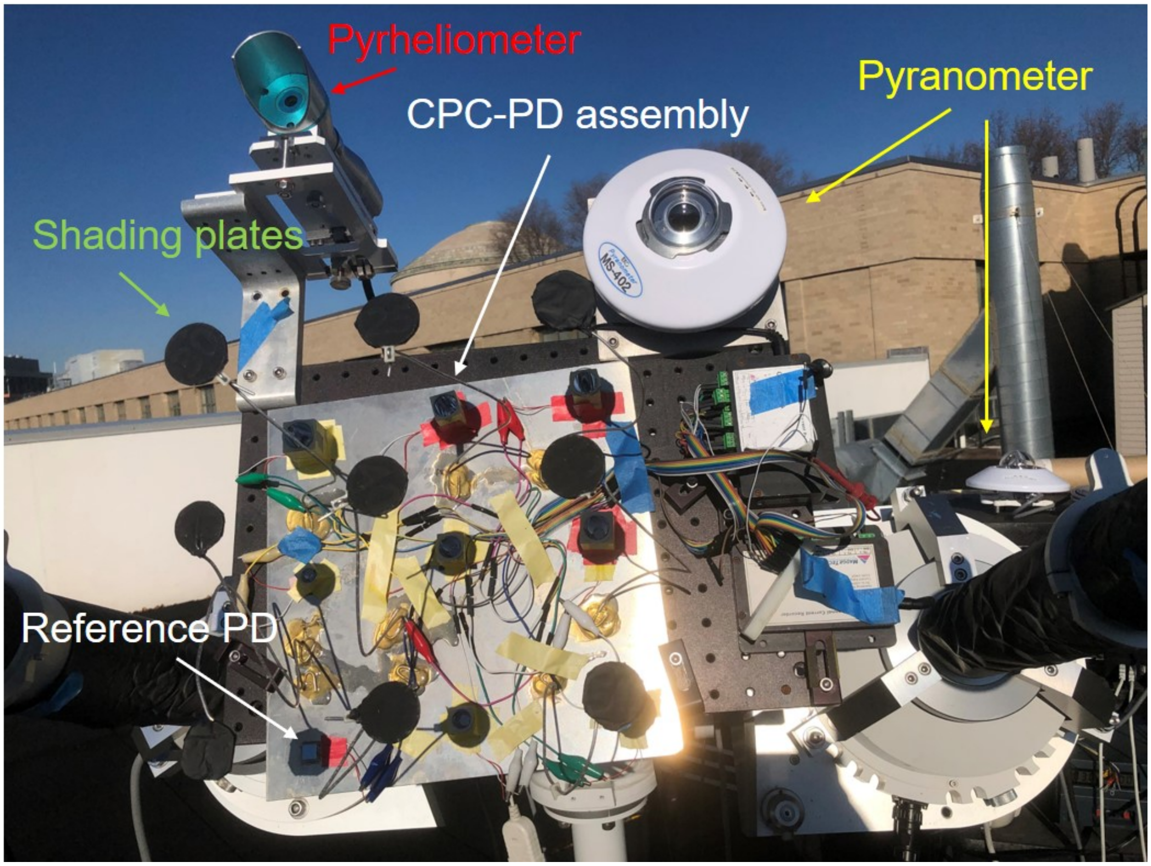

Figure 4-2: Setup of the CPC measurement.

4.2 Diffuse Angular Distribution Measurement: Validating the Model

To test the validity of the Igawa model, compound parabolic concentrators (CPCs) are customized with semi-acceptance angle ranging from 20° to 55°. The CPCs are assembled with Si photodiodes (PD) (Thorlabs, FSDS1010) using optical adhesive (Norland 86H). The CPC-PD assemblies and a bare reference PD are mounted on a 2-axis tracker (EKO, STR-32G) and aligned to the sun position during tracking. The semi-acceptance angle of reference PD is taken as 90°. Shading plates are applied to block DNI light so only the diffuse light is collected. By normalizing the signals of CPC-PD to the reference PD, the CPC transmission within certain incident angle is measured. DNI and GHI are measured with pyrheliometer (EKO, MS-56) and pyranometer (EKO, MS-802), respectively. The setup is shown in Figure 4-2.

The simulated CPC transmission T_{CPC} is shown as Equation 4.1:

$$T_{CPC} = \frac{\int\limits_{\gamma=0}^{\pi/2}\int\limits_{\alpha=0}^{2\pi} \cos\gamma \cdot \cos\zeta \cdot Le(\gamma_s, \gamma, \zeta) \cdot T^{*}_{CPC}(\zeta) \cdot d\gamma d\alpha}{\int\limits_{\gamma=0}^{\pi/2}\int\limits_{\alpha=0}^{2\pi} \cos\gamma \cdot \cos\zeta \cdot Le(\gamma_s, \gamma, \zeta) \cdot d\gamma d\alpha} \tag{4.1}$$

$T^{*}_{CPC}(\zeta)$ is the transmission of CPC to rays with incident angle ζ, which is studied with LightTools ray-tracing software with responsivity-corrected ASTM G173-03 diffuse spectrum. The ASTM G173-03 diffuse spectrum is derived by the difference between the ASTM G173-03 global tilt spectrum and the ASTM G173-03 direct + circumsolar spectrum. Then the spectrum is corrected with the photodiode (PD) wavelength responsitivity curve. The other labels are introduced in details in the next Chapter 4.3.

The measurement is performed under various weather types (e.g. clear, partly cloudy, overcast) for 152 days from August 2018 to July 2019, in Cambridge MA, USA. The measurement-suspended days are due to weather issues (The setup is not waterproof to measure in rainy or snowy days) and setup maintenance. The measurement and the simulation results are presented in Figure 4-3. It should be noted that Igawa model underestimates the forward scattering feature of diffuse light when sky index is between 0.3-0.9, as the results of exclusion of sky elements of which angular distance to the sun are smaller than 15°. It leads to the deviation between measurement and simulation in the corresponding conditions. Except this minor imperfection, there is generally good agreement between the measurement and the simulation which supports Igawa model's applicability for our simulation purpose.

4.3 Model Construction

The Igawa model radiance distribution function $Le(\gamma_s, \gamma, \zeta)$ is determined by the graduation function $\phi(\gamma)$ and the scattering indicatrix function $f(\zeta)$ in the form as Equation 4.2:

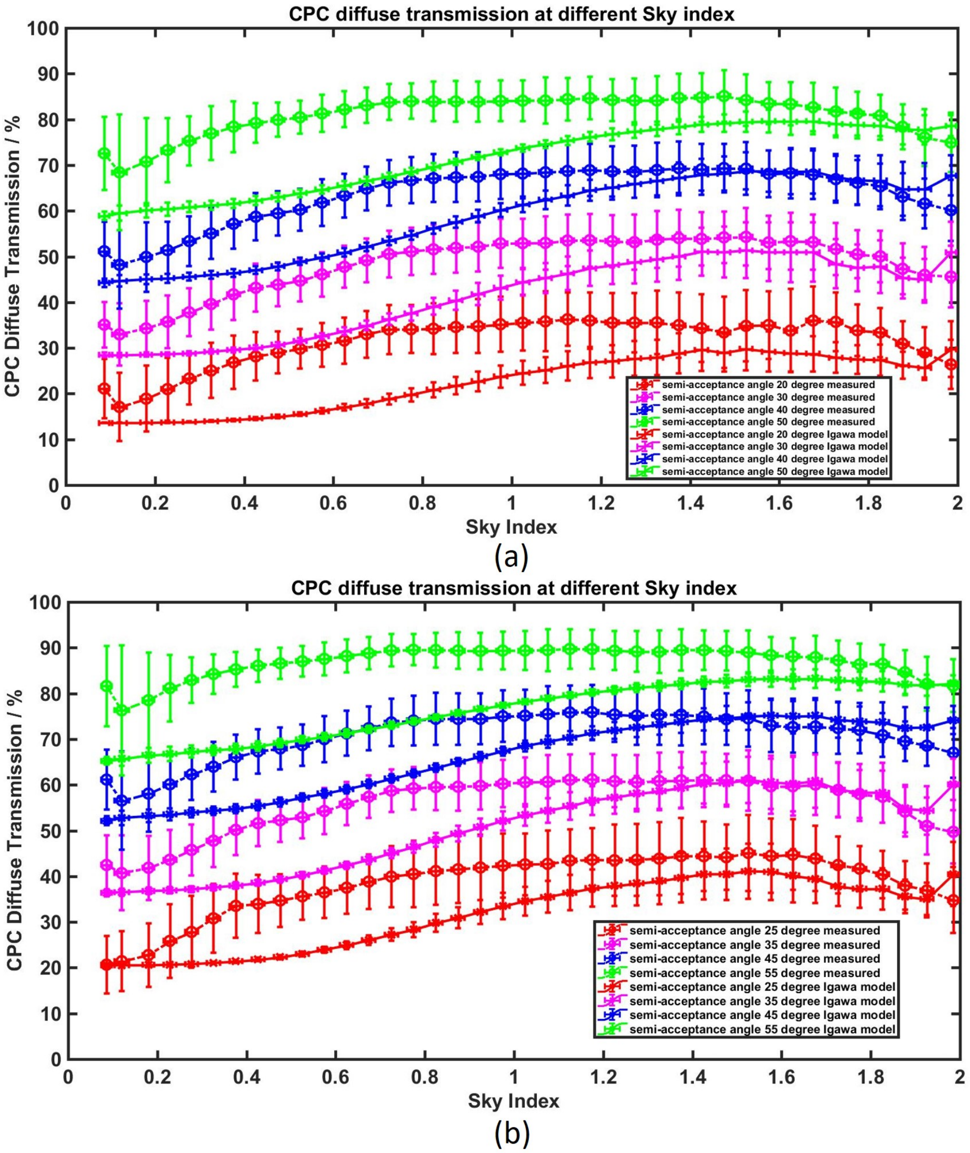

Figure 4-3: Diffuse irradiance transmission at different sky index. (a) CPC acceptance angle: 20°, 30°, 40° and 50°; (b) CPC acceptance angle: 25°, 35°, 45° and 55°. Measured data labelled with circles. Simulation data labelled with squares.

$$Le(\gamma_s, \gamma, \zeta) = Lez(\gamma_s) \cdot \frac{\phi(\gamma) \cdot f(\zeta)}{\phi(\pi/2) \cdot f(\pi/2 - \gamma_s)} \tag{4.2}$$

where $Lez(\gamma_s)$, γ, γ_s, ζ are zenith radiance, altitude angle of the sky element, sun altitude angle and the absolute angular difference from the sky element to the sun position, respectively. The graduation function $\phi(\gamma)$ and the scattering indicatrix function $f(\zeta)$ are described in Equation 4.3 and 4.4 as:

$$\phi(\gamma) = 1 + a \cdot \exp(b/\sin\gamma) \tag{4.3}$$

$$f(\zeta) = 1 + c \cdot (\exp(d \cdot \zeta) - \exp(d \cdot \pi/2)) + e \cdot \cos^2\zeta \tag{4.4}$$

The coefficients *a*-*e* are functions of defined term sky index. Sky index is highly correlated with the sky clearness. It's determined by diffuse horizontal irradiance (DHI), global horizontal irradiance (GHI), and sun position with other constants such as extraterrestrial direct normal irradiance.

Equation 4.2 only gives relative value of $Le(\gamma_s, \gamma, \zeta)$. The absolute value of $Le(\gamma_s, \gamma, \zeta)$ is derived from expression of DHI as Equation 4.5:

$$\text{DHI} = \int_{\gamma=0}^{\pi/2} \int_{\alpha=0}^{2\pi} Le(\gamma_s, \gamma, \zeta) \cdot \sin\gamma \cdot \cos\gamma \cdot d\gamma d\alpha \tag{4.5}$$

γ is the azimuth angle of the sky element.

Thus, the radiance distribution $Le(\gamma_s, \gamma, \zeta)$ is a function of DHI, GHI and sun position. DHI and GHI can be directly retrieved from TMY3 hourly datasets. Sun position is calculated with PVLIB toolbox in Matlab using time, geographic locations and weather data from the TMY3 datasets. [110] Then the annualized diffuse radiance energy distribution map can be generated by adding the hourly radiance distribution $Le(\gamma_s, \gamma, \zeta)$. $Le(\gamma_s, \gamma, \zeta)$ needs to take into account the tracking method: for 2-axis tracking systems, $Le(\gamma_s, \gamma, \zeta)$ shall be transformed to align to the sun position. For 1-axis tracking systems, $Le(\gamma_s, \gamma, \zeta)$ shall be transformed to align to the azimuth tracking direction.

It shall be noted that the radiance model does not have spectral feature while Rayleigh scattering indicates wavelength dependence in scattering. Albedo is assumed zero because no albedo angular distribution model exists, and it needs to consider complicated surrounding building environments. However, this approach shall be an accurate-enough first order simulation for design start point. To maintain the same assumptions with the original Igawa model, our simulation assumes zero radiance value from sky elements with altitude angle $<5°$. Sky elements of which the angular distance to the sun position is $<2.5°$ also have zero radiance value to exclude the direct and circumsolar irradiance. The annualized diffuse radiance energy distribution maps of the 221 TMY3 class 1 stations are generated by Matlab code as detailed above, attached in Appendix A.

4.4 Insights from the Model

As a comparison, annualized diffuse radiance energy distribution maps of Boston in 2-axis tracking scheme based on Igawa model and isotropic model are shown in Figure 4-4. These maps are formed in altitude-azimuth format, with typical geographical convention of south = 180° azimuth. The concentric circles represent the altitude from 0° to 90°, with sun position = 90°. In 2-axis scheme, the diffuse radiance energy distribution drops sharply in the south direction because current model assumes zero albedo. The maps show that the isotropic model significantly underestimates the forward scattering nature of diffuse irradiance.

Ideal anisotropic CPCs are simulated as exemplary diffuse concentrator design based on these maps. Ideal CPC is assumed to have 100% and 0% transmission to rays incident within and outside the acceptance angle region, respectively. In 2-axis scheme, the CPC is always aligned to the sun. The optimization perimeters are the semi-acceptance angles in the horizontal and vertical directions. Figure 4-5 (a) and (b) showed the simulated collectible diffuse energy with Igawa model and isotropic model. It shows that the Igawa model predicts $> 50\%$ collectible energy compared to

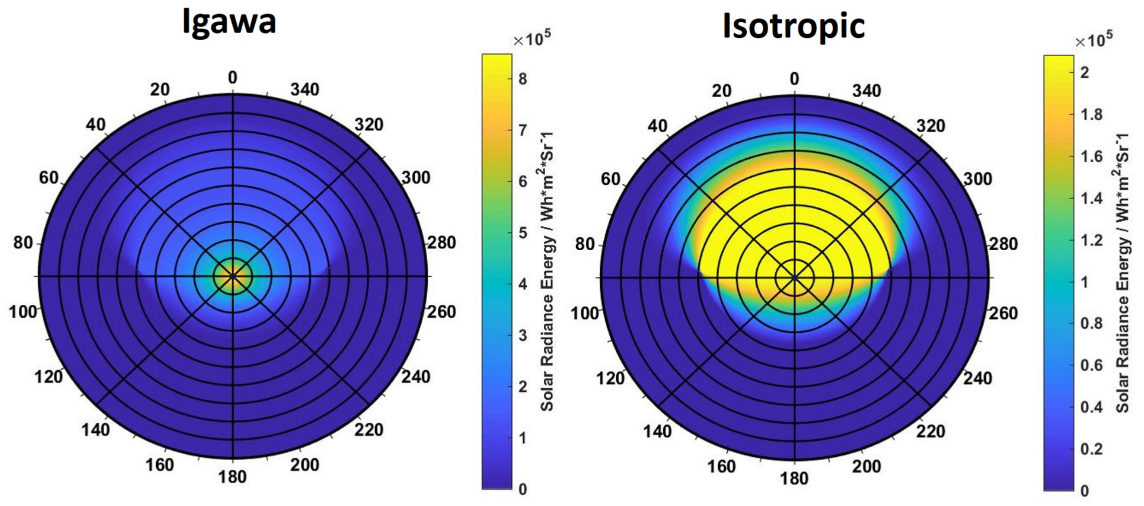

(a) (b)

Figure 4-4: Annualized diffuse radiance energy distribution map of Boston in 2-axis tracking scheme. (a) using Igawa model, (b) using isotropic model.

the isotropic model, indicating the importance to deploy the right model to accurately describe the diffuse radiance distribution. Figure 4-5 (c) shows the diffuse energy collection efficiency of the CPC, by normalizing the collectible diffuse energy to the case with 90° vertical acceptance angle and 90° horizontal acceptance angle. 80% diffuse energy can be collected with 50° acceptance angle CPC. To study how much diffuse cell area can be reduced by applying concentration, the line concentration ratio is calculated as $Concentration\, ratio = n/sin(acceptance\, angle)$, assuming refractive index $n = 1.5$. Figure 4-5 (d) shows that 5X dielectric diffuse concentrator can collect 80% of the total diffuse energy in 2-axis tracking scheme. It suggests that 80% diffuse cell area can be reduced with only 20% loss in the diffuse energy collection by applying diffuse concentrator.

The annualized diffuse radiance energy distribution maps are imported into the ray-tracing model to design a realistic diffuse concentrator in the module described in Chapter 3.3 to enable a hybrid module function, as shown in Figure 4-6. The LightTools model schematics is shown in Figure 4-7 (a). The diffuse concentrator is designed as an anisotropic polygon CPC to match with the 1 cm × 1 cm aperture. The diffuse concentrator input aperture is fixed as 9.5 mm × 9.5 mm so the diffuse

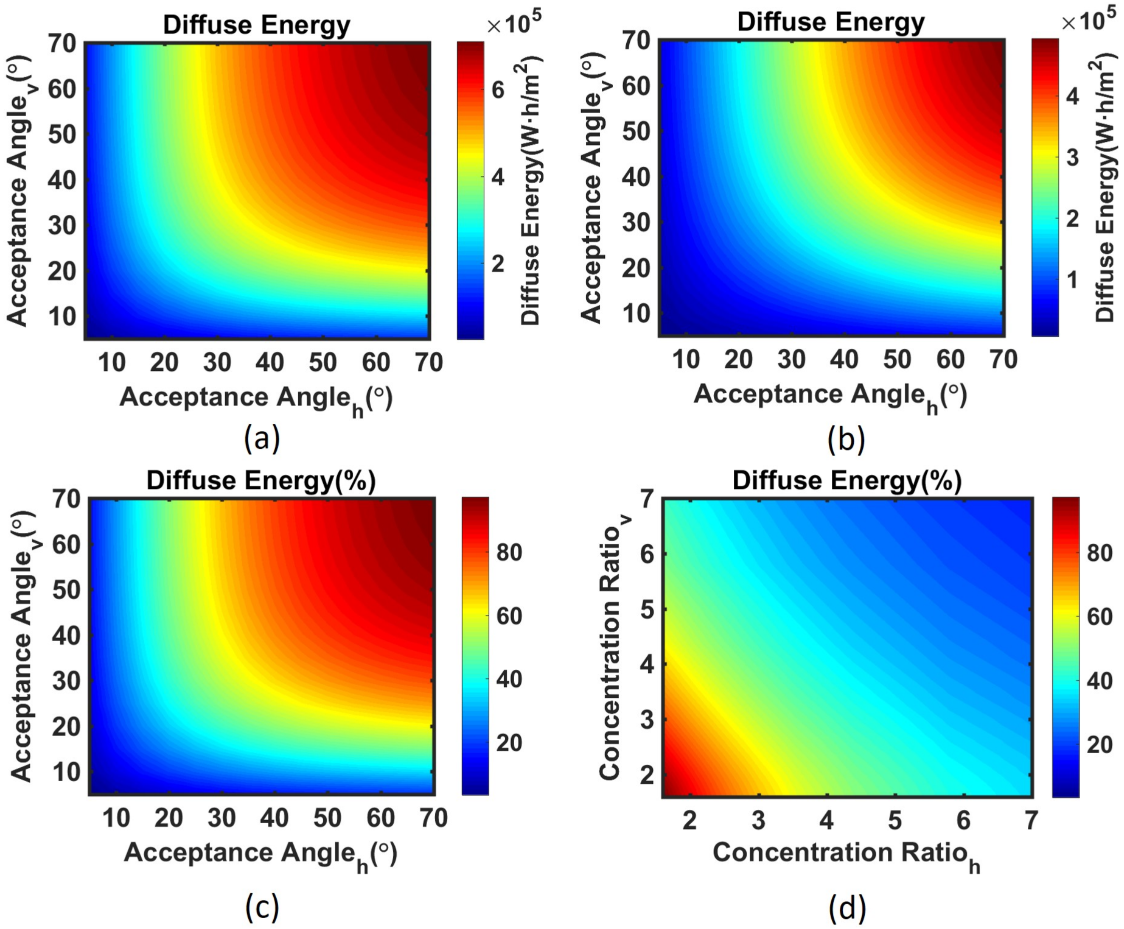

(a) (b)

(c) (d)

Figure 4-5: (a) Collectible diffuse energy at different acceptance angle with Igawa model; (b) Collectible diffuse energy at different acceptance angle with isotropic model; (c) Diffuse energy collection efficiency at different acceptance angle with Igawa model; (d) Diffuse energy collection efficiency at different concentration ratio with Igawa model.

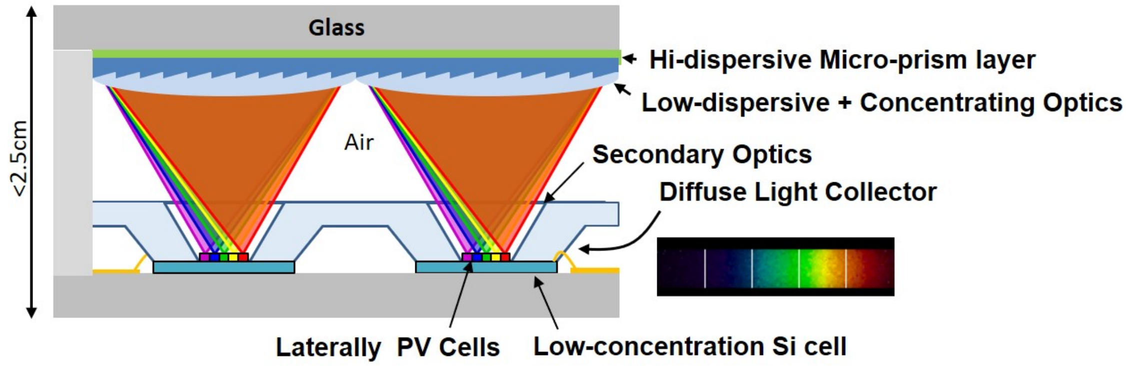

Figure 4-6: Schematics of the micro hybrid laterally-arrayed multi-junction cells module.

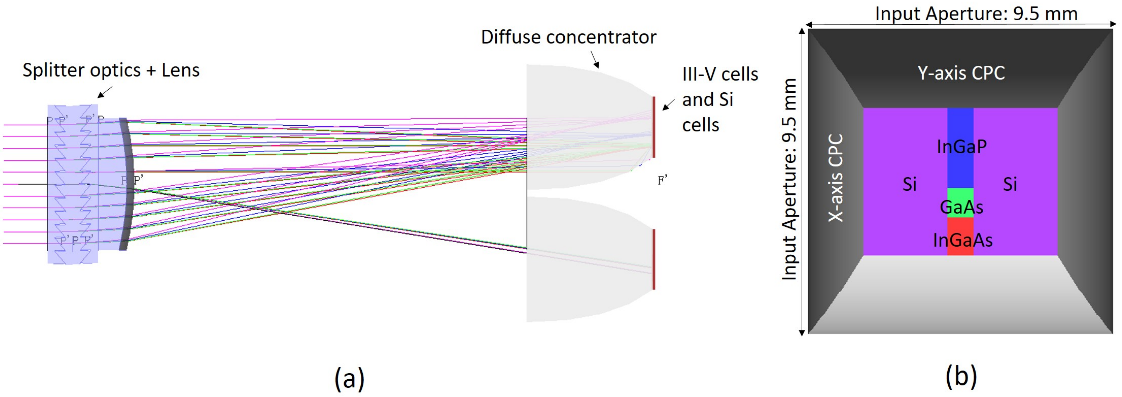

Figure 4-7: (a) Ray-trace model schematics of the module; (b) The layout of the cells and the diffuse concentrator.

concentrator array will have 1 mm wall thickness to ensure mechanical strength. The reflective diffuse concentrator is made of reflective aluminum which has reflectivity as 91.2%. The output aperture size in the Y direction (the spectrum splitting direction) matches to the total length of the III-V multi-junction cells and the output aperture size in the X direction (across the spectrum splitting direction) can be optimized. Two Si cell are put side-by-side with the III-V cells as diffuse cells at the CPC output, as shown in Figure 4-7 (b). The diffuse collection efficiency of this CPC design is plotted in Figure 4-8, showing that the Igawa model consistently predicts >10% more collectible diffuse energy.

To study the diffuse irradiance resources variation across the United States, Figure 4-9 shows the annualized diffuse radiance energy maps of Boston (MA), Seattle (WA),

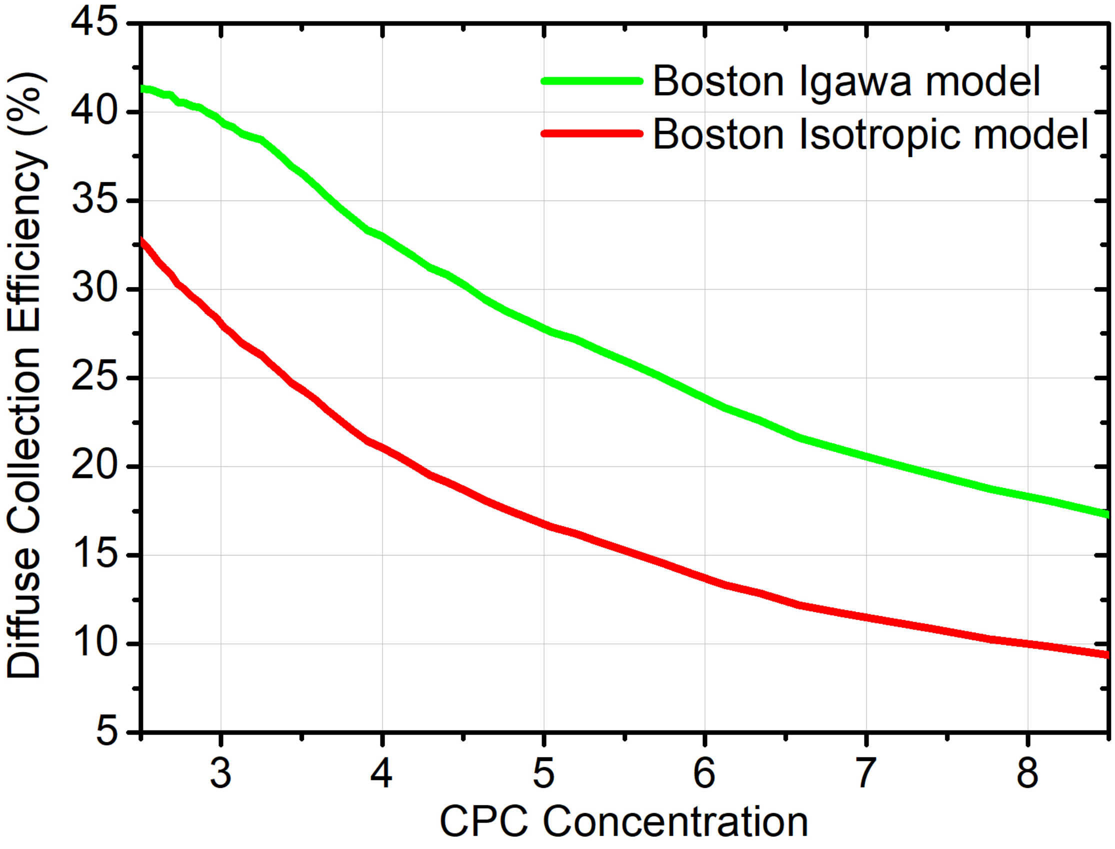

Figure 4-8: Diffuse energy collection efficiency of the polygon CPC.

Columbia (OH) and Phoenix (AZ) in a 2-axis tracking scheme. These maps show that despite the huge differences in geographic locations and weather types, the diffuse radiance energy distributions are quite similar in the 2-axis tracking scheme. Ideal CPCs are simulated as exemplary diffuse concentrator design. Figure 4-10 (a) shows the projected collectible diffuse irradiance in 2-axis tracking scheme in these four cities, and (b) shows the collection efficiency by normalizing the collectible energy to the 90° acceptance angle concentrator case. Despite the different collectible diffuse energy level in the 4 cities due to the diffuse energy abundance, the diffuse collection efficiency increases with the acceptance angle in the similar trend. This agrees with the similar diffuse radiance energy distribution in Figure 4-9.

Figure 4-11 illustrates the projected collectible diffuse energy with an ideal CPC with a 40° semi-acceptance angle mounted on a 2-axis tracker across the United States. The map is generated by interpolation based on the simulation conducted on the 221 Class 1 TMY3 stations (represented as red dot). The diffuse energy collection efficiency is determined using the same method as above. The collectible diffuse energy shows a non-uniform distribution across USA in Figure 4-11 (a). It reaches 600 kWh/m^2 in the southeast while remains 400 kWh/m^2 in the western United States. It is very different from the global solar irradiance distribution where the southwest area has the most abundant global irradiance. This is because the western area has dry weather thus most of the solar irradiance is not scattered and accounted as DNI, leaving relatively less diffuse irradiance. On the other hand, Figure 4-11 (b) shows the diffuse energy collecting efficiency is consistently 68%-70% across the USA. Again, it agrees with the similar diffuse distribution form in Figure 4-9. This suggests a quite counterintuitive conclusion that despite the differences in solar irradiance resources, geographic locations and weather conditions, designing a general diffuse concentrator applied to the whole USA market is reasonable, in the perspective of diffuse energy collecting efficiency.

This simulation framework can also be applied to low concentration system that deploys non-tracking or azimuth tracking schemes. In low concentration systems, the concentrator simultaneously concentrate the direct irradiance and the diffuse irradi-

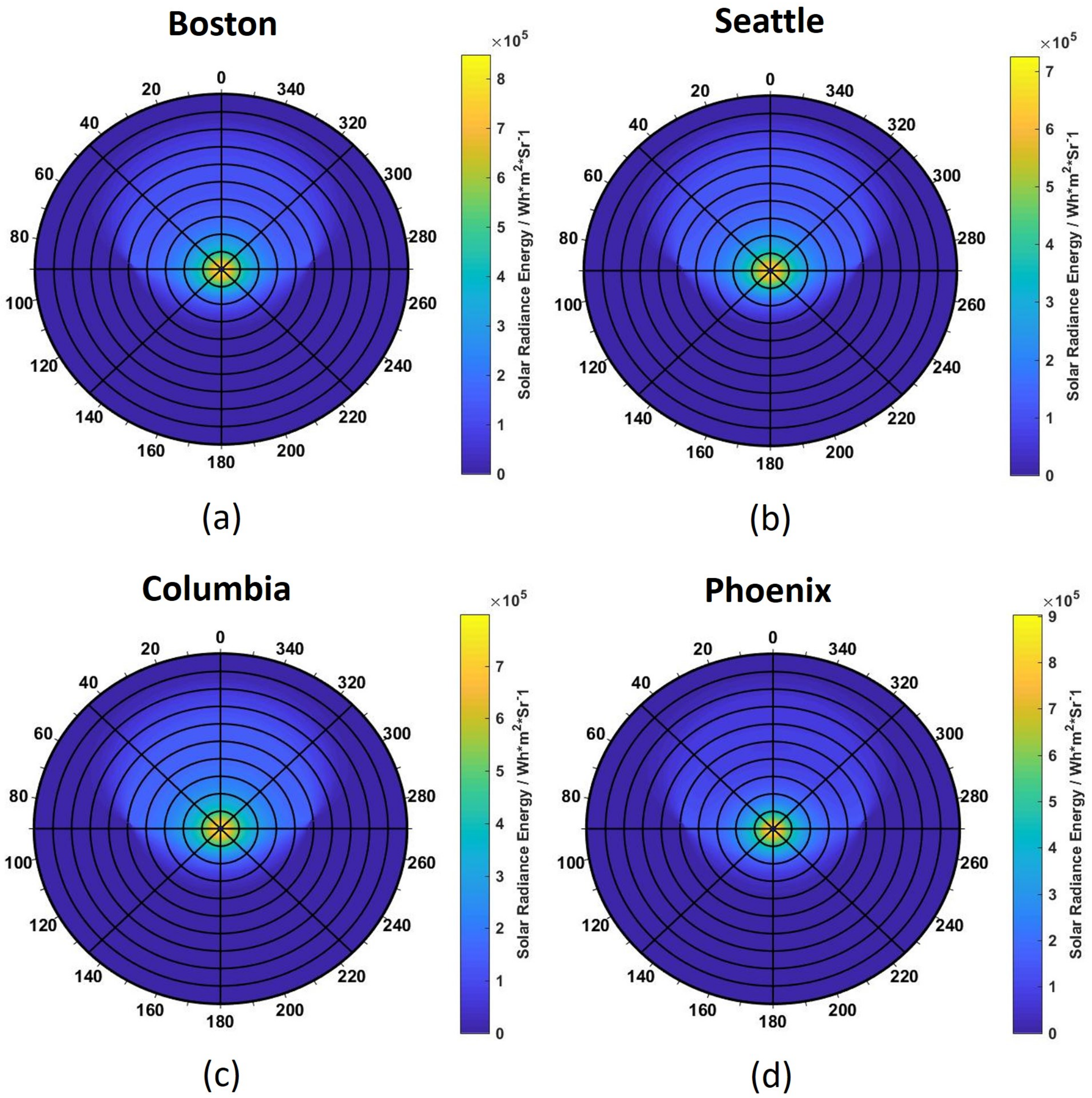

Figure 4-9: Annualized diffuse radiance energy map of Boston, Seattle, Columbia and Phoenix in 2-axis Scheme.

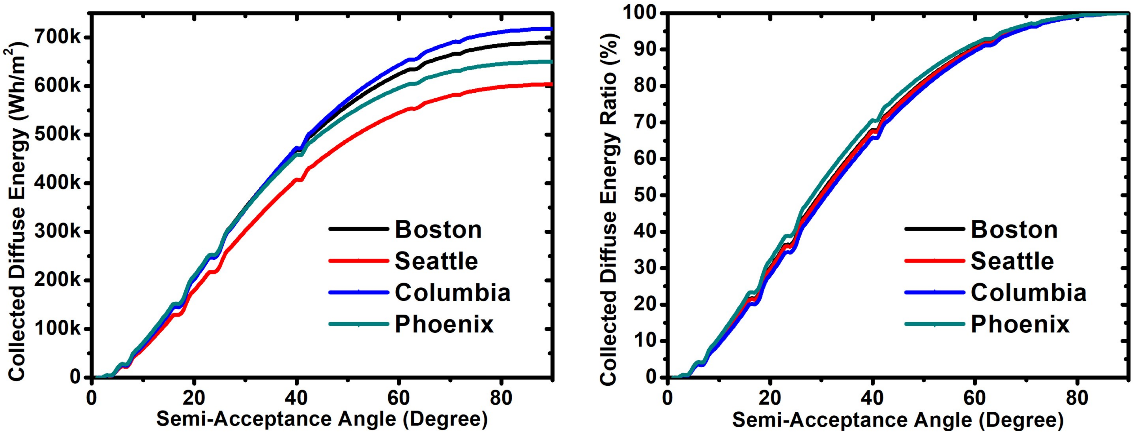

(a) (b)

Figure 4-10: (a)Collectible diffuse energy by ideal CPC; (b) Diffuse energy collection efficiency by ideal CPC.

ance so both the DNI and the diffuse radiance distributions shall be considered. The annualized diffuse radiance energy distribution map and the annualized DNI radiance energy distribution map of Boston in non-tracking scheme are plotted in Figure 4-12 (a) and (b). Anisotropic CPC performance is simulated by optimizing the horizontal acceptance angle, vertical acceptance angle and the CPC altitude angle. The CPC azimuth angle is fixed to 180° facing south. Figure 4-12 (c) shows the collectible solar energy with different acceptance angle design and (d) shows the corresponding optimized altitude angle.

4.5 Conclusion

In this chapter, we proposed to combine anisotropic diffuse radiance model with TMY3 meteorological dataset to generate annualized diffuse radiance energy distribution map. This approach provides an accurate reference for efficient energy-production-oriented diffuse concentrator designs. We conducted an outdoor diffuse radiance distribution measurement and verified the validity of the Igawa model. Our approach predicts that >50% more diffuse energy can be harvested, compared to the commonly used isotropic model. It indicates that diffuse concentration is an valu-

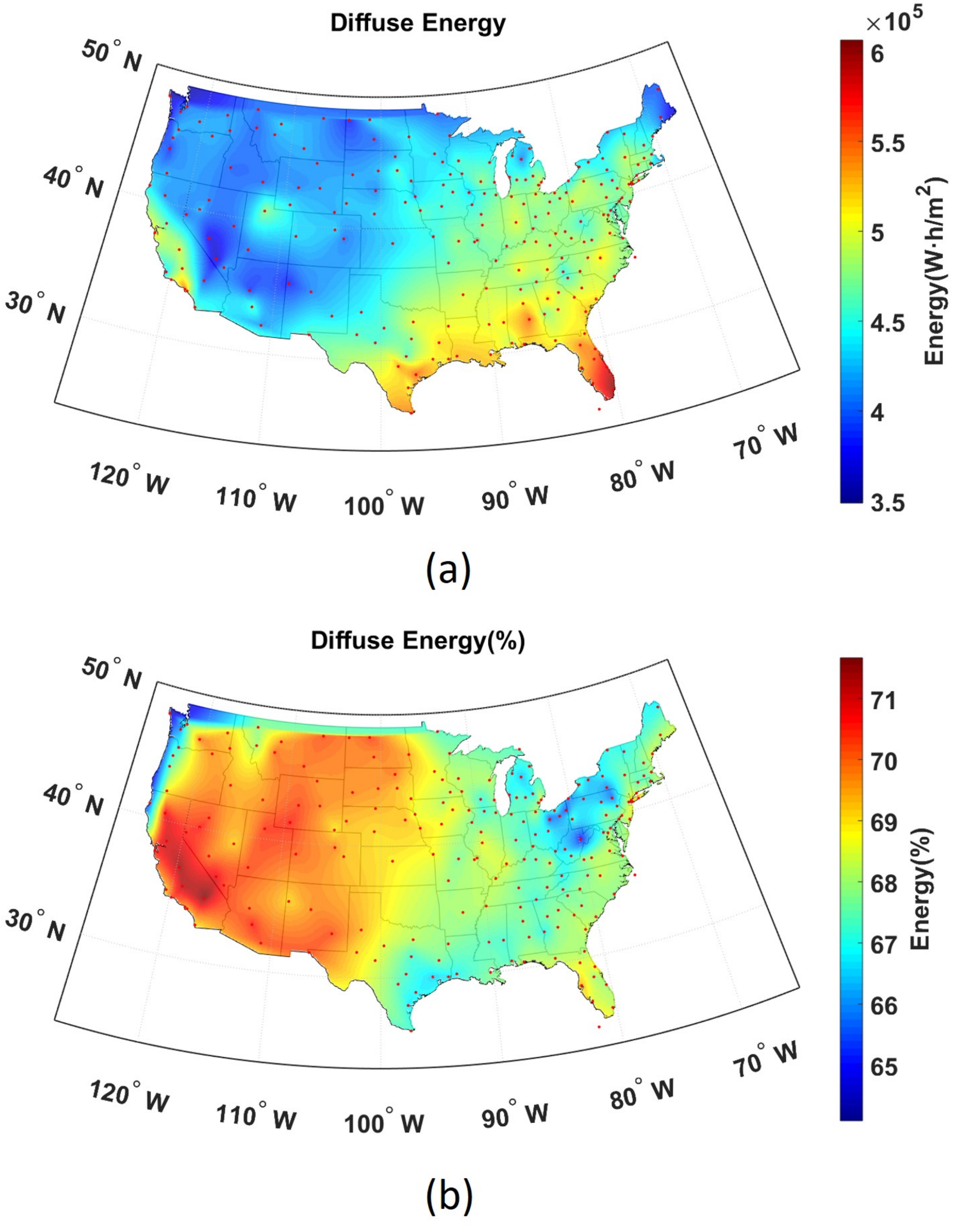

Figure 4-11: (a) Projected diffuse energy, (b) Diffuse collection efficiency of concentrator with 40° semi-acceptance angle across the United States.

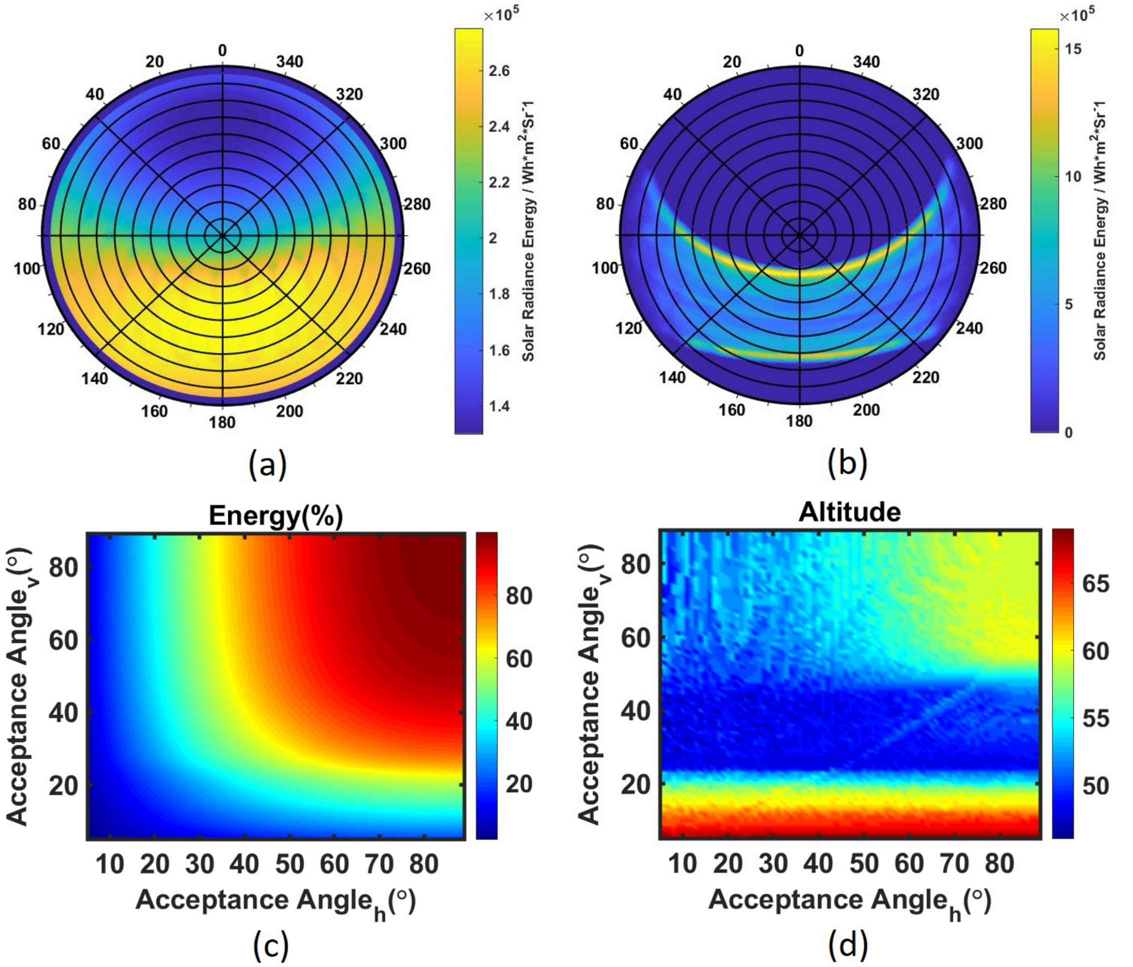

Figure 4-12: (a) Annualized diffuse radiance energy distribution map of Boston in non-tracking scheme; (b) Annualized DNI radiance energy distribution map of Boston in non-tracking scheme; (c) Solar irradiance collecting efficiency of an anisotropic CPC; (d) Optimum altitude angle of the CPC at different acceptance angle.

able approach to further drive down the cost of micro hybrid CPV module. A 5X dielectric diffuse concentrator can harvest 80% of the total diffuse energy. Another anti-intuitive finding is that in 2-axis tracking scheme, the diffuse radiance energy distribution is very consistent across the United States. It's suggesting that designing a universal diffuse concentrator can effectively work across the United States.

Chapter 5

Conclusions and Future Work

5.1 Summary and Conclusions

In Chapter 2, we demonstrated the multi-functional Si platform that can simultaneously act as the secondary concentrator for DNI collection and diffuse harvesting device. The module concentration-acceptance-angle product is improved by 46% by the micro cavity secondary concentrator and delivered state-of-the-art value as 0.68. The fabricated Si cell exhibits comparable harvesting efficiency compared to IBC cells fabricated from normal Si wafer. The micro hybrid concentrator photovoltaic module is predicted to gain over 17% efficiency improvement compared to CPV-only case.

In Chapter 3, we leveraged the materials dispersion properties and optical structures to develop the novel micro-prism-array spectrum splitting optics. The optics delivered 80% broadband transmission, as-designed spectrum splitting capability and outstanding minimal beam deflection. This optics showed great potential to enable a lateral-arrayed multi-junction micro CPV for the first time.

In Chapter 4, we proposed the novel approach to simulate the annualized radiance energy distribution. Compared to the previous isotropic model, our approach predicted over 50% more diffuse energy that can be collected by diffuse concentrator. This method significantly improved the bankability of micro hybrid CPV system and will improve the reliability evaluation of the system performance.

5.2 Future Work

In this thesis, the outstanding optics performances have been demonstrated. However, these optics haven't been successfully integrated to deliver a module efficiency due to the difficulties in micro cells fabrication. Thus, during the preparation of this thesis, we are still seeking collaborators to prototype a micro hybrid concentrator module with high-efficiency multi-junction cells. Besides, we are collaborating with Sandia National Lab to combine our diffuse simulation model and thoroughly conduct cost model analysis on micro hybrid CPV systems. It shall be mentioned that to achieve cost-effective micro hybrid concentrator photovoltaic module, the multi-junction cells fabrication cost must be reduced. It's mainly limited by the high price of Ge and III-V substrates and the limited substrate reuse due to the material fragility. An important solution is the Ge-on-Si approach that is part of the LAMB project, which by innovatively patterning and growing Ge epitaxially on Si substrate, can potentially improve the substrate reuse to hundreds of times and suppress the materials cost to the minimal level.

In the WPV project describe in Chapter 2, currently the multi-functional Si platform is integrated as a whole wafer. One improvement approach is to replace the whole wafer to discrete small Si cells and integrate with diffuse concentrator. Since Chapter 4 has suggested the strong forward scattering nature of diffuse radiation, the Si cell area can be effectively reduced by concentrator to further reduce the cost from Si materials and improve the cell performance. Besides, currently the Si wafer is fragile with the through-hole cavity and exhibits limited process yield. Segmentation of the Si cell can significantly reduce the wafer breaking risk. This process is also compatible with the transfer printing process for III-V cells assembly, thus introduces minimal extra module assembly cost. The extra diffuse optics molding cost is also minimal since it can be monolithically molded with the primary concentrator for DNI.

The micro-prism optics in Chapter 3 is effective in a 3J lateral-arrayed micro concentrator photovoltaic system. However, it will not gain substantial efficiency improvement by introducing more junctions, due to the overlap of spots in continuous wavelength, especially in near-IR wavelength. Unfortunately this phenomena is fundamentally limited by the materials dispersion properties. According to Kramer-Kronig relations, the optical dispersion happens strongly near an absorption peak. Thus the fine spectrum splitting capability of this optics originates from the strong absorption in the UV region. To improve the dispersion in near-IR region, we need to introduce absorption in the visible region, which is unfavored to maintain high optical transmission. To further improve the module efficiency with current optics, a possible approach is to adopt low-cost down-conversion and up-conversion coating materials at the cell edge. [111,112] However, this approach needs substantial improvements on the conversion efficiencies to be feasible. Another more feasible method is to adopt tandem structure in the long wavelength cells with the compromise on fabrication complexities and cost. The micro-prism optics also has great potential in the spectrometer application since it has high broadband transmission and no high order issues that exist in grating based technologies.

The model in Chapter 4 can be expanded to other photovoltaic systems like Si panel and low concentration photovoltaics with different tracking methods like non-tracking and azimuth tracking. One specifically interesting application is building integrated photovoltaics, since buildings orientation can vary, while accurate angular distribution of solar energy is critical to design and evaluate the building integrated photovoltaic systems. It will also be very interesting to apply non-imaging optics methods like simultaneous multiple surface to design diffuse concentrator and optimize it based on cost models.

Appendix A

Annualized Diffuse Radiance Energy Distribution Simulation Code in Two-Axis Tracking Scheme

A.1 Code Main Body

```
% Copyright: @PMAT MIT
% Please do not copy or distribute without permission.
% Contact: duanhui@mit.edu; hujuejun@mit.edu.

% Citation statement: This model is based on NSRDB TMY3 dataset and
% Igawa diffuse radiance model. Data reading and processing implement
% functions from PV_LIB toolbox.

% This model first reads data from TMY3 dataset, use PV_LIB to
% process the data format, then apply Igawa model to generate
% diffuse radiance map.

```

```
% Read TMY3 data, get the full station list.
FileList = dir('*.csv');
N = size(FileList,1);

for k=1:N

TMY=pvl_readtmy3(FileList(k).name);

% Construct time and location data for processing.
Tstruct=pvl_maketimestruct(TMY.DateNumber-datenum(0,0,0,0,30,0),...
    TMY.SiteTimeZone);
location=pvl_makelocationstruct(TMY.SiteLatitude,TMY.SiteLongitude,...
    TMY.SiteElevation);

% Calculate the sun position and solar time
[SunAz_deg, SunAl_deg, ApparentSunAl, SolarTime] = pvl_ephemeris...
    (Tstruct,location,100*TMY.Pressure,TMY.DryBulb);
SunZenith_deg=90-SunAl_deg;
SunAz_rad=deg2rad(SunAz_deg);
SunAl_rad=deg2rad(SunAl_deg);

% TMY data processing for Igawa model implementation. Variable names
% consistent with Igawa model paper

% Read DHI and GHI.
Eed=TMY.DHI;
Eeg=TMY.GHI;

% Calculate Air mass.
m=pvl_relativeairmass(SunZenith_deg, 'Kastenyoung1989');

% Extraterrestrial direct normal irradiance.
Eeo=1367;

% Calculate standard global irradiance.
Seeg=0.84*Eeo./m.*exp(-0.0675.*m);
```

```

% Calculate clear sky index.
Kc=Eeg./Seeg;

% Calculate cloudless index
Ces=0.01299+0.07698*m-0.003857*m.^2+0.0001054*m.^3-0.000001031*m.^4;
Ce=Eed./Eeg;
Cle=(1-Ce)./(1-Ces);

% Calculate the sky index.
Si=Kc+real(sqrt(Cle));
Si((Si>2)&(Si<2.1))=2;
Si(Si>2)=nan;

% Initialize the diffuse radiance maps.
Diffuse_map_Igawa=zeros([181,360]);
Diffuse_map_Isotropic=zeros([181,360]);

% Only include data points with GHI>0.
valid_index=find(Eeg>0);

% Calculate the radiance energy map for each hourly data. Addup to ...
   generate
% annualized radiance energy map.
for x=1:length(valid_index)
   i=valid_index(x);
   if isnan(Si(i))

   else

   % Igawa diffuse radiance map generation
   New_map=Diffuse_2_axis_Cal(Si(i),SunAl_deg(i),'Igawa');
   % Diffuse radiance map addup
   if isreal(New_map)
   Diffuse_map_Igawa=Diffuse_map_Igawa+Eed(i)*New_map;
   else
```

```
       return
   end

   % Isotropic diffuse radiance map generation
   New_map=Diffuse_2_axis_Cal(Si(i),SunAl_deg(i),'Isotropic');
   % Diffuse radiance map addup
   if isreal(New_map)
   Diffuse_map_Isotropic=Diffuse_map_Isotropic+Eed(i)*New_map;
   else
       return
   end

   end
end

% To turn the radiance map unit to W*h/m^2/Sr
% Normalize to 1 degree * 1 degree mesh.

% Generate DNI maps
DNI_map=ones([181,360]);
azimuth=(-180:1:179);
altitude=(-90:1:90);
[new_Azimuth,new_Altitude]=meshgrid(azimuth,altitude);
Tracker_altitude=90;
Tracker_azimuth=0;
angle_diff=acosd(sind(Tracker_altitude).*sind(new_Altitude)+...
    cosd(Tracker_altitude).*cosd(new_Altitude).*cosd...
    (abs(Tracker_azimuth-new_Azimuth)));
% DNI is confined in the 2.5 half degree cone.
DNI_map(angle_diff>2.5)=0;

% Normalize the mesh to the DHI value, the DHI sensor is pointing to the
% sky dome.
correct=abs(cosd(new_Altitude).*cosd(angle_diff));
Normalized_factor=sum(sum(correct.*DNI_map));
DNI_map=DNI_map/Normalized_factor*sum(TMY.DNI);
```

```


DNI_map_SI=DNI_map*(180/pi)^2;
Diffuse_map_Isotropic_SI=Diffuse_map_Isotropic*(180/pi)^2;
Diffuse_map_Igawa_SI=Diffuse_map_Igawa*(180/pi)^2;

save([pwd '\' num2str(TMY.SiteID) '\Two_axis_tracking_map.mat'],...
    'Diffuse_map_Igawa','Diffuse_map_Igawa_SI','Diffuse_map_Isotropic_SI',...
    'Diffuse_map_Isotropic','DNI_map','DNI_map_SI');

end
```

A.2 Called Functions

A.2.1 Diffuse Le Calculation

```

function [Tracker_Le] = Diffuse_2_axis_Cal(Si,SunAl_deg,Model)
% This function calculates the 2-axis diffuse radiance map in the ...
    tracker
% coordinate with sun in the tracker dome.

azimuth=(-180:1:179);
altitude=(-90:1:90);

[Tracker_Azimuth,Tracker_Altitude]=meshgrid(azimuth,altitude);
r=ones(size(Tracker_Azimuth));
[x,y,z] = ...
    sph2cart(deg2rad(Tracker_Azimuth),deg2rad(Tracker_Altitude),r);
R = roty(90-Sun_deg);

earth_cartesian=R*[x(:),y(:),z(:)]';

new_x=earth_cartesian(1,:);
```

```
new_x=reshape(new_x,size(Tracker_Azimuth));
new_y=earth_cartesian(2,:Al);
new_y=reshape(new_y,size(Tracker_Azimuth));
new_z=earth_cartesian(3,:);
new_z=reshape(new_z,size(Tracker_Azimuth));

[earth_Azimuth,earth_Altitude,r]=cart2sph(new_x,new_y,new_z);
earth_Azimuth=rad2deg(earth_Azimuth);
earth_Altitude=rad2deg(earth_Altitude);
sun_az=0;
angle_diff=acosd(sind(SunAl_deg).*sind(earth_Altitude)+cosd(SunAl_deg)*...
    cosd(earth_Altitude).*cosd(abs(sun_az-earth_Azimuth)));

if strcmp('Igawa',Model)
    new_Le=graduation_f(Si,earth_Altitude).*indicatrix_f(Si,angle_diff)...
        ./(graduation_f(Si,90).*indicatrix_f(Si,(90-SunAl_deg)));
elseif strcmp(Model,'Isotropic')
    new_Le=ones(size(Tracker_Azimuth));
else
    error('Model input error')
    return
end

sun_altitude=90;
sun_azimuth=0;
angle_diff=acosd(sind(sun_altitude).*sind(Tracker_Altitude)+...
    cosd(sun_altitude).*cosd(Tracker_Altitude).*...
    cosd(abs(sun_azimuth-Tracker_Azimuth)));

new_Le(earth_Altitude<5)=0;
new_Le(angle_diff<2.5)=0;

% Normalize the mesh to the DHI value, the DHI sensor is pointing to the
% sky dome.
sky_altitude=SunAl_deg;
sky_azimuth=-180;
```

```
angle_diff=acosd(sind(sky_altitude).*sind(Tracker_Altitude)+...
    cosd(sky_altitude).*cosd(Tracker_Altitude).*...
    cosd(abs(sky_azimuth-Tracker_Azimuth)));
correct=abs(cosd(Tracker_Altitude).*cosd(angle_diff));
Normalized_factor=sum(sum(correct.*new_Le));
Tracker_Le=new_Le/Normalized_factor;
end
```

A.2.2 Graduation Function

```
function [result] = graduation_f(Si,angle)
a=4.5/(1+0.15*exp(3.4*Si))-1.04;
b=-1/(1+0.17*exp(1.3*Si))-0.05;
c=1.77*(1.22*Si)^3.56*exp(0.2*Si)*(2.1-Si)^0.8;
d=-3.05/(1+10.6*exp(-3.4*Si));
e=0.48/(1+245*exp(-4.13*Si));

result=1+a*exp(b./sind(angle));
end
```

A.2.3 Scattering Indicatrix Fucntion

```
function [ result ] = indicatrix_f(Si, angle )
a=4.5/(1+0.15*exp(3.4*Si))-1.04;
b=-1/(1+0.17*exp(1.3*Si))-0.05;
c=1.77*(1.22*Si)^3.56*exp(0.2*Si)*(2.1-Si)^0.8;
d=-3.05/(1+10.6*exp(-3.4*Si));
e=0.48/(1+245*exp(-4.13*Si));

result=1+c.*(exp(d*deg2rad(angle))-exp(d*deg2rad(90)))+e*(cosd(angle)).^2;
end
```

Bibliography

[1] BP, "BP Statistical Review of World Energy 2018," [Online], https://www.bp.com/content/dam/bp/business-sites/en/global/corporate/pdfs/energy-economics/statistical-review/bp-stats-review-2018-full-report.pdf.

[2] P. Würfel and U. Würfel, *Physics of Solar Cells: From Basic Principles to Advanced Concepts, 3rd Edition.* Wiley, 2016.

[3] REN21, "RENEWABLES 2018 GLOBAL STATUS REPORT," [Online], http://www.ren21.net/wp-content/uploads/2018/06/17-8652_GSR2018_FullReport_web_final_.pdf.

[4] D. R. Myers, *Solar Radiation: Practical Modeling for Renewable Energy Applications, 1st Edition.* CRC Press, 2017.

[5] P. Blanc, B. Espinar, N. Geuder, C. Gueymard, R. Meyer, R. Pitz-Paal, B. Reinhardt, D. Renné, M. Sengupta, L. Wald, and S. Wilbert, "Direct normal irradiance related definitions and applications: The circumsolar issue," *Solar Energy*, vol. 110, pp. 561 – 577, 2014. [Online]. Available: http://www.sciencedirect.com/science/article/pii/S0038092X14004824

[6] S. Vashishtha, "DIFFERENTIATE BETWEEN THE DNI, DHI AND GHI," [Online], https://firstgreenconsulting.wordpress.com/2012/04/26/differentiate-between-the-dni-dhi-and-ghi/.

[7] National Renewable Energy Laboratory, "Reference Solar Spectral Irradiance: Air Mass 1.5," [Online], https://rredc.nrel.gov/solar//spectra/am1.5/.

[8] W. Shockley and H. J. Queisser, "Detailed balance limit of efficiency of p-n junction solar cells," *Journal of Applied Physics*, vol. 32, no. 3, pp. 510–519, 1961. [Online]. Available: https://doi.org/10.1063/1.1736034

[9] C. H. Henry, "Limiting efficiencies of ideal single and multiple energy gap terrestrial solar cells," *Journal of Applied Physics*, vol. 51, no. 8, pp. 4494–4500, 1980. [Online]. Available: https://doi.org/10.1063/1.328272

[10] J. Koshel, *Illumination Engineering: Design with Nonimaging Optics.* Wiley, 2013.

[11] M. Born, E. Wolf, A. B. Bhatia, P. C. Clemmow, D. Gabor, A. R. Stokes, A. M. Taylor, P. A. Wayman, and W. L. Wilcock, *Principles of Optics: Electromagnetic Theory of Propagation, Interference and Diffraction of Light*, 7th ed. Cambridge University Press, 1999.

[12] “The flow-line method for designing nonimaging optical systems,” in *Nonimaging Optics*, R. Winston, J. C. Miñano, and P. Benítez, Eds. Academic Press, 2005, pp. 99 – 158. [Online]. Available: http://www.sciencedirect.com/science/article/pii/B9780127597515500063

[13] “Simultaneous multiple surface design method,” in *Nonimaging Optics*, R. Winston, J. C. Miñano, and P. Benítez, Eds. Academic Press, 2005, pp. 181 – 218. [Online]. Available: http://www.sciencedirect.com/science/article/pii/B9780127597515500087

[14] D. M. Chapin, C. S. Fuller, and G. L. Pearson, “A new silicon p-n junction photocell for converting solar radiation into electrical power,” *Journal of Applied Physics*, vol. 25, no. 5, pp. 676–677, 1954. [Online]. Available: https://app.dimensions.ai/details/publication/pub.1057788714

[15] A. Luque and S. Hegedus, *Handbook of Photovoltaic Science and Engineering, Second Edition.* Wiley, 2011.

[16] National Renewable Energy Laboratory, “Best Research-Cell Efficiency Chart,” [Online], https://www.nrel.gov/pv/cell-efficiency.html.

[17] Wikipedia, “Photovoltaics,” [Online], https://en.wikipedia.org/wiki/Photovoltaics.

[18] S. Comello, S. Reichelstein, and A. Sahoo, “The road ahead for solar PV power,” *Renewable and Sustainable Energy Reviews*, vol. 92, pp. 744 – 756, 2018. [Online]. Available: http://www.sciencedirect.com/science/article/pii/S1364032118303125

[19] Fraunhofer Institute for Solar Energy Systems, “PHOTOVOLTAICS REPORT,” [Online], 2019, https://www.ise.fraunhofer.de/content/dam/ise/de/documents/publications/studies/Photovoltaics-Report.pdf.

[20] A. Goodrich, P. Hacke, Q. Wang, B. Sopori, R. Margolis, T. L. James, and M. Woodhouse, “A wafer-based monocrystalline silicon photovoltaics road map: Utilizing known technology improvement opportunities for further reductions in manufacturing costs,” *Solar Energy Materials and Solar Cells*, vol. 114, pp. 110 – 135, 2013. [Online]. Available: http://www.sciencedirect.com/science/article/pii/S0927024813000457

[21] Fraunhofer ISE and NREL, “Current status of concentrator photovoltaic (CPV) technology,” [Online], 2017, https://www.ise.fraunhofer.de/content/dam/ise/de/documents/publications/studies/cpv-report-ise-nrel.pdf.

[22] A. Luque, G. Sala, and I. Luque-Heredia, “Photovoltaic concentration at the onset of its commercial deployment,” *Progress in Photovoltaics: Research and Applications*, vol. 14, no. 5, pp. 413–428. [Online]. Available: https://onlinelibrary.wiley.com/doi/abs/10.1002/pip.705

[23] R. M. Swanson, “The promise of concentrators,” *Progress in Photovoltaics: Research and Applications*, vol. 8, no. 1, pp. 93–111. [Online]. Available: https://onlinelibrary.wiley.com/doi/abs/10.1002/%28SICI%291099-159X%28200001/02%298%3A1%3C93%3A%3AAID-PIP303%3E3.0.CO%3B2-S

[24] S. Kurtz, D. Myers, W. E. McMahon, J. Geisz, and M. Steiner, “A comparison of theoretical efficiencies of multi-junction concentrator solar cells,” *Progress in Photovoltaics: Research and Applications*, vol. 16, no. 6, pp. 537–546. [Online]. Available: https://onlinelibrary.wiley.com/doi/abs/10.1002/pip.830

[25] P. Benítez, J. C. M. nano, P. Zamora, R. Mohedano, A. Cvetkovic, M. Buljan, J. Chaves, and M. Hernández, “High performance fresnel-based photovoltaic concentrator,” *Optics Express*, vol. 18, no. S1, pp. A25–A40, Apr 2010. [Online]. Available: http://www.opticsexpress.org/abstract.cfm?URI=oe-18-101-A25

[26] M. A. Green, Y. Hishikawa, E. D. Dunlop, D. H. Levi, J. Hohl-Ebinger, M. Yoshita, and A. W. Ho-Baillie, “Solar cell efficiency tables (version 53),” *Progress in Photovoltaics: Research and Applications*, vol. 27, no. 1, pp. 3–12. [Online]. Available: https://onlinelibrary.wiley.com/doi/abs/10.1002/pip.3102

[27] M. Steiner, G. Siefer, T. Schmidt, M. Wiesenfarth, F. Dimroth, and A. W. Bett, “43% sunlight to electricity conversion efficiency using CPV,” *IEEE Journal of Photovoltaics*, vol. 6, no. 4, pp. 1020–1024, July 2016.

[28] J. E. Haysom, O. Jafarieh, H. Anis, K. Hinzer, and D. Wright, “Learning curve analysis of concentrated photovoltaic systems,” *Progress in Photovoltaics: Research and Applications*, vol. 23, no. 11, pp. 1678–1686. [Online]. Available: https://onlinelibrary.wiley.com/doi/abs/10.1002/pip.2567

[29] C. Kost, J. N. Mayer, J. Thomsen, N. Hartmann, C. Senkpiel, S. S.P. Philipps, Nold, S. Lude, N. Saad, J. Schmidt, and T. Schlegl, “Levelized cost of electricity: PV and CPV in comparison to other technologies,” in *29th European Photovoltaic Solar Energy Conference and Exhibition*, 2014, pp. 4086 – 4090.

[30] N. J. Ekins-Daukes, P. Sandwell, J. Nelson, A. D. Johnson, G. Duggan, and E. Herniak, “What does CPV need to achieve in order to succeed?” *AIP Conference Proceedings*, vol. 1766, no. 1, p. 020004, 2016. [Online]. Available: https://aip.scitation.org/doi/abs/10.1063/1.4962072

[31] National Renewable Energy Laboratory, “Solar Maps,” [Online], https://www.nrel.gov/gis/solar.html.

[32] C. A. Gueymard and S. M. Wilcox, "Assessment of spatial and temporal variability in the us solar resource from radiometric measurements and predictions from models using ground-based or satellite data," *Solar Energy*, vol. 85, no. 5, pp. 1068 – 1084, 2011. [Online]. Available: http://www.sciencedirect.com/science/article/pii/S0038092X11000855

[33] C. Domínguez, N. Jost, S. Askins, M. Victoria, and I. Antón, "A review of the promises and challenges of micro-concentrator photovoltaics," *AIP Conference Proceedings*, vol. 1881, no. 1, p. 080003, 2017. [Online]. Available: https://aip.scitation.org/doi/abs/10.1063/1.5001441

[34] G. N. Nielson, M. Okandan, J. L. Cruz-Campa, A. L. Lentine, W. C. Sweatt, V. P. Gupta, and J. S. Nelson, "Leveraging scale effects to create next-generation photovoltaic systems through micro- and nanotechnologies," vol. 8373, 2012. [Online]. Available: https://doi.org/10.1117/12.919464

[35] M. Wiesenfarth, I. Anton, and A. W. Bett, "Challenges in the design of concentrator photovoltaic (CPV) modules to achieve highest efficiencies," *Applied Physics Reviews*, vol. 5, no. 4, p. 041601, 2018. [Online]. Available: https://doi.org/10.1063/1.5046752

[36] M. W. Haney, T. Gu, and G. Agrawal, "Hybrid micro-scale CPV/PV architecture," in *2014 IEEE 40th Photovoltaic Specialist Conference (PVSC)*, June 2014, pp. 2122–2126.

[37] N. Hayashi, A. Matsushita, D. Inoue, M. Matsumoto, T. Nagata, H. Higuchi, Y. Aya, and T. Nakagawa, "Nonuniformity sunlight-irradiation effect on photovoltaic performance of concentrating photovoltaic using microsolar cells without secondary optics," *IEEE Journal of Photovoltaics*, vol. 6, no. 1, pp. 350–357, Jan 2016.

[38] E. Menard, M. Sullivan, J. Wilson, S. S. Brent Fisher, M. Meitl, K. Ghosal, and S. Burroughs, "Optics development for micro-cell based CPV modules," 2011. [Online]. Available: https://doi.org/10.1117/12.893385

[39] K.-T. Lee, Y. Yao, J. He, B. Fisher, X. Sheng, M. Lumb, L. Xu, M. A. Anderson, D. Scheiman, S. Han, Y. Kang, A. Gumus, R. R. Bahabry, J. W. Lee, U. Paik, N. D. Bronstein, A. P. Alivisatos, M. Meitl, S. Burroughs, M. M. Hussain, J. C. Lee, R. G. Nuzzo, and J. A. Rogers, "Concentrator photovoltaic module architectures with capabilities for capture and conversion of full global solar radiation," *Proceedings of the National Academy of Sciences*, vol. 113, no. 51, pp. E8210–E8218, 2016. [Online]. Available: https://www.pnas.org/content/113/51/E8210

[40] P. Zamora, P. Benítez, R. M. Arroyo, A. Cvetkovic, J. F. Vilaplana, Y. Li, M. Hernández, J. C. Chaves, and J. C. Miñano, "Experimental characterization of Fresnel-Köhler concentrators," *Journal of Photonics for*

Energy, vol. 2, no. 1, pp. 1 – 12 – 12, 2012. [Online]. Available: https://doi.org/10.1117/1.JPE.2.021806

[41] M. Buljan, J. C. M. nano, P. Benítez, R. Mohedano, and J. Chaves, "Improving performances of Fresnel CPV systems: Fresnel-RXI Köhler concentrator," *Optics Express*, vol. 22, no. S2, pp. A205–A210, Mar 2014. [Online]. Available: http://www.opticsexpress.org/abstract.cfm?URI=oe-22-102-A205

[42] J. S. Price, A. J. Grede, B. Wang, M. V. Lipski, B. Fisher, K.-T. Lee, J. He, G. S. Brulo, X. Ma, S. Burroughs, C. D. Rahn, R. Nuzzo, J. A. Rogers, and N. C. Giebink, "High-concentration planar microtracking photovoltaic system exceeding 30% efficiency," *Nature Energy*, vol. 2, p. 17113, Jul 2017, article. [Online]. Available: https://doi.org/10.1038/nenergy.2017.113

[43] N. Yamada, T. Ijiro, W. Goto, K. Okamoto, K. Dobashi, and T. Shiobara, "Development of silicone-encapsulated CPV module based on LED package technology," in *2013 IEEE 39th Photovoltaic Specialists Conference (PVSC)*, June 2013, pp. 0493–0496.

[44] N. Tien and S. Shin, "A novel concentrator photovoltaic (CPV) system with the improvement of irradiance uniformity and the capturing of diffuse solar radiation," *Applied Sciences*, vol. 6, no. 9, p. 251, sep 2016. [Online]. Available: https://doi.org/10.3390%2Fapp6090251

[45] N. Yamada and K. Okamoto, "Experimental measurements of a prototype high concentration Fresnel lens CPV module for the harvesting of diffuse solar radiation," *Optics Express*, vol. 22, no. S1, pp. A28–A34, Jan 2014. [Online]. Available: http://www.opticsexpress.org/abstract.cfm?URI=oe-22-101-A28

[46] S. Paap, V. Gupta, A. Tauke-Pedretti, P. Resnick, C. Sanchez, G. Nielson, J. L. Cruz-Campa, B. Jared, J. Nelson, M. Okandan, and W. Sweatt, "Cost analysis of flat-plate concentrators employing microscale photovoltaic cells for high energy per unit area applications," in *2014 IEEE 40th Photovoltaic Specialist Conference (PVSC)*, June 2014, pp. 2926–2929.

[47] S. M. Paap, V. P. Gupta, J. L. Cruz-Campa, M. Okandan, W. C. Sweatt, B. H. Jared, B. Anderson, G. N. Nielson, A. Tauke-Pedretti, and J. S. Nelson, "Cost analysis for flat-plate concentrators employing microscale photovoltaic cells," *2013 IEEE 39th Photovoltaic Specialists Conference (PVSC)*, pp. 3431–3434, 2013.

[48] R. A. Matula, "Electrical resistivity of copper, gold, palladium, and silver," *Journal of Physical and Chemical Reference Data*, vol. 8, no. 4, pp. 1147–1298, 1979. [Online]. Available: https://doi.org/10.1063/1.555614

[49] B. Shu, U. Das, J. Appel, B. McCandless, S. Hegedus, and R. Birkmire, "Alternative approaches for low temperature front surface passivation of interdigitated

back contact silicon heterojunction solar cell," in *2010 35th IEEE Photovoltaic Specialists Conference*, June 2010, pp. 003 223–003 228.

[50] Z. Shu, U. Das, J. Allen, R. Birkmire, and S. Hegedus, "Experimental and simulated analysis of front versus all-back-contact silicon heterojunction solar cells: effect of interface and doped a-si:h layer defects," *Progress in Photovoltaics: Research and Applications*, vol. 23, no. 1, pp. 78–93. [Online]. Available: https://onlinelibrary.wiley.com/doi/abs/10.1002/pip.2400

[51] Sandia National Laboratories, "Final Report MEPV," [Online], https://prod-ng.sandia.gov/techlib-noauth/access-control.cgi/2015/151071.pdf.

[52] National Renewable Energy Laboratory, "National Solar Radiation Database," [Online], https://nsrdb.nrel.gov/.

[53] F. Dimroth, T. N. D. Tibbits, M. Niemeyer, F. Predan, P. Beutel, C. Karcher, E. Oliva, G. Siefer, D. Lackner, P. Fuß-Kailuweit, A. W. Bett, R. Krause, C. Drazek, E. Guiot, J. Wasselin, A. Tauzin, and T. Signamarcheix, "Four-junction wafer-bonded concentrator solar cells," *IEEE Journal of Photovoltaics*, vol. 6, no. 1, pp. 343–349, Jan 2016.

[54] H. Föll, "Semiconductor Technology," [Online], University of Kiel, 2011, https://www.tf.uni-kiel.de/matwis/amat/semitech_en/index.html.

[55] L. Z. Broderick, B. R. Albert, B. S. Pearson, L. C. Kimerling, and J. Michel, "Design for energy: Modeling of spectrum, temperature and device structure dependences of solar cell energy production," *Solar Energy Materials and Solar Cells*, vol. 136, pp. 48 – 63, 2015. [Online]. Available: http://www.sciencedirect.com/science/article/pii/S0927024814006813

[56] Y. Mols, L. Zhao, G. Flamand, M. Meuris, and J. Poortmans, "Annual energy yield: A comparison between various monolithic and mechanically stacked multijunction solar cells," in *2012 38th IEEE Photovoltaic Specialists Conference*, June 2012, pp. 002 092–002 095.

[57] M. A. Steiner, J. F. Geisz, J. S. Ward, I. García, D. J. Friedman, R. R. King, P. T. Chiu, R. M. France, A. Duda, W. J. Olavarria, M. Young, and S. R. Kurtz, "Mechanically stacked four-junction concentrator solar cells," in *2015 IEEE 42nd Photovoltaic Specialist Conference (PVSC)*, June 2015, pp. 1–3.

[58] H. Shen, T. Duong, J. Peng, D. Jacobs, N. Wu, J. Gong, Y. Wu, S. K. Karuturi, X. Fu, K. Weber, X. Xiao, T. P. White, and K. Catchpole, "Mechanically-stacked perovskite/CIGS tandem solar cells with efficiency of 23.9% and reduced oxygen sensitivity."

[59] S. Essig, C. Allebé, T. Remo, J. F. Geisz, M. A. Steiner, K. Horowitz, L. Barraud, J. S. Ward, M. Schnabel, A. Descoeudres, D. Young, M. Woodhouse, M. Despeisse, C. Ballif, and A. Tamboli, "Raising the one-sun

conversion efficiency of III-V/Si solar cells to 32.8% for two junctions and 35.9% for three junctions," *Nature Energy*, vol. 2, pp. 17 144 EP –, Aug 2017, article. [Online]. Available: https://doi.org/10.1038/nenergy.2017.144

[60] I. Mathews, D. O'Mahony, K. Thomas, E. Pelucchi, B. Corbett, and A. P. Morrison, "Adhesive bonding for mechanically stacked solar cells," *Progress in Photovoltaics: Research and Applications*, vol. 23, no. 9, pp. 1080–1090, 2015. [Online]. Available: https://onlinelibrary.wiley.com/doi/abs/10.1002/pip.2517

[61] A. Sachenko, M. Kulish, I. Sokolovskyi, and V. Kostylyov, "Lateral multijunction photovoltaic cells," *Semiconductor Physics, Quantum Electronics and Optoelectronics*, vol. 16, no. 1, pp. 1–17, 2013. [Online]. Available: http://journal-spqeo.org.ua/n1_2013/P001-017abstr.html

[62] A. L. Lentine, G. N. Nielson, M. Okandan, J. Cruz-Campa, and A. Tauke-Pedretti, "Voltage matching and optimal cell compositions for microsystem-enabled photovoltaic modules," *IEEE Journal of Photovoltaics*, vol. 4, no. 6, pp. 1593–1602, Nov 2014.

[63] M. K. Alam, F. H. Khan, and A. S. Imtiaz, "An efficient power electronics solution for lateral multi-junction solar cell systems," in *IECON 2011 - 37th Annual Conference of the IEEE Industrial Electronics Society*, Nov 2011, pp. 4373–4378.

[64] M. K. Alam, F. Khan, and A. M. Imtiaz, "Optimization of subcell interconnection for multijunction solar cells using switching power converters," *IEEE Transactions on Sustainable Energy*, vol. 4, no. 2, pp. 340–349, April 2013.

[65] M. K. Alam, F. H. Khan, and A. M. Imtiaz, "Interconnection and optimization issues of multijunction solar cells — a new mitigation approach using switching power converters," in *2012 Twenty-Seventh Annual IEEE Applied Power Electronics Conference and Exposition (APEC)*, Feb 2012, pp. 583–589.

[66] A. L. Lentine, G. N. Nielson, M. Okandan, W. C. Sweatt, J. L. Cruz-Campa, and V. Gupta, "Optimal cell connections for improved shading, reliability, and spectral performance of microsystem enabled photovoltaic (MEPV) modules," in *2010 35th IEEE Photovoltaic Specialists Conference*, June 2010, pp. 003 048–003 054.

[67] A. L. Lentine, G. N. Nielson, M. Okandan, J. Cruz-Campa, and A. Tauke-Pedretti, "Enhanced efficiency for voltage matched stacked multi-junction cells: Optimization with yearly temperature and spectra variations," in *2013 IEEE 39th Photovoltaic Specialists Conference (PVSC)*, June 2013, pp. 0788–0791.

[68] A. Carlson, A. M. Bowen, Y. Huang, R. G. Nuzzo, and J. A. Rogers, "Transfer printing techniques for materials assembly and micro/nanodevice fabrication," *Advanced Materials*, vol. 24, no. 39, pp. 5284–5318, 2012. [Online]. Available: https://onlinelibrary.wiley.com/doi/abs/10.1002/adma.201201386

[69] C. Bower, “Micro-Transfer-Printing (microTP):Technology Overview,” [Online], X-Celeprint, 2014, http://sites.ieee.org/ocs-cpmt/files/2013/06/CPMT_2014.02.11_V1_uTP.pdf.

[70] B. Furman, E. Menard, A. Gray, M. Meitl, S. Bonafede, D. Kneeburg, K. Ghosal, R. Bukovnik, W. Wagner, J. Gabriel, S. Seel, and S. Burroughs, “A high concentration photovoltaic module utilizing micro-transfer printing and surface mount technology,” in *2010 35th IEEE Photovoltaic Specialists Conference*, June 2010, pp. 000 475–000 480.

[71] R. Bukovnik, E. Menard, M. Meitl, S. Bonafede, R. McNeill, W. Wagner, S. Seel, and S. Burroughs, “A micro-transfer printed high efficiency flexible photovoltaic panel,” in *2011 37th IEEE Photovoltaic Specialists Conference*, June 2011, pp. 001 543–001 547.

[72] S. Burroughs, R. Conner, B. Furman, E. Menard, A. Gray, M. Meitl, S. Bonafede, D. Kneeburg, K. Ghosal, R. Bukovnik, W. Wagner, S. Seel, and M. Sullivan, “A new approach for a low cost CPV module design utilizing micro-transfer printing technology,” *AIP Conference Proceedings*, vol. 1277, no. 1, pp. 163–166, 2010. [Online]. Available: https://aip.scitation.org/doi/abs/10.1063/1.3509179

[73] C. N. Eisler, C. A. Flowers, E. C. Warmann, J. V. Lloyd, P. Espinet-Gonzalez, S. Darbe, M. S. Dee, M. D. Escarra, E. D. Kosten, W. Zhou, and H. A. Atwater, “The polyhedral specular reflector: A spectrum-splitting multijunction design to achieve ultrahigh (>50%) solar module efficiencies,” *IEEE Journal of Photovoltaics*, vol. 9, no. 1, pp. 174–182, Jan 2019.

[74] X. Wang, N. Waite, P. Murcia, K. Emery, M. Steiner, F. Kiamilev, K. Goossen, C. Honsberg, and A. Barnett, “Lateral spectrum splitting concentrator photovoltaics: direct measurement of component and submodule efficiency,” *Progress in Photovoltaics: Research and Applications*, vol. 20, no. 2, pp. 149–165. [Online]. Available: https://onlinelibrary.wiley.com/doi/abs/10.1002/pip.1194

[75] B. Mitchell, G. Peharz, G. Siefer, M. Peters, T. Gandy, J. C. Goldschmidt, J. Benick, S. W. Glunz, A. W. Bett, and F. Dimroth, “Four-junction spectral beam-splitting photovoltaic receiver with high optical efficiency,” *Progress in Photovoltaics: Research and Applications*, vol. 19, no. 1, pp. 61–72. [Online]. Available: https://onlinelibrary.wiley.com/doi/abs/10.1002/pip.988

[76] C. Michel, J. Loicq, T. Thibert, and S. Habraken, “Optical study of diffraction grating/Fresnel lens combinations applied to a spectral-splitting solar concentrator for space applications,” *Applied Optics*, vol. 54, no. 22, pp. 6666–6673, Aug 2015. [Online]. Available: http://ao.osa.org/abstract.cfm?URI=ao-54-22-6666

[77] S. D. Vorndran, B. Chrysler, B. Wheelwright, R. Angel, Z. Holman, and R. Kostuk, “Off-axis holographic lens spectrum-splitting photovoltaic system for direct and diffuse solar energy conversion,” *Applied Optics*, vol. 55, no. 27, pp. 7522–7529, Sep 2016. [Online]. Available: http://ao.osa.org/abstract.cfm?URI=ao-55-27-7522

[78] P. Wang, J. A. Dominguez-Caballero, D. J. Friedman, and R. Menon, “A new class of multi-bandgap high-efficiency photovoltaics enabled by broadband diffractive optics,” *Progress in Photovoltaics: Research and Applications*, vol. 23, no. 9, pp. 1073–1079. [Online]. Available: https://onlinelibrary.wiley.com/doi/abs/10.1002/pip.2516

[79] M. Stefancich, A. Zayan, M. Chiesa, S. Rampino, D. Roncati, L. Kimerling, and J. Michel, “Single element spectral splitting solar concentrator for multiple cells CPV system,” *Optics Express*, vol. 20, no. 8, pp. 9004–9018, Apr 2012. [Online]. Available: http://www.opticsexpress.org/abstract.cfm?URI=oe-20-8-9004

[80] C. Maragliano, M. Chiesa, and M. Stefancich, “Point-focus spectral splitting solar concentrator for multiple cells concentrating photovoltaic system,” *Journal of Optics*, vol. 17, no. 10, p. 105901, aug 2015. [Online]. Available: https://doi.org/10.1088%2F2040-8978%2F17%2F10%2F105901

[81] D. Vázquez-Moliní, A. Álvarez Fernández-Balbuena, E. Bernabeu, J. M. de Luna Clemente, A. Domingo-Marique, and Ángel García-Botella, “New concentrator multifocal Fresnel lens for improved uniformity: design and characterization,” vol. 7407, 2009, pp. 7407 – 7407 – 11. [Online]. Available: https://doi.org/10.1117/12.826346

[82] S. Bäumer, *Handbook of Plastic Optics, second edition.* Wiley, 2011.

[83] U. Schulz, K. Lau, and N. Kaiser, “Antireflection coating with UV-protective properties for polycarbonate,” *Applied Optics*, vol. 47, no. 13, pp. C83–C87, May 2008. [Online]. Available: http://ao.osa.org/abstract.cfm?URI=ao-47-13-C83

[84] U. Schulz, U. B. Schallenberg, and N. Kaiser, “Antireflection coating design for plastic optics,” *Applied Optics*, vol. 41, no. 16, pp. 3107–3110, Jun 2002. [Online]. Available: http://ao.osa.org/abstract.cfm?URI=ao-41-16-3107

[85] B. Wang, J. S. Price, and N. C. Giebink, “Durable broadband ultralow index fluoropolymer antireflection coatings for plastic optics,” *Optica*, vol. 4, no. 2, pp. 239–242, Feb 2017. [Online]. Available: http://www.osapublishing.org/optica/abstract.cfm?URI=optica-4-2-239

[86] S. Kurtz, D. Myers, W. E. McMahon, J. Geisz, and M. Steiner, “A comparison of theoretical efficiencies of multi-junction concentrator solar cells,” *Progress in Photovoltaics: Research and Applications*, vol. 16, no. 6, pp. 537–546, 2008. [Online]. Available: https://onlinelibrary.wiley.com/doi/abs/10.1002/pip.830

[87] P. Hartmann, R. Jedamzik, S. Reichel, and B. Schreder, “Optical glass and glass ceramic historical aspects and recent developments: a Schott view,” *Applied Optics*, vol. 49, no. 16, pp. D157–D176, Jun 2010. [Online]. Available: http://ao.osa.org/abstract.cfm?URI=ao-49-16-D157

[88] J. W. Goodman, *Introduction to Fourier optics, 4th ed.* Macmillan Learning, 2017.

[89] B. Marion, M. Anderberg, P. Gray-Hann, and D. Heimiller, “PVWATTS Version 2 – Enhanced Spatial Resolution for Calculating Grid-Connected PV Performance: Preprint.”

[90] J. A. Jakubiec and C. F. Reinhart, “Towards validated urban photovoltaic potential and solar radiation maps based on LIDAR measurements , GIS data , and hourly DAYSIM simulations,” 2012.

[91] W. D. Lubitz, “Effect of manual tilt adjustments on incident irradiance on fixed and tracking solar panels,” *Applied Energy*, vol. 88, no. 5, pp. 1710 – 1719, 2011. [Online]. Available: http://www.sciencedirect.com/science/article/pii/S030626191000471X

[92] A. Schroder, “Determination of annual optimal altitude and azimuth angles of fixed tilt solar collectors in the continental United States using the national solar radiation database,” 2011.

[93] M. Rönnelid and B. Karlsson, “Irradiation distribution diagrams and their use for estimating collectable energy,” *Solar Energy*, vol. 61, no. 3, pp. 191 – 201, 1997. [Online]. Available: http://www.sciencedirect.com/science/article/pii/S0038092X9700039X

[94] P. Loutzenhiser, H. Manz, C. Felsmann, P. Strachan, T. Frank, and G. Maxwell, “Empirical validation of models to compute solar irradiance on inclined surfaces for building energy simulation,” *Solar Energy*, vol. 81, no. 2, pp. 254 – 267, 2007. [Online]. Available: http://www.sciencedirect.com/science/article/pii/S0038092X06000879

[95] F. Siala and F. Hooper, “A model for the directional distribution of the diffuse sky radiance with an application to a CPC collector,” *Solar Energy*, vol. 44, no. 5, pp. 291 – 296, 1990. [Online]. Available: http://www.sciencedirect.com/science/article/pii/0038092X9090056I

[96] D. H. Li, T. Chau, and K. K. Wan, “A review of the CIE general sky classification approaches,” *Renewable and Sustainable Energy Reviews*, vol. 31, pp. 563 – 574, 2014. [Online]. Available: http://www.sciencedirect.com/science/article/pii/S1364032113008320

[97] L. R. Diaz, P. Blanche, and R. A. Norwood, “Implementation of solar diffuse CIE model in ray tracing program for irradiance calculations,” in *2017 IEEE 44th Photovoltaic Specialist Conference (PVSC)*, June 2017, pp. 1147–1150.

[98] K. Tohsing, W. Klomkliang, I. Masiri, and S. Janjai, "An investigation of sky radiance from the measurement at a tropical site," *AIP Conference Proceedings*, vol. 1810, no. 1, p. 080006, 2017. [Online]. Available: https://aip.scitation.org/doi/abs/10.1063/1.4975537

[99] R. Kittler and P. Valko, "Radiance distribution on densely overcast skies: comparison with CIE luminance standard," *Solar Energy*, vol. 51, no. 5, pp. 349 – 355, 1993. [Online]. Available: http://www.sciencedirect.com/science/article/pii/0038092X9390147G

[100] K. Bücher, "Site dependence of the energy collection of PV modules," *Solar Energy Materials and Solar Cells*, vol. 47, no. 1, pp. 85 – 94, 1997. [Online]. Available: http://www.sciencedirect.com/science/article/pii/S0927024897000287

[101] T. Huld, E. Dunlop, H. G. Beyer, and R. Gottschalg, "Data sets for energy rating of photovoltaic modules," *Solar Energy*, vol. 93, pp. 267 – 279, 2013. [Online]. Available: http://www.sciencedirect.com/science/article/pii/S0038092X13001540

[102] N. Igawa, Y. Koga, T. Matsuzawa, and H. Nakamura, "Models of sky radiance distribution and sky luminance distribution," *Solar Energy*, vol. 77, no. 2, pp. 137 – 157, 2004. [Online]. Available: http://www.sciencedirect.com/science/article/pii/S0038092X04001070

[103] R. Perez, R. Seals, and J. Michalsky, "All-weather model for sky luminance distribution—preliminary configuration and validation," *Solar Energy*, vol. 50, no. 3, pp. 235 – 245, 1993. [Online]. Available: http://www.sciencedirect.com/science/article/pii/0038092X9390017I

[104] A. P. Brunger and F. C. Hooper, "Anisotropic sky radiance model based on narrow field of view measurements of shortwave radiance," *Solar Energy*, vol. 51, no. 1, pp. 53 – 64, 1993. [Online]. Available: http://www.sciencedirect.com/science/article/pii/0038092X9390042M

[105] A. Harrison, "Directional sky luminance versus cloud cover and solar position," *Solar Energy*, vol. 46, no. 1, pp. 13 – 19, 1991. [Online]. Available: http://www.sciencedirect.com/science/article/pii/0038092X91901023

[106] R. Kittler, "Luminance distribution characteristics of homogeneous skies: a measurement and prediction strategy," *Lighting Research & Technology*, vol. 17, no. 4, pp. 183–188, 1985. [Online]. Available: https://doi.org/10.1177/14771535850170040301

[107] A. Gracia, J. Torres, M. D. Blas, A. García, and R. Perez, "Comparison of four luminance and radiance angular distribution models for radiance estimation," *Solar Energy*, vol. 85, no. 9, pp. 2202 – 2216, 2011. [Online]. Available: http://www.sciencedirect.com/science/article/pii/S0038092X11002088

[108] P. Ineichen, “Angular distribution of the diffuse illuminance,” [Online], University of Geneva, 2005, https://archive-ouverte.unige.ch/unige:38778.

[109] S. Wilcox and W. Marion, “1991- 2005 Update: Typical Meteorological Year 3,” [Online], National Solar Radiation Data Base, 2008, https://rredc.nrel.gov/solar/old_data/nsrdb/1991-2005/tmy3/.

[110] Sandia National Lab, “PVLIB Toolbox,” [Online], National Technology and Engineering Solutions of Sandia, 2018, https://pvpmc.sandia.gov/.

[111] A. Lin, C.-Y. Huang, P. Parashar, H.-M. Chou, Y.-S. Lin, M.-H. Kao, S.-W. Chen, C.-H. Shen, J.-M. Shieh, T.-Y. Chen, C.-C. Lin, P. Yu, and H.-C. Kuo, “HIT solar cell performance enhancement with luminescent down shifting phenomenon,” in *Conference on Lasers and Electro-Optics.* Optical Society of America, 2018, p. AW3O.2. [Online]. Available: http://www.osapublishing.org/abstract.cfm?URI=CLEO_AT-2018-AW3O.2

[112] J.-C. Chen, W.-J. Ho, Z.-X. Lin, W.-B. Bai, G.-Y. Chen, H.-X. Zhang, J.-J. Liu, and H.-P. Shiao, “Efficiency increasing of single-junction gaas solar cells coated with species of NIR up-conversion phosphors layer on front-side surface by spin-on film deposition,” in *Conference on Lasers and Electro-Optics.* Optical Society of America, 2018, p. AW3O.1. [Online]. Available: http://www.osapublishing.org/abstract.cfm?URI=CLEO_AT-2018-AW3O.1